ION TRANSPORT ACROSS INDIVIDUAL SUB-CONTINUUM GRAPHENE NANOPORES: PHENOMENOLOGY, THEORY, AND IMPLICATIONS FOR INDUSTRIAL SEPARATIONS

By

Tarun Kumar Jain

B.A. Physics, Mathematics, New York University

Submitted to the Department of Mechanical Engineering
in partial fulfillment of the requirements for the degree of

Doctor of Philosophy in Mechanical Engineering
at the
MASSACHUSETTS INSTITUTE OF TECHNOLOGY

February 2015

Author: Signature redacted

Certified by: Signature redacted

Rohit Karnik
Associate Professor of Mechanical Engineering

Accepted by: Signature redacted

David E. Hardt
Chairman, Department Committee on Graduate Students

This page is left intentionally blank

Ion transport across individual sub-continuum graphene nanopores: phenomenology, theory, and implications for industrial separations

by

Tarun Kumar Jain

Submitted to the Department of Mechanical Engineering
on January 2015 in partial fulfillment of the requirements of the
Doctor of Philosophy in Mechanical Engineering

Abstract

Atomically thin materials, and in particular graphene, provide a new class of solid-state nanopores – apertures that allow for the exchange of matter across thin membranes – with the smallest possible volumes of any ion channel. As the diameter of these nanopores becomes comparable to that of hydrated ions, sub-continuum effects have the potential to enable selective transport similar to that observed in biological ion channels. Being substantially thinner than its biological counterparts, the atomic thickness of graphene places it in a new physical regime with ultimate permeance and distinct geometric constraints on atomic interactions. Engineering graphene nanopores with both high permeance and selectivity has major implications for industrial separation processes, including reverse osmosis, nanofiltration, electrodialysis, metal cation separations, and proton exchange membranes. However, phenomenological measurements on the behavior of single sub-2 nm pores have been extremely limited and the mechanisms of ion transport remain unclear.

In this thesis, the behaviors of sub-2 nm graphene nanopores are experimentally characterized, and a theoretical model is developed that quantitatively matches many of the observed transport features. Inspired by the patch-clamp method for measuring ion channels, a method is developed for statistically isolating individual graphene nanopores by reducing the graphene area under test. The conductances of sub-2 nm graphene nanopores were found to span two orders of magnitude below that of larger graphene nanopores reported so far. Different graphene pores were found to display distinct trends in cation selectivity, as well as nonlinear ionic transport such as voltage-activated and rectified current-voltage curves. Furthermore, in rare instances, nanopores exhibited real-time voltage gating where the nanopore switches between two states in a voltage-dependent manner. The set of these behaviors are in fact highly reminiscent of biological ion channels and deviate from those of larger solid-state nanopores. A theoretical model consisting of electromigration over an energy landscape defined by ion dehydration and electrostatic interactions was able to accurately model the nonlinear conductance characteristics of graphene nanopores, and provided evidence that voltage gating is consistent with proton or ion binding/unbinding in the vicinity of the nanopore. Switching gears, a new measurement platform was developed that can measure large numbers of graphene nanopores, with the aim of performing high-throughput characterization of an entire distribution of nanopores in a graphene membrane. By developing a method to integrate solid-state nanopores into microfluidic devices, and leveraging active microfluidic components for electrical multiplexing, measurements over multiple solid-state and graphene nanopores in a single device were demonstrated. In conclusion, this study presents experimental insight into the behaviors of a new class of two-dimensional solid-state nanopores and elucidates the mechanisms of ion transport in these structures. The mechanistic understanding of transport is expected to guide the engineering of graphene nanopores with both high permeance and selectivity, and the high-throughput platform for testing graphene nanopores will enable rapid screening of graphene nanopore fabrication methods.

This page is left intentionally blank

Acknowledgements

I would like to acknowledge those who contributed to this research, and to this thesis specifically.

First and foremost, I would like to thank Professor Rohit Karnik. Working with Rohit has shaped my approach and understanding of scientific and engineering problems. In many ways, Rohit has had a vital role in defining a new area of research into transport across two-dimensional materials – with the underlying belief that combining persistence, innovation, and precise analysis would help him solve challenging problems. Rohit consistently encouraged me to look deeper and more critically at my work, and patiently provided feedback on the many ideas – some of them only half-baked! – I brought to him. In virtually all instances, the "not-so incidental" benefits of some fundamental insight were generalizable device architectures for exploiting physical principles. I came into graduate school wanting to learn how to make – both in substance and in form – impacts on human civilization with science, and Rohit's guidance has helped me learn how this can be done.

I am also grateful to the other members of my thesis committee, Professor Patrick Doyle, and Professor Cullen Buie. The theory in this thesis was worked out long after the experiments had been finished, and in the interim where a solid explanation seemed elusive, their input, thoughts, and comments were very valuable.

I would like to sincerely thank Ben Rasera and Ricardo Guerrero, two undergraduate students who each spent eight-month periods fully devoted to working on this research with me. It was a pleasure to mentor these two bright students, and it is because of their efforts that so much was accomplished in so short a time.

A thank you also extends to all present and former members of Rohit's research group. There was no lack of spirit or camaraderie. It has been a delight to work here, and although many of us worked on our own distinct research projects, by the end there was a common ambition for doing great science and making great membranes.

Finally, a couple of personal notes. I'd like to thank all of the amazing friends I've met at MIT. I've been inspired by the intensity with which MIT students pursue life endeavors, and the intellectual curiosity they bring to the world. And most importantly, a heartfelt thank you to my family. I've learned from them the many invaluable – though seemingly intangible – aspects of what it means to live.

This page is left intentionally blank

Contents

List of Figures

List of Tables

Chapter 1

Introduction to nanopore membrane separations

The discovery of two-dimensional materials, such as graphene and boron nitride, has enabled a class of sub-continuum nanopores that operate in a new physical regime.[1] The collective physical understanding of mass transport through nanoscale confinement till date strongly suggests that precisely engineered nanopores in two-dimensional materials can exhibit not only ultimate permeance[1] , but also the ability to discriminate between chemical species[2]. In fact, a physical proof for highly permeable, highly selective mass transport conduits already exists in the form of biological ion channels. Unfortunately, these biological ion channels - ubiquitous amongst living organisms, the subject of intense study, and a guiding light in the engineering of synthetic alternatives - are not stable under the extreme chemical, mechanical, and thermal driving forces used to produce large quantities of materials in industrial separations processes. Therefore, in addition to the fascinating physics of mass transport, nanopores in two-dimensional materials have the potential to transform industrial separations through a potent combination of permenace, selectivity, and resilience. By identifying industrial separations as the application domain for sub-continuum nanopores in two-dimensional materials, an analogy can be made between the role of biological ion channels in the *metabolic activity of living organisms* and nanoporous two-dimensional materials in the *metabolism of civilization.*

This introduction will deal exclusively with the higher level discussion of membrane based separation processes, in the context of the practical, the philosophical, and the physical. Following the high-level physical discussion, the paradigm of next generation membranes based on precisely engineered nanopores in a two-

[1] Sub-continuum nanopores refers to nanopores that, owing to a reduction in diameter, exhibit emergent transport properties that are inaccessible with a purely continuum description of transport. As a rule of thumb, nanopores in two-dimensional materials with diameters below $2\,nm$, fall within this category.

dimensional material will be presented. Central to the creation of functional two-dimensional membranes is the an undertanding of how selectivity for specific atomic, ionic, or molecular species is encoded into the structure of a nanopore. Developing an experimentally verified theory for the relationship between a nanopore's structure and its function is a major impetus of this thesis.

1.1 The economic applications of membrane separations

Broadly speaking there are four categories of materials that form the raw material basis for human activies. These are water, geophysically synthesized high energy-density organic deposits (methane, coal, oil), ore deposits (metals, aluminosilicates, salts, gemstones, etc), and the fourth being living organic matter (cultivation of crops for food). Industrial separations, including the refining of hydrocarbons, the refining of metals, and water filtration ("refining" of water) transform these raw materials found in nature into material states conducive for further human processing. If one were to consider the set of life-sustaining processes for human civilization - herein coined the *metabolism of civilization* - industrial separations processes would be a core constitutent.

Selective membranes that preferentially permit transport of specific atomic, ionic, or molecular species play a key role in many industrial separations processes. Membrane based separation processes, which are driven by direct input of mechanical work, are almost always more energy efficient than other thermally driven separations[3]. Despite the compelling reasons to pursue energy efficiency in separations, industrial adoption of membrane based technologies is, and has been, contingent upon the development of high-performance membranes that are correspondingly economically viable. Economic viability is measured not only by energy efficiency (density of entropy generation), but also by capital efficiency, return on investment, and in some cases, quantifiable externalities (such as carbon emissions or public health benefits), compared to other non-membrane based methods.

The performance of a majority of membrane separations is currently limited by the permeability and selectivity of the membrane material. After over fifty years of optimization, existing polymer-based membranes (used in both gas and fluid phase separations), in which ions and molecules undergo highly frustrated transport through a tortuous and serial network of channels, are reaching their phenomenological limits[4]. Recently, based on the ability of biological ions channels to exhibit highly discriminatory transport rates between cations while retaining exceptional permeability, a new paradigm for membranes was proposed. In this paradigm, a parallel array of nanopores in an atomically thin material such as graphene enables selective transport with high permeance[5]. Moving to high-performance membranes that have increased selectivity and permeance is expected to reduce the required membrane area that needs to be installed (for the same

desired output volume)[6] – this overall lowers the capital cost of a facility, improves profit margins for operators, and allows for facilities to be set up in places and in quantities where it would otherwise not be possible.

1.2 Industrial separations and its relation to the *metabolism of civilization*

The ability to control ionic and molecular transport across interfaces is one of the foundational pillars of the functioning of cells and the machinery of life, without which human life, let alone human civilization, could not survive. Through evolutionary pressures, biological ion channels precisely regulate the chemical environments inside cells and enable the extraordinary spectrum of proteins to maintain their molecular functions. Selective transport in ion channels also forms the basis of all neurological activity, using chemical concentrations as a physical basis for electrical signal processing and transduction. Erwin Schrodinger, a member of the 20th century pantheon of physicists, adequately summarized this view[7]:

> How does the living organism avoid decay? The obvious answer is: By eating, drinking, breathing (and in the case of plants) assimilating. The technical term is metabolism. The Greek word change or exchange. Exchange of what? Originally the underlying idea is, no doubt, exchange of material...What an organism feeds upon is negative entropy [order]. Or, to put it less paradoxically, the essential thing in metabolism is that the organism succeeds in freeing itself from all the entropy it cannot help producing while alive. – Erwin Schrodinger

In summary, 'metabolic' processes consume energy to locally create order, which facilitates the synthesis or purification of required materials. This essential definition of metabolic processes not only permeates molecular and cellular function, but also applies equally to the human activities of labor and work[8]. It is clear that on the existential level, a functioning civilization must extract from its surroundings all of the materials consumed in the multitude of human activities and endeavors. All work products fundamentally require processing and refining materials from the external environment and transforming them into new functional elements. Even more stringent requirements on materials refinement are exacted by the technological artifice, which relies on harnessing electrical, optical, and mechanical properties of intentionally purified or alloyed materials.

Civilization involves processing and transformation of materials found in their natural state into functional purified, alloyed, or synthesized derivatives. Most commodities, including water, coal, and metals, are found in a relatively purified state by an accident of nature, in which differential transport rates, phase separation,

or locally frustrated transport have led to a concentrated deposit of a material. When materials are purified or mixed in precise ratios, the material properties that emerge can be substantially different and differentiated, thereby enabling a large range of functionalities and motivating their initial purification. In a highly simplistic description, these distinct material properties physically originate as emergent features of chemical bonding and physical interactions between molecules. Thus, the use of virtually all materials begins with refining, wherein each chemical species in a material deposit is segregated or demixed. Compared to the initial mixed state, the de-segregated chemical species have lower entropy. In this simple observation, we find a relationship between a *metabolic imperative* for civilization, namely materials demixing, and fundamental physical properties of a system.

The availability of resources is a critical question. As an example, in evolutionary biology, the availability of resources in bacterial colonies has been studied, and determines the extent to which specific genetic traits survive. Continuing the parallel between molecular biology and civilization, analogous to genetic traits are the foundational character traits of the collective organized society - and if ever there were a good reason to survive, it would be to cultivate whatever it truly means to live as humans in a human civilization.

1.3 Literature on transport through graphene nanopores

After nearly sixty years of optimization, the polymer based selective membranes used today in both gas phase and aqueous phase separations have reached their phenomenological limits. This phenomenological limit is characterized by a well defined trade-off between the selectivity and permeance of the membrane[4], and is determined by the membrane architecture alone, independent of the specific formulation of the polymer material. As a result, alternative membrane architectures have been explored to improve the permeance and selectivity of separations membranes; many of these new membrane materials consist of well defined nanopore structures which aim to use short-range interactions to exhibit transport properties that emerge as a direct consequence of the nanopore structure[5]. As a general principle, the selectivity and permeance of a structure is a fundamental property of the nanopore structure. As one increases the thickness of a membrane material - in most membranes, this is equivalent to putting multiple nanopores in parallel - the selectivity increases while the permeance decreases. In direct opposition to the existing polymer based membranes, this heuristic analysis indicates that optimal performance will be achieved with a parallel array of nanopores in an ultrathin membrane, with each nanopore in the membrane designed at the atomic level to yield extremely high selectivity.

A notable manifestation of this paradigm shift are aquaporin based membranes. Aquaporin ion channels are highly selective transport polar water molecules over all charged species (including the proton). Prelimi-

nary calculations indicated that aquaporin based membrances could yield membranes with as high as a 100 fold increase in permeance with the same selectivity as the aquaporin channel itself[9]. However, the lipid bilayer support for ion channels has proven to be a major limitation in realizing the performance promised by ion channel based membranes. It is clear than any manifestation of the new membrane architecture with a parallel array of atomically precise nanopores must rely on solid-state materials that exhibit mechanical and chemical stability under the harsh operating conditions in industrial separations processes. Fabrication of sub-nm nanopores in solid-state materials, let alone arrays of trillions of atomically precise sub-nm nanopores, has till date been limited. One notable exception to this is graphene, the archetypal two-dimensional material.

As early as 2009, experimental research into monolayer graphene as a membrane material for desalination had started. Graphene has ideal material properties for industrial separations membranes: it has a high mechanical strength[10, 11], is chemically stable in oxidizing and acidic conditions, and can be made in large quantities using chemical vapor deposition (CVD)[12]. Graphene in its pristine state without holes has been shown to be impermeable to atomic and ionic species down to helium[13], though a protons have recently been shown to permeate across pristine graphene - though the absolute permeance is very low, it is high enough to use graphene in fuel cells[14]. Mass transport across graphene is thus enabled by creating nanopores in the membrane. Molecular dynamics simulations of graphene nanopores predict extremely high water permeance (under an applied pressure)[15] and ionic conductance (under an applied voltage)[16]. In aqueous phase, ions are coordinated tightly by water molecules, forming structures known as hydration shells[17], that effectively make the ion significantly larger than water molecules. As a result, molecular dynamics simulations have predicted that graphene nanopores can have both high permeance (for water) and high selectivity (against ions) when the nanopores are smaller than the hydrated radius of the ions[2]. Functional groups on the graphene nanopore have also been implicated in imparting charge based selectivity between anions and cations[18]. Charge based selectivity has led to preliminary investigation of the use of graphene as an electrodialysis separation membrane[19] with similar order of magnitude improvements in performance as predicted with reverse osmosis separation with graphene.

Most importantly, however, graphene's atomic thickness implies that vacancy defects - which are universal on a thermodynamic basis - are also nanopores. Vacancy defects are typically significantly smaller than the nanopores made in thicker solid-state nanopores, enabling the *experimental* synthesis of the sub-nm pore sizes that are theoretically predicted to exhibit selectivity. Several methods for fabricating sub-nm nanopores in graphene have been investigated previously, including oxygen plasma[20], electron beam irridation[21], ion beam bombardment[22], and dopants in chemical synthesis[23]. Measurements over large areas of graphene have indicated that nanopores can be artificially created that exhibit selective transport between water and ions[22]. However, large area membranes fundamentally average over the behavior of individual nanopores,

and therefore do not give a sufficiently detailed understanding of the behaviors and physics of sub-nm solid-state nanopores. Therefore, in thesis, the emphasis will be on the study of individual nanopores. The approach will combine experiments and theory to provide a more complete picture of ion transport on the sub-nanometer lengthscale.

1.4 Thesis Overview

This thesis is devoted pre-dominantly to the scientific understanding of ion transport through two-dimensional nanopores with the express aim of providing the foundations for engineering these nanopores with selectivity. To frame the problem, a mathematical formalism for ionic transport across a single nanopore is described (Chapter 2). Complementing the theory, an experimental technique is developed to statistical isolate, and measure, the behaviors of individual sub-continuum nanopores in a graphene membrane (Chapter 3). We find that sub-continuum graphene nanopores exhibit fascinating properties remnisicent of biological ion channels, namely nonlinear current-voltage properties, distinct trends in cation selectivity, and stochastic switching. By examining atomic interactions in the graphene nanopore, and making some approximations on the potential profile in the pore, a simple model is constructed - as a prototype inverse problem - to estimate the structural properties of a nanopore given experimental characterization (Chapter 4). Surprisingly, the model is able to account for all of the nonlinear behaviors observed in graphene nanopores. To address the need for higher data throughput to fully verify physical theories of ion transport, a device architecture is designed that can characterize an entire distribution of nanopores with single pore resolution (Chapter 5). Understanding ion specific contributors to transport phenomena is a fundamental precursor to engineering selectivity between ions. When science is viewed through the lens of societal applications, an essential aspiration is that an in-depth knowledge of a system, and the tools to study the system, will both accelerate application development and our human capabilities. Therefore, this thesis is focused on providing both a rigorous experimental-theory combination to ion transport and on developing the conceptual and practical tools for future analysis of ion transport at the single pore level.

The narrative for next-dimensional membranes extends well beyond creating selective nanopores in two dimensional materials. Developing heirarchical structures that collectively maximize transport efficiency[24], and fabrication of nanopores over km^2 areas with Ångstrom precision, are also critical to realization of high-performance, economically viable membranes. Though both of these tasks are monumental engineering endeavors, neither of will be covered in this thesis.

Chapter 2

Theory of ion transport through nanopores

> The general theory of quantum mechanics is now almost complete...The underlying physical laws necessary for the mathematical theory of a large part of physics and the whole of chemistry are thus completely known, and the difficulty is only that the exact application of these laws leads to equations much too complicated to be soluble. It therefore becomes desirable that approximate practical methods of applying quantum mechanics should be developed, which can lead to an explanation of the main features of complex atomic systems without too much computation. - Paul Dirac, 1927[25]

Dirac's observation is extraordinarily relevant to the field of ion transport through protein ion channels; their complex three dimensional structure makes first principles calculation of functional behaviors analytically impossible, and computationally challenging. The literature is littered with a myriad of analytic approximations and computational approaches to ion transport; the three dimensional-complexity of biological ion channels makes attempts to use mathematical treatments to interpret physics in ion channels rare.

Graphene is an order of magnitude thinner than any other nanopore or ion channel, and is uniquely (along with other two dimensional materials) in a regime where both the thickness of the nanopore and the diameter can be less than one nanometer. Though the reduction in thickness confers clear advantages for membrane permeance, it also makes graphene the most ideal nanopore possible to study tranpsort physics at the nanoscale. Even for this nearly ideal nanopore system, both quantum and classical dynamics with atomic resolution are too computationally expensive. In contrast, statistical methods provide a convenient way of reducing the number of degrees of freedom, and should facilitate a synthesis of different interactions

into a centralized framework for the structure-function relationship.

This chapter, which builds the basic theory for ion transport through nanopores, will provide the following:

1. A summary statistical mechanics for highly interacting systems
2. A brief review of statistical mechanics for highly interacting particulate systems
3. A sketch of the derivation of partial differential equations from stochastic differential equations for highly interacting particulate systems
4. Context for using the partial differential equations to compute transport properties (and implicitly, the structure function relationship)

Graphene nanopores, with the smallest possible volume of any protein, synthetic, or solid-state nanopores offer unique opportunities to understand the relationship between structure and function. While the structure of the nanopore constrains all forces acting in the system, some functional behaviors are more highly correlated with structural properties than others. The thereotical framework presented in this chapter, though abstract, will provide a basis for deconvoluting the contributions to the total transport rates of many different interactions in the system.

2.1 Approaches to nanopore physics in literature

> Arguably, the signature of modern science lies in its ability to both conceptualize the very large and very small, and to develop suitable diagnostic techniques. The merely large and merely small are not so incidental beneficiaries....Relevant theory [nanoscale transport under environmental confinement] has been available for ages, but advances in the technology have supplied new motivation. - Percus 2014[26]

Theories for the equilibrium, and to some extent the non-equilibrium, description of nanopores and ion channels have existed in physics since 1946 under the guise of the statistical mechanics of open systems with strong interparticle and boundary interactions under external potentials and thermal fluctuations[27, 28]. Since then, the statistical mechanics framework for highly interacting fluids has been intrepreted in the context of equilibrium correlations in homogeneous fluids[29] (the very large), and analytically exact solutions for one-dimensional systems of hard rods[30] (very small). However, there were no experimentally relevant physical systems to which the theory could be meaningfully applied until the elucidation of the structure of biological ion channels in the mid 1990's[31, 32, 33]. Within the decade after this discovery, by the mid-2000's, the study of synthetic nanochannels and nanofluidic systems was in full swing. These nanofluidic

systems, which constituted the "merely small", were described with great success[34] by the "non-incidental benefits" of the mean field theory approximation to the fully general non-equilibrium statistical mechanics - the Poisson-Nernst-Planck equations.

The Nernst-Planck equation, describing diffusive transport across a potential or convective landscape, had been applied to ion channels - at that time, a large collective of ion channels in a nerve fiber - as early as 1949 by Hodgkin and Katz[35]. The mathematical descriptions of transport assumed that all potential gradients were constant, assigning fitting coefficients (the permeance of a channel) to all complex potentials that give rise to selective transport. By the 1960's, there was some recognition that selective transport arose from short-range interactions between ions, their hydration shells, and confined geometries[36], thereby making use of the growing body of literature on the thermodynamic properties of ionic hydration first derived in 1920 by Max Born. It was not until Neher and Sakmann isolated individual ion channels in 1976 [37] that it was understood that selective transport was an intrinsic property of individual channels, not an emergent phenomena from a collective. This understanding was in direct contrast to ionic selectivity that was observed in porous networks such as polymer based membranes used in desalination and ion selective glass electrodes, and was brought to its inevitable conclusion with the visualization of the atomic structure of biological ion channels.

Knowledge of the structure of ion channels provided clear motivation to transition from gross mean field approximations to a finer understanding of transport with atomic resolution. The first attempts consisted of all atom molecular dynamics simulations of ion channels[38, 39], with the aim of elucidating the mechanisms by which ionic selectivity arises. Molecular dynamics simulations excel at modeling specific nanopore configurations, but are unable to shed generalizable insight into properties of highly-interacting particulate systems under extreme confinement. For this task, a return to the fundamental statistical mechanical descriptions would be needed. About the same time, Eisenberg started writing a series of analytical papers on the physics of ion transport, starting with a re-derivation of the multi-dimensional Fokker-Planck equations[40].

The Fokker-Planck description of non-equilibrium transport is a stochastic analog of the Liouville equations considered in the 1940's papers by Born, Green, and Kirkwood that treats as stochastic the many deterministic interactions in a system. Casting the problem in the mathematical terminology of stochastic differential equations is extremely useful, as the formalsim can easily capture non-equilibrium properties of the system. However, typical treatments with the Fokker-Planck equation typically exclude an important property of ion channels - being an open system, the number of particles is subject to change. When the number of particles in the system is large, these number fluctuations can be ignored. In ion channels, the number of ions - and even sometimes water molecules - is not so large that number fluctuations can be neglected. Number fluctuations in graphene nanopores, which represent the physical limit of a very small

system for study, should be even more pronounced. Unlike larger systems, in the limit of the very small - namely two dimensional nanopores - the number of ions is so small that explicit enumeration of the nanopore occupancy and computation of nonequilibrium properties of a nanopore should be possible.

The potential to explicitly compute consequences of interparticle interactions in highly confined nanopores makes certain mathematical formalisms more intuitive and physically relevant than others. This thesis synthesizes relevant theory in stochastic differential equations and nonequilibrium statistical mechanics with a notation that makes the open nature of a graphene nanopore explicit. Intrisic geometric properties in steady state will be discussed to create a potentially viable framework for studying the nonequilibrium properties of highly interacting systems.

2.2 Statistical mechanics in an interacting open system

2.2.1 Natural control volumes of a nanopore system

The simplest nanopore system consists of a single nanopore in a planar membrane with one reservoir on either side of the membrane. At the boundaries of these reservoirs, external driving forces such as a pressure gradient or electric potential gradient are applied. These driving forces result in transport of matter from one reservoir to the other. As the membrane is considered to be completely impermeable, all mass transport must take place through the nanopore. As shown in Figure 2.2.1, this nanopore system can be conveniently described by three control volumes: (1) a first reservoir, (2) a second reservoir, and (3) a nanopore connecting the two.

Strictly speaking, the mass transport equations need to be solved both in the reservoirs and in the nanopore, as the external fields (electric or pressure) and concentrations of the chemical species at the entrance and exit of the nanopore will be modulated by any dissipation in the reservoirs. The reservoirs, however, are significantly larger than the nanopore, thereby requiring that the mass transport equations be solved in a domain much larger than the nanopore itself. In most of the systems studied historically, the mass transport resistance of the nanopore has been significantly larger than the mass transport resistance of particles from the boundary of the reservoir to the nanopore; therefore, in most cases, mass transport equations are solved only in the nanopore, and it is assumed that the concentration of particles and the applied driving forces are the same at the boundary of the nanopore as they are at the boundary of the reservoir.

However, it has been shown that mass transport in the reservoir can have a significant impact on transport through the nanopore[41]. With non-trivial coupling between the reservoirs and the nanopore in mind,

a particularly elegant method of solving for mass transport through the entire system was described by Eisenberg et al.[42]. In this method, the mass transport equations in each one dimensional control volume (Figure 2.2.1) is solved independently. Each independent solution of the mass transport equations is used to update the boundary conditions used to solve for mass transport in the adjacent control volume. Eventually, a self-consistent solution is obtained, where the boundary conditions on each domain are equal. The ability to model the system with the solutions to differential equations in distinct control volumes is remarkably powerful. In this thesis, we will model the transport properties of idealized cylindrical nanopores, with a radius, r_p in a membrane with a thickness of L_p. A system with a cylindrical nanopore can be fully divided into four control volumes (Figure 2.2.1), in which the volumes and boundary conditions are naturally expressed in cylindrical coordinates.

Most of the self-consistent theory has been performed in a one dimensional coordinate system: using cylindrical coordinates in the nanopore and averaging over the radial coordinate, and spherical coordinates in the reservoir and averaging over the angular dependence[42]. As shown in Figure 2.2.1, the 1D control volumes neglect the small volume of the spherical caps at the nanopore entrance and exit. In the limit of very long nanopores (where $L_p \gg r_p$), these volumes can be neglected [43]. For graphene nanopores, and other two-dimensional materials, the aspect ratio limit is reversed, and in many cases, $L_p < r_p$. Even though the spherical caps lack the confining boundaries of the nanopore control volume, their volume is similar to the volume of the nanopore.

Therefore, future attempts to use self-consistent theory for two-dimensional nanopores, should use the two dimensional set of natural control volumes instead, and this thesis will adopt the two-dimensional description as well.

In a self-consistent solution, the mass transport equations are derived and solved for each control volume separately. As an initial investigation into mass transport through two-dimensional nanopores, the majority of this chapter will focus on transport in the nanopore only; the challenge of self-consistent solving of the multiple control volumes is a challenge in numerical methods, and not *directly* the relevant physical one.

2.2.2 Enumeration of states in open systems

In this section, a reduced master equation for the time evolution of the nanopore occupancy will be presented. A consequence of the smallness of the nanopore control volumes is that the number of particles in each control volume can be enumerated explicitly. Particles are allowed to move between control volumes, making each control volume an open sub-system. The number of particles in the reservoirs, however, is significantly

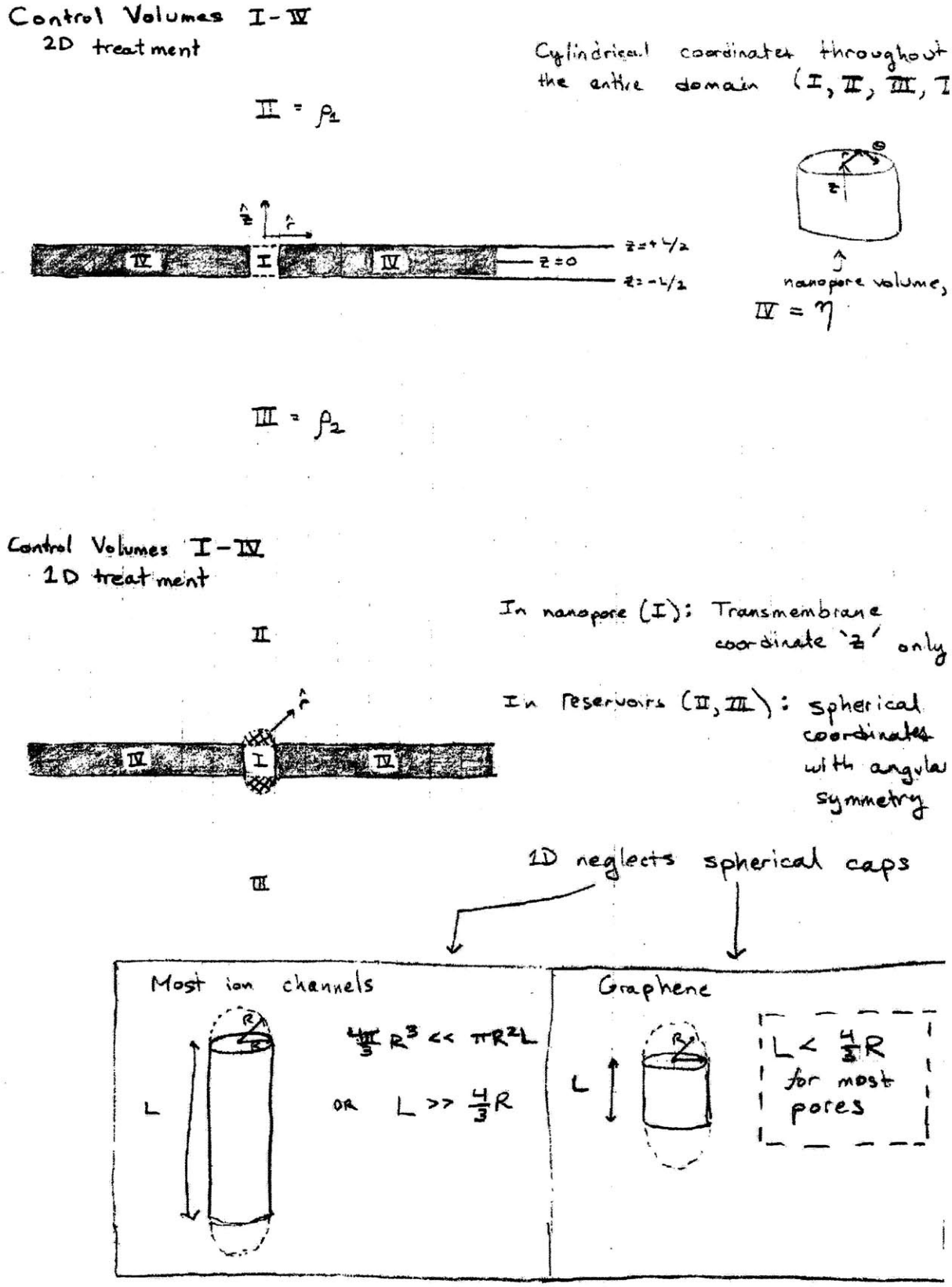

Figure 2.2.1: One and two dimensional coordinate systems for natural control volumes. Current through the control volumes (I, II, III) is conserved. No mass exchange can occur with control volume IV (the graphene membrane).

larger - by many orders of magnitude - than the number of particles in the nanopore. Let us consider an open nanopore sub-system with s particles in a system with a total of N particles. The N dependence serves primarily to highlight that the reservoir state impacts the nanopore occupancy and probabilies. The notation that follows is written to closely follow the notation used in the textbook, *Statistical Mechanics of Phases, Interfaces, and Thin Films*[44] (Davis). Each particle has a coordinate in phase space of $\vec{\chi} = (\vec{x}, \vec{v})$, where $\vec{x}$ is the particle's position, and $\vec{v}$ is the particles velocity.

Consider the probability of finding the particles in a configuration, $p_{N(t)}\left(\vec{\chi}_1, \vec{\chi}_2, \ldots, \vec{\chi}_N, t\right)$, at some time t. Normalization of particles requires that the total probability integrate to unity:

$$\sum_{N=1}^{\infty} \int d^N \vec{\chi}\, p_{N(t)}\left(\vec{\chi}_1, \vec{\chi}_2, \ldots, \vec{\chi}_N, t\right) = 1 \tag{2.2.1}$$

The "s-body configuration distribution function" (Davis p157) can be written as:

$$p_{s(t),N(t)}\left(\vec{\chi}_1, \vec{\chi}_2, \ldots, \vec{\chi}_s, t\right) = \int \left(d^{N-s}\vec{\chi}\right)\, p_{N(t)}\left(\vec{\chi}_1, \vec{\chi}_2, \ldots, \vec{\chi}_N, t\right) \tag{2.2.2}$$

The total probability that the sub-system is found in a configuration with s particles can finally be written again as a sum (Davis p382):

$$P^{(s)} = \sum_{N=s}^{\infty} P\left(N\right) p_{s(t),N(t)} \tag{2.2.3}$$

Where $P\left(N\right)$ is the total probility of finding the system in a configuration with N particles. In the descriptions above, there is no mention or indication of what these probabilities might actually be; this omission is intentional. Equilibrium statistical mechanics allows the probabilities above to be written explicitly (Davis). In the general nonequilibrium case it is dangerous to *a priori* assume that steady state solutions are close to equilibrium. Generally speaking, there is no consensus yet on how to define an appropriate metric for how far from equilibrium one is.

Next, we write down the master equation for evolution of the probability density in time, given by transitions between states $(s, N) \rightarrow (s', N')$[45].

$$\frac{\partial P^{(s,N)}}{\partial t} = \sum_{s'} \sum_{N'} \left(W\left[s', N' \rightarrow s, N\right) P^{(s',N')} - W\left(s, N \rightarrow s', N'\right) P^{(s,N)} \right] \tag{2.2.4}$$

In the equation above, $W\left(s', N' \rightarrow s, N\right)$ is the probability from transition from a state s', N' into a state s, N. This equation is again fully general provided that the states are discrete and not continuous. However,

one could make the argument that the probability of transitions between states is not independent of the positions and velocities of each particle, or specifically that $W\left(\{\vec{x}\}_{s'}, \{\vec{x}\}_{N'} \rightarrow \{\vec{x}\}_{s}, \{\vec{x}\}_{N}\right) = W\left(s', N' \rightarrow s, N\right)$. Strictly speaking, transitions between the discrete states (s, N) occur only for particles in direct proximity to (less than one particle away from) the boundaries of the control volumes. While it is possible to write down a master equation for continuous phase space and discrete number states together, integration over phase space would provide an equation similar to 2.2.2, just with the transition probabilities being different. This thesis takes an alternative approach: we will investigate computation of the steady state probability density $P^{(s)} = \int d^s\vec{\chi}\, p^{(s,N)}\left(\vec{\chi}_1, \vec{\chi}_2, \ldots, \vec{\chi}_s\right)$ from its own continuous master equation, with the aim that solutions for $p^{(s,N)}$, which assume the occupancy of the nanopore is known, can be then used with the master equation (equation 2.2.2) to compute the average occupancy of the pore.

We also note that one might also be interested in a simpler problem, namely one that only depends on ensemble averages over the reservoirs and the number of particles in the nanopore, and that the N dependence can be omitted entirely. In doing so, it is assumed that the reservoir state was used in the boundary conditions to compute the probabilities $P^{(s)}$. The reduced master equation then has the form:

$$\frac{\partial P^{(s)}}{\partial t} = \sum_{s'}\left[W\left(s' \rightarrow s\right)P^{(s')} - W\left(s \rightarrow s'\right)P^{(s)}\right] \tag{2.2.5}$$

This reduced master equation is a natural consequence of the smallness of the nanopore compared to the reservoir, or specifically that both $s \lll N$ and that the volume of the nanopore is significantly smaller compared to the reservoirs. A derivation for this result, though expressed in terms of the entropy of the system, can be found in Phil Attard's book on nonequilibrium statistical mechanics (p26 onwards) [46].

2.2.3 Statistical mechanics and the BBGKY heirarchy

Using the Liouville equation, physicists have derived several useful formalisms for studying the statisical mechanics of highly interacting particle systems. The following treatment is fully deterministic, and fundamentally includes all atoms and molecules in the system, including water molecules; it therefore represents the most computationally intensive formalism short of molecular dynamics. However, using this deterministic picture will serve to highlight the need for approximations and approximate solutions. This section on statistical mechanics follows the discussion found in Kardar's book, *Statistical Physics of Particles* on p62 onwards[47]:

$$\frac{\partial \rho_M}{\partial t} = \{\rho_M, \mathcal{H}\} \tag{2.2.6}$$

Where $\rho_M = \rho_M(\vec{q}_1, \vec{p}_1, \vec{q}_2, \vec{p}_2, \ldots, \vec{q}_N, \vec{p}_N)$ is the probability density, $\vec{q}_i$ is the position of the i^{th} particle, $\vec{p}_i$ is the momentum of the i^{th} particle, and $\mathcal{H}$ is the Hamiltonian of the system. In expanded form, the Liouville equation is:

$$\frac{\partial \rho_M}{\partial t} = \sum_{k=1}^{M} \frac{\partial \rho}{\partial \vec{p}_k}\frac{\partial \mathcal{H}}{\partial \vec{q}_k} + \frac{\partial \rho}{\partial \vec{q}_k}\frac{\partial \mathcal{H}}{\partial \vec{p}_k} \tag{2.2.7}$$

For convenience, we consider the Hamiltonian for particles that interact via central, pair-wise forces in an external potential:

$$\mathcal{H} = \sum_{i=1}^{M} \frac{\vec{p}_i \cdot \vec{p}_i}{2m_i} + \sum_{i=1}^{M} \mathcal{U}(\vec{q}_i) + \frac{1}{2}\sum_{i=1}^{M}\sum_{j=1\neq i}^{M} \mathcal{V}(\vec{q}_i - \vec{q}_j) \tag{2.2.8}$$

For a nanopore, the single particle potential, $\mathcal{U}(\vec{q}_i)$ can furthermore be decomposed into an external force caused by the nanopore:

$$\mathcal{U}(\vec{q}_i) = \mathcal{U}_{ext}(\vec{q}_i) + \mathcal{U}_{pore}(\vec{q}_i) \tag{2.2.9}$$

Multi-body interactions between the nanopore and the molecular distribution - primarily arising form polarization of the membrane - have been omitted for the time being. From here, the goal is to write down an equation for the time evolution of the probability density for the sub-system with σ particles, given by $\rho_\sigma = \rho_\sigma(\vec{q}_1, \vec{p}_1, \vec{q}_2, \vec{p}_2, \ldots, \vec{q}_\sigma, \vec{p}_\sigma)$. It is extremely important to note here that the system of M particles and the sub-system of σ particles are not the same as described in the previous section. Earlier, the system was divided into a nanopore sub-system, and two reservoirs - one on either side of the nanopore. In this description, M is the total number of particles in the system, and σ is any smaller collection of particles in the system. The expression for ρ_σ furthermore should be derived from the total system dynamics, which according to equation 2.2.3 is deterministic, albeit chaotic for large numbers of particles. The derivation for the sub-system dynamics begins by splitting the Hamiltonian into three components:

$$\mathcal{H} = \mathcal{H}_{M-\sigma} + \mathcal{H}_t + \mathcal{H}' \tag{2.2.10}$$

Where these three Hamiltonians are given by:

$$\mathcal{H}_{M-\sigma} = \sum_{i=\sigma+1}^{M} \frac{\vec{p}_i \cdot \vec{p}_i}{2m_i} + \sum_{i=\sigma+1}^{M} \mathcal{U}(\vec{q}_i) + \frac{1}{2} \sum_{i=\sigma+1}^{M} \sum_{j=\sigma+1 \neq i}^{M} \mathcal{V}(\vec{q}_i - \vec{q}_j) \tag{2.2.11}$$

$$\mathcal{H}_{\sigma} = \sum_{i=1}^{\sigma} \frac{\vec{p}_i \cdot \vec{p}_i}{2m_i} + \sum_{i=1}^{\sigma} \mathcal{U}(\vec{q}_i) + \frac{1}{2} \sum_{i=1}^{\sigma} \sum_{j=1 \neq i}^{\sigma} \mathcal{V}(\vec{q}_i - \vec{q}_j) \tag{2.2.12}$$

$$\mathcal{H}' = \frac{1}{2} \sum_{i=1}^{\sigma} \sum_{j=\sigma+1}^{M} \mathcal{V}(\vec{q}_i - \vec{q}_j) \tag{2.2.13}$$

These expressions for the Hamiltonian can be used in equation 2.2.3 to obtain an equivalent Liouville equation for the evolution of the phase space density for the subsystem of s particles, ρ_s (Kardar 62-64):

$$\frac{\partial \rho_\sigma}{\partial t} - \{\rho_\sigma, \mathcal{H}_\sigma\} = (N - \sigma) \sum_{k=1}^{\sigma} \int d^{\sigma+1}\vec{q}_k d^{\sigma+1}\vec{p}_k \frac{\partial \mathcal{V}(\vec{q}_k - \vec{q}_{\sigma+1})}{\partial \vec{q}_k} \cdot \frac{\partial \rho_{\sigma+1}}{\partial \vec{p}_k} \tag{2.2.14}$$

The term on the right hand side in equation 2.2.3 accounts for interactions between particles in the sub-system and particles outside of the sub-system. More generally, the sub-system dynamics has the form of a Boltzmann equation:

$$\frac{\partial \rho_\sigma}{\partial t} - \{\rho_\sigma, \mathcal{H}_\sigma\} = \left(\frac{\partial \rho_\sigma}{\partial t}\right)_{coll}^{M-\sigma} \tag{2.2.15}$$

Where the term $\left(\frac{\partial \rho_\sigma}{\partial t}\right)_{coll}$ corrects the phase space evolution for interactions with the reservoirs outside the nanopore. The typical approach, that taken in the BBGKY approximation (Kardar 65, Davis 383-385) [47, 44] is to solve out starting with a sub-system of $\sigma = 1$, then $\sigma = 2$, and so on. However, $\sigma = 1$ does not refer to the occupancy of the nanopore, but picking any particle in the sytem. One option is to pick the first particle so that it is in the nanopore as a prior requirement. The remainder of the particles, however, includes both other particles in the nanopore and those outside the nanopore. It is therefore seen that the heirarchical equations does not enable an analysis with a clear interpretation in reference to the enumeration of nanopore occupancy by the index s. This formalism becomes even more inconvenient when trying to average over the water molecule degrees of freedom. Instead of continuing with the statistical mechanics, an alternative approach based on stochastic differential equations will be employed.

2.3 Converting stochastic to partial differential equations in particulate systems

2.3.1 A stochastic description of particulate transport

In contrast to the deterministic statistical mechanics, an approach is needed that facilitates averaging over unwanted degrees of freedom. For the purposes of this discussion, these unwanted degrees of freedom are the full phase space descriptions of water molecules and the full phase space descriptions of particles outside the nanopore. We therefore turn our attention to stochastic approaches, which generalize the effects of multiple degrees of freedom as random perturbations on a sub-system of interest.

The dynamical evolution described by Liouville equation is one instance of a more general class of continuous stochastic processes. The Kramers-Moyal expansion method allows for a large class of first order stochastic differential equations to be converted near exactly into partial differential equations on the probability density (Risken 48)[45]. Much of the theory in this section follows the write-up by Garcia-Palacios[48], but is extended to multiple spatial dimensions for multiple particles. The equations of motion are in fact, a second order stochastic differential equation. Nonetheless, by re-writing the equation of motion as two coupled first order ODE's, the Klein-Kramer's equation can be derived for the dual space (x, v) (Risken 229)[45].

Equivalent to the Liouville equation, the deterministic dynamics of the system can be written in terms of the forces on each particle:

$$m_i \ddot{\vec{x}}_i = \vec{F}_i \left(\vec{x}_1, \vec{x}_2, \ldots \vec{x}_N\right) \tag{2.3.1}$$

Writing equation 2.3.1 as two first order differential equations by introducing the velocity, we then have:

$$m_i \dot{\vec{v}}_i = \vec{F}_i \left(\vec{x}_1, \vec{x}_2, \ldots \vec{x}_N\right) \tag{2.3.2}$$

$$\dot{\vec{x}}_i = \vec{v}_i \tag{2.3.3}$$

The number of particles above ranges from $i \in [1, M]$, where M is the total number of particles, including water molecules. From here on, much of the analysis will be performed following Risken's comprehensive book, *The Fokker-Planck Equation: Methods of Solutions and Applications[45]*. Considering a total of N ions or other molecules in solution now, the equations can be written as (Risken 2):

$$\dot{\vec{v}}_i + = \frac{1}{m_i}\vec{F}_i\left(\vec{x}_1, \vec{x}_2, \ldots \vec{x}_N\right) - \gamma\vec{v}_i - \Gamma_W^i\left(t\right) \tag{2.3.4}$$

$$\dot{\vec{x}}_i = \vec{v}_i \tag{2.3.5}$$

Where γ is a drag coefficient, and $\Gamma\left(t\right)$ is the stochastic (fluctuating) force per unit mass. At this point, the degrees of freedom of the water molecules have been completely integrated over. This integration over water degrees of freedom is extremely robust, and of the many approximations that will be made, is the least worrisome. The forces that remain in the system are forces between particles, between particles and the nanopore, and between particles and an external potential.

$$\vec{F}_i = \vec{\nabla}_{\vec{x}_i}\left(\mathcal{U}_{ext}\left(\vec{x}_i\right) + \mathcal{U}_{pore}\left(\vec{x}_i\right) + \sum_{j=1\neq i}^{N}\mathcal{V}\left(\vec{x}_i - \vec{x}_j\right)\right) \tag{2.3.6}$$

From the force, it can be seen that coupling between the particles in the bath with particles in the nanopore occurs because of the inter-particle interaction term $\mathcal{V}\left(\vec{x}_i - \vec{x}_j\right)$. In the same spirit as the Hamiltonian separation performed in statistical mechanics, the inter-particle potential can be split into three terms:

$$\mathcal{V}^\alpha = \sum_{j=1\neq i}^{N}\mathcal{V}\left(\vec{x}_i - \vec{x}_j\right) = \mathcal{V}_s^\alpha + \mathcal{V}_N^\alpha + \mathcal{V}_{s-N}^\alpha \tag{2.3.7}$$

$$\mathcal{V}_s^\alpha = \sum_{j=1\neq i}^{s}\mathcal{V}\left(\vec{x}_i - \vec{x}_j\right) \tag{2.3.8}$$

$$\mathcal{V}_N^\alpha = \sum_{j=s+1}^{N}\mathcal{V}\left(\vec{x}_i - \vec{x}_j\right) \tag{2.3.9}$$

$$\mathcal{V}_{s-N}^\alpha = \sum_{j=s+1}^{N}\mathcal{V}\left(\vec{x}_i - \vec{x}_j\right) \tag{2.3.10}$$

Of these potentials, the term $\mathcal{V}_s^\alpha$ describes inter-particle interactions within the nanopore - these are specifically the interactions that we would like to keep explicitly in the dynamics. The potential $\mathcal{V}_N^\alpha$ impacts the distribution of ions outside the pore, but does not contribute to the force on ions in the pore, as $\vec{\nabla}_{\vec{x}_i}\left(\mathcal{V}\left(\vec{x}_j - \vec{x}_k\right)\right) = 0$. Recall that the potential is a function of the distance between particles, $\vec{x}_i - \vec{x}_j$, and that the force arising from these potentials will be in the direction of $\hat{x}_i - \hat{x}_j$. The potential $\mathcal{V}_{s-N}^\alpha$ computes interactions between ions in the nanopore and outside the nanopore. Our aim is to create a formalism that

allows each reservoir to be solved separately, which means that this term needs to be approximated, i.e. the degrees of freedom need to be reduced.

Let us consider the assumption that interactions between particles results in a net mean force and a stochastic force that depend only on the position of the particle in the pore:

$$\left\langle \vec{\nabla} \left[\sum_{j=s+1}^{N} \mathcal{V}\left(\vec{x}_i - \vec{x}_j\right) \right] \right\rangle = f^{\mathcal{V}}\left(\vec{x}_i\right) + \Gamma_C\left(t\right) \tag{2.3.11}$$

In this mean field approximation for the bath, we can consider the average force as:

$$\left(N-s\right) \int d^{N-s}\vec{x}\, p\left(\vec{x}\right) \nabla\left(\mathcal{V}\left(\vec{x}_i - \vec{x}\right)\right) \approx \int d\vec{x}\left(c\left(\vec{x}\right) \nabla\left(\mathcal{V}\left(\vec{x}_i - \vec{x}\right)\right)\right. \tag{2.3.12}$$

Where $c\left(\vec{x}\right)$ is the concentration of ions in the bath. Clearly, the average has a fixed mean if the concentration is fixed. In an electrolyte, most electorstatic interactions of this type should cancel out when the concentrations of anions and cations are equal. The mean force therefore becomes increasingly important as the bath deviates from electroneutrality. Approximating interactions with particles outside the nanopore as a mean force and a stochastic force will eventually result in an expression for a convenient probability density for particles in the nanopore only. One of the main goals of this analysis is to understand the effect of interactions between particles in the nanopore, and the approximations made here will significantly facilitate this analysis.

For the moment, let us also assume that the net force from interparticle fluctuations, $f^{\mathcal{V}}$, is a constant, and in particular that it is zero. This term can always be added back in later with ease should it be necessary. Fluctuations, in the spatial positions of particles in equilibrium will be henceforth absorbed into the stochastic force $\Gamma^i\left(t\right) = \Gamma^i_C\left(t\right) + \Gamma^i_W\left(t\right)$. Therefore, we have the following equation for the velocity derivative:

$$\dot{\vec{v}}_i = \frac{1}{m_i}\vec{\nabla}_{\vec{x}_i}\left(\mathcal{U}_{ext}\left(\vec{x}_i\right) + \mathcal{U}_{pore}\left(\vec{x}_i\right) + \sum_{j=1\neq i}^{s} \mathcal{V}\left(\vec{x}_i - \vec{x}_j\right)\right) - \gamma\vec{v}_i - \Gamma^i\left(t\right) \tag{2.3.13}$$

In the majority of systems, the stochastic force is assumed to be uncorrelated white noise, captured by the following properties:

$$\left\langle \Gamma_i\left(t\right)\right\rangle = 0 \tag{2.3.14}$$

$$\left\langle \Gamma_i\left(t\right)\Gamma_i\left(t+\tau\right)\right\rangle = 2\frac{\gamma_i}{m_i}k_B T \tag{2.3.15}$$

Alternative treatments of the system involve explicitly assuming specific kinds of memory functions for the

dynamics - a common one being an exponentially decaying memory function. For now, we are interested in the steady state mass transport across the system, which occurs on timescales, $\tau_{ss} > 10^{-3}s$. In comparison, the timescales for the interactions contributing to $\Gamma_i(t)$ all occur at timescales significantly shorter, $\tau_\Gamma < 10^{-10}s$.

2.3.2 The Kramers-Moyal expansion of the master equation

The continuous master equation for the evolution of this probability density, $\rho_N(\vec{\chi}_1, \vec{\chi}_2, \ldots, \vec{\chi}_N)$ is given by [48]:

$$\frac{\partial \rho_N(\{\vec{\chi}\}, t)}{\partial t} = \int d^N\vec{\chi}' \left[W(\{\vec{\chi}\}|\{\vec{\chi}'\})\rho_N(\{\vec{\chi}'\}, t) - W(\{\vec{\chi}'\}|\{\vec{\chi}\})\rho_N(\{\vec{\chi}\}, t)\right] \tag{2.3.16}$$

Where $\{\chi\}$ refers to the entire set of $(\vec{\chi}_1, \vec{\chi}_2, \ldots, \vec{\chi}_N)$ for N particles in the system. Similar to the discrete case, the function, $W(\{\vec{\chi}'\}, \{\vec{\chi}\})$ is the probability of transitioning between the two states $\{\vec{\chi}'\}$ and $\{\vec{\chi}\}$. By performing a Taylor expansion of the right hand side, the Kramers-Moyal expansion is obtained [48]. Because the complexity of the expressions increases significantly with dimensionality of the equation, in this section the Kramers-Moyal expansions will be written out for several different systems, ranging from one particle, to N particles, in 1-D and in d-D. For a single particle in one-dimension, the Kramers-Moyal expansion is:

$$\frac{\partial \rho_1(\chi, t)}{\partial t} = \sum_{m=1}^{\infty} \frac{(-1)^m}{m!} \left(\frac{\partial}{\partial \chi}\right)^m \left(a^{(m)}(\chi)\rho_1(\chi, t)\right) \tag{2.3.17}$$

The coefficients, $a^{(m)}$ are called the Kramers-Moyal expansion coefficients. Risken's book on the Fokker-Planck equation[45] refers to these coefficients with the notation $D^{(m)}$. The Kramers-Moyal coefficients are given by the correlation function:

$$a^{(m)}(\chi) = \frac{1}{m!} \lim_{\tau \to 0} \frac{1}{\tau} \langle (\xi(t+\tau) - \chi(t))^m \rangle \tag{2.3.18}$$

Where ξ is the stochastic variable in real space that the probability distribution is describing with χ. The actual functions are therefore determined by stochastic differential equations in the physical system for the variable ξ. The Kramers-Moyal expansion of the probability density and coefficients c an also be written for N one dimensional particles[48]. For each value of $m \in \mathbb{Z}^+$, consider the set of integers, $\{j_i\}$ such that $\sum_{k=1}^{N} j_k = m$. The Kramers-Moyal expansion is then given by:

$$\frac{\partial \rho_N(\{\chi\}, t)}{\partial t} = \sum_{m=1}^{\infty} \frac{(-1)^m}{m!} \sum_{i=1}^{N} \left(\frac{\partial}{\partial \chi^i}\right)^{j_i} \left(a^{(m),\{j_i\}}(\{\chi\})\rho_N(\{\chi\}, t)\right) \tag{2.3.19}$$

$$a^{(m),\{j_i\}} = \frac{1}{m!}\lim_{\tau\to 0}\frac{1}{\tau}\left\langle \prod_i^N \left(\xi^i\left(t+\tau\right)-\chi^i\left(t\right)\right)^{j_i}\right\rangle \tag{2.3.20}$$

Where, the superscript, i in ξ^i and χ^i both refer to the i^{th} particle. A superscript is used intentially to distinguish the i^{th} particle from the dimensional components that will be introduced later on. Now consider the Kramers-Moyal expansions are written for d dimensional particle, with no restrictions on correlations between any of the dimensions, and with $\sum_{i=1}^{k} j_k = m$:

$$\frac{\partial \rho_1\left(\vec{\chi}\right)}{\partial t} = \sum_{m=1}^{\infty}\sum_{k=1}^{d}\frac{(-1)^m}{m!}\left(\frac{\partial}{\partial \chi_k}\right)^{\{j_k\}}\left(a^{(m),\{j_k\}}\left(\vec{\chi}\right)\rho_1\left(\vec{\chi},t\right)\right) \tag{2.3.21}$$

$$a^{(m),\{j_k\}}\left(\vec{\chi}\right) = \frac{1}{m!}\lim_{\tau\to 0}\frac{1}{\tau}\left\langle \prod_{i=1}^{k}\left(\vec{\xi}\left(t+\tau\right)-\vec{\chi}\left(t\right)\right)^{j_k}\right\rangle \tag{2.3.22}$$

In each case, we see that the number of expansion coefficients, for a given order m, is proportional to N^m and d^m respectively. The case for N particles, each in a d dimensional space has to be handled with more specificity, primarily because the number of coefficients in this system would scale as $(N \times d)^m$. It has been proven that for Gaussian stochastic variables, the expansion coefficients, $a^{(m)}$ are equal to zero for $m \geq 3$. Even if the stochastic force is not Gaussian, the $m \geq 3$ terms are often very small, and are neglected in virtually all treatments on the subject. Considering only expansion coefficients for N particles in d dimensions up to $m = 2$, the Kramers-Moyal expansion can be written as:

$$\frac{\partial \rho_N}{\partial t} = -\sum_{i=1}^{N}\sum_{k=1}^{d}\left(\frac{\partial}{\partial \chi_k}\right)^i\left(a^{(1,i,k)}\rho_N\right) + \frac{1}{2}\sum_{i=1}^{N}\sum_{j=1}^{N}\sum_{k=1}^{d}\sum_{k'}^{d}\left(\frac{\partial}{\partial \chi_k}\right)^i\left(\frac{\partial}{\partial \chi_{k'}}\right)\left(a^{(2,i,j,k,k')}\rho_N\right) \tag{2.3.23}$$

$$a^{(1,i,k)}\left(\{\vec{\chi}\},t\right) = \lim_{\tau\to 0}\frac{1}{\tau}\left\langle\left(\xi_k^i\left(t+\tau\right)-\chi_k^i\left(t\right)\right)\right\rangle \tag{2.3.24}$$

$$a^{(2,i,j,k,k')}\left(\{\vec{\chi}\},t\right) = \frac{1}{2}\lim_{\tau\to 0}\frac{1}{\tau}\left\langle\left(\xi_k^i\left(t+\tau\right)-\chi_k^i\left(t\right)\right)\times\left(\xi_{k'}^j\left(t+\tau\right)-\chi_{k'}^j\left(t\right)\right)\right\rangle \tag{2.3.25}$$

Note that there are N^2d^2 expansion coefficients for $m = 2$.

2.3.3 Kramers-Moyal in a dual space

The dynamics of a system occurs in a dual space of coupled first order differential equations. This dual space is typically characterized with the position and velocity coordinates, or the position and momentum coordinates. To derive the appropriate evolution of the probability density in the dual space, let us consider a d dimensional space, with $d/2$ position coordinates, q_k and $d/2$ velocity coordinates v_k. The stochastic variables variables will be $\xi_{x,k}$ and $\xi_{v,k}$ for the position and velocity components respectively. The $(N \times d)^2$ expansion coefficients can be re-written with the position and velocity coordinates:

$$a_x^{(1,i,k)}(\vec{x},\vec{v},t) = \lim_{\tau\to 0}\frac{1}{\tau}\left\langle\left(\xi_{x,k}^i(t+\tau) - x_k^i(t)\right)\right\rangle \text{ for } k \in [1, d/2] \tag{2.3.26}$$

$$a_v^{(1,i,k)}(\vec{x},\vec{v},t) = \lim_{\tau\to 0}\frac{1}{\tau}\left\langle\left(\xi_{v,k}^i(t+\tau) - v_k^i(t)\right)\right\rangle \text{ for } k \in [1, d/2] \tag{2.3.27}$$

$$a_{xx}^{(1,i,j,k,k')}(\vec{x},\vec{v},t) = \frac{1}{2}\lim_{\tau\to 0}\frac{1}{\tau}\left\langle\left(\xi_{x,k}^i(t+\tau) - x_k^i(t)\right)\times\left(\xi_{x,k'}^j(t+\tau) - x_{k'}^j(t)\right)\right\rangle \text{ for } k \in [1, d/2] \tag{2.3.28}$$

$$a_{xv}^{(1,i,j,k,k')}(\vec{x},\vec{v},t) = \frac{1}{2}\lim_{\tau\to 0}\frac{1}{\tau}\left\langle\left(\xi_{x,k}^i(t+\tau) - x_k^i(t)\right)\times\left(\xi_{v,k'}^j(t+\tau) - v_{k'}^j(t)\right)\right\rangle \text{ for } k \in [1, d/2] \tag{2.3.29}$$

$$a_{vv}^{(1,i,j,k,k')}(\vec{x},\vec{v},t) = \frac{1}{2}\lim_{\tau\to 0}\frac{1}{\tau}\left\langle\left(\xi_{v,k}^i(t+\tau) - x_v^i(t)\right)\times\left(\xi_{v,k'}^j(t+\tau) - v_{k'}^j(t)\right)\right\rangle \text{ for } k \in [1, d/2] \tag{2.3.30}$$

Each sum over d coordinates in equation 2.3.2 can be split into two sums over $d/2$ coordinates. These terms are written explicitly below:

$$\sum_{k=1}^{d}\frac{\partial}{\partial\chi_k}\left(a^{(1,i,k)}\rho_N\right) = \sum_{k=1}^{d/2}\left(\frac{\partial}{\partial x_k}\right)^i\left(a_x^{(1,i,k)}\rho_N\right) + \left(\frac{\partial}{\partial v_k}\right)^i\left(a_v^{(1,i,k)}\rho_N\right) \tag{2.3.31}$$

$$\left(\frac{\partial^i}{\partial\chi_k}\frac{\partial^j}{\partial\chi_{k'}}\right)a^{(2,i,j,k,k')}\rho_N = \left(\frac{\partial^i}{\partial x_k}\frac{\partial^j}{\partial x_{k'}}\right)a_{xx}^{(2,i,j,k,k')}\rho_N + 2\left(\frac{\partial^i}{\partial x_k}\frac{\partial^j}{\partial v_{k'}}\right)^j a_{xv}^{(2,i,j,k,k')}\rho_N + \left(\frac{\partial^i}{\partial v_k}\frac{\partial^j}{\partial v_{k'}}\right)a_{vv}^{(2,i,j,k,k')}\rho_N \tag{2.3.32}$$

2.3.4 Langevin SDE to the Klein Kramers PDE

The Kramers-Moyal coefficient expansion can be used to obtain partial differential equations for the probability density for a large range of stochastic differential equations[45, 48], of the form:

$$\frac{\partial \xi_k^i}{\partial t} = A_k^i\left(\{\xi\}, t\right) + \sum_j \sum_{k'} B_{k,k'}^{ij}\left(\{\xi\}, t\right) \Gamma_k^i\left(t\right) \tag{2.3.33}$$

Where $\Gamma\left(t\right)$ is a Gaussian, stochastic force satisfying:

$$\left\langle \Gamma_i^k\left(t\right)\right\rangle = 0 \tag{2.3.34}$$

$$\left\langle \Gamma_i^k\left(t+\tau\right)\Gamma_j^{k'}\left(t\right)\right\rangle = 2\gamma_i^k \frac{k_B T}{m} \delta\left(k-k'\right)\delta\left(i-j\right)\delta\left(\tau\right) \tag{2.3.35}$$

Generally, the $B_{k,k'}^{ij}$ matrix allows for a set of equations much more complicated than we need to solve. Let us now consider the solution for N particles, with $d/2$ spatial and velocity dimensions, satisfying two first order stochastic differential equations:

$$\dot{x}_k^i = v_k^i \tag{2.3.36}$$

$$\dot{v}_k^i = F_k^i\left(\{x_k^i, x_{k'}^j\}, t\right) - \gamma_k^i v_k^i + \Gamma_k^i\left(t\right) \tag{2.3.37}$$

The coefficients can be shown to be:

$$a_x^{(1,i,k)} = v_k^i \tag{2.3.38}$$

$$a_v^{(1,i,k)} = F_k^i\left(\{x_k^i, x_{k'}^j\}, t\right) - \gamma_k^i v_k^i \tag{2.3.39}$$

$$a_{xx}^{(2,i,j,k,k')} = a_{xv}^{(2,i,j,k,k')} = 0 \tag{2.3.40}$$

$$a_{vv}^{(2,i,j,k,k')} = \gamma_k^i \frac{k_B T}{m_i} \delta\left(k-k'\right)\delta\left(i-j\right) \tag{2.3.41}$$

The equation for the evolution of the probability density is obtained, and in literature often referred to as the Klein-Kramers equation:

$$\frac{\partial \rho_N}{\partial t} = \sum_{i=1}^{N}\sum_{k=1}^{d/2}\left(\frac{\partial}{\partial v_k}\right)^i\left(\left(F_k^i\left(\{x_k^i, x_{k'}^j\}, t\right) - \gamma_k^i v_k^i\right)\rho_N\right) + \left(\frac{\partial}{\partial x_k}\right)^i (v_k^i \rho_N) + \sum_{i=1}^{N}\sum_{k=1}^{d/2}\left(\frac{\partial}{\partial v_k^i}\frac{\partial}{\partial v_k^i}\right)\left(\gamma_k^i \frac{k_B T}{m}\rho_N\right) \tag{2.3.42}$$

2.4 Computing transport properties from the probability density

2.4.1 Smoluchowski equation

A great deal of insight into mass transport can be gained from the derivations in the previous sections. In contrast to the deterministic dynamics described by the Hamiltonian, a stochastic differential equation is obtained for the equations of motion when fast degrees of freedom are averaged over. In the condensed matter systems of interest, the fastest degrees of freedom correspond to the dynamics of solvent molecules, and the stochastic differential equation describes the motion of all solute particles. Furthermore, most condensed matter systems operate in the limit of high friction, which is mathematically modeled by setting the $m\ddot{v}$ term to zero. In the high friction limit, the Smoluchowski equation is obtained instead of the Klein-Kramers equation. Going through a similar derivation as performed in the last section, and assuming that the diffusion tensor is diagonal, with no cross-correlations between particles that are induced by hydrodynamic coupling, yields (in vector notation, again extended to N particles):

$$\frac{\partial \rho_N}{\partial t} = \sum_{i=1}^{N}\sum_{k=1}^{d/2}\left(-\frac{D_k^i}{k_B T}\frac{\partial}{\partial x_k}\right)(F_k^i \rho_N) + \sum_{i=1}^{N}\sum_{k=1}^{d/2}\left(\sqrt{D_k^i}\frac{\partial}{\partial x_k}\right)^i\left(\sqrt{D_k^i}\frac{\partial}{\partial x_k}\right)^i \rho_N \tag{2.4.1}$$

In vector notation, equation 2.4.1 can be written compactly as[49]:

$$\frac{\partial \rho_N}{\partial t} = \sum_{i=1}^{N}\vec{\nabla}\cdot\left[\mathbf{D}^i\left(-\frac{1}{k_B T}\vec{F}^i\rho_N + \vec{\nabla}\rho_N\right)\right] \tag{2.4.2}$$

Moving the sum into the divergence, the Smoluchowski equation can be written as a probability conservation equation of the form:

$$\frac{\partial \rho_N}{\partial t} = \vec{\nabla}\cdot\vec{J} \tag{2.4.3}$$

Where the probability current, $\vec{J}$ is given by:

$$\vec{J} = \sum_{i=1}^{N}\vec{J}^i = \sum_{i=1}^{N}\mathbf{D}^i\left(-\frac{1}{k_B T}\vec{F}^i\rho_N + \vec{\nabla}\rho_N\right) \tag{2.4.4}$$

Let us consider forces of the form:

$$\vec{F}^i = -\vec{\nabla}\left(\mathcal{U}\left(\vec{x}^i\right) + \mathcal{V}\left(\vec{x}^i - \vec{x}^j\right)\right) \tag{2.4.5}$$

In general, of interest is how the terms $\mathcal{U}$ and $\mathcal{V}$ determine the net current through a graphene nanopore. We will further assume that the diffusion tensor $\mathbf{D}^i$ is diagonal.

2.4.2 Geometric solutions to transport properties

A nanopore's function is defined by the transport properties of ions in solution. Calculating the net probability current through the nanopore, $I = \int dA\, \vec{J}$ as a function of applied voltage, concentration, and other experimental parameters is of primary interest. Furthermore, in industrial separations, we are often interested in the steady state properties of the nanopore, in which case, $\frac{\partial \rho_s}{\partial t} = 0$, and for all particles, $\nabla \cdot \vec{J}^i = 0$. In the two dimensional coordinate system, we therefore have the general relation that (in steady state):

$$\frac{\partial \vec{J}^i \cdot \hat{r}}{\partial r} + \frac{\partial \vec{J}^i \cdot \hat{z}}{\partial z} = 0 \tag{2.4.6}$$

Furthermore, in steady state, the quantity $\vec{J}$ is also time invariant, i.e. $\frac{\partial \vec{J}}{\partial t} = 0$. The problem is only well defined if the probability is defined on the boundaries, and the potential function is known everywhere in space.

$$\rho_s\left(r, z = \pm L_p/2\right) = \rho_N^{\pm L/2}\left(r\right) \tag{2.4.7}$$

Computation of the potential function should be possible given the small number of ions in a graphene nanopore. Chapter 4 will cover methods of computing this potential for the single ion case, with the hope that the methods developed there can be generalized in the future to computing the potential across the entire phase space with a small number of ions in the pore.

On the radial boundaries, $r_p - r_i$, where r_i is the hard-sphere radius of an ion, the radial probability flux must vanish:

$$\vec{J}^i\left(r = r_p - r_i, z\right) \cdot \hat{r} = 0 \tag{2.4.8}$$

The conditions above fully specify solutions for the probability density and the flux. The electric driving force that establishes the non-equilibrium transport is included in the single particle potential $\mathcal{U}\left(\vec{x}_i\right)$ and need not be specified until Chapter 4. We note here that at each coordinate $(r = r_p - r_i, z)$, one can draw

an unique surface where the flux, $\vec{J}^i = const.$ Let each of these surfaces be specified with the notation ∂S_{r_p}. For each of these surfaces, there furthermore exists a tangent vector, $\hat{t}_{r_p}(r,z)$ and a normal vector $\hat{n}_{r_p}(r,z)$. In the direction of the tangent vector, the projection of the flux is zero:

$$\vec{J}^i \cdot \hat{t}^i_{r_p} = 0 \tag{2.4.9}$$

The zero flux relationship is vital, as it allows for partial computation of the probability density. Recall that:

$$\vec{J}^i = D^i \left(-\frac{1}{k_B T} \vec{F}^i \rho_N + \vec{\nabla}^i \rho_N \right) \tag{2.4.10}$$

Along the tangent, we therefore have:

$$0 = -\frac{1}{k_B T} \vec{\nabla}\varphi \cdot \hat{t}^i_{r_p} \rho_N + \left(\vec{\nabla}^i \rho_N \right) \cdot \hat{t}^i_{r_p} \tag{2.4.11}$$

While in the normal direction, the surface is a surface of constant flux:

$$J_n = -\frac{1}{k_B T} \vec{\nabla}\varphi \cdot \hat{n}^i_{r_p} \rho_N + \left(\vec{\nabla}^i \rho_N \right) \cdot \hat{n}^i_{r_p} \tag{2.4.12}$$

Equation 2.4.2 requires a lot of further work before it is used to compute the probability density explicitly. However, it provides clear insight on how to relate equilibrium properties of the system to non-equilibrium properties. In equilibrium, there is a well defined relationship between the potential and the density, and at least part of the equilibrium solution can be used to interpret the dynamical properties of the system. This observation will be used in the next section to solve explicitly for transport int he case of $s = 1$

2.4.3 Solving for the current for the single particle distribution

Similar to the approach taken in the BBGKY heirarchy, the first step to understanding the implications of the equation set (consituted by both the reduced master equation and the Nernst-Planck equation on the probability densities) is to solve for the single particle density where $s = 1$. This section, however, substitutes for the probability density the concentration of the ionic species, and as a result the Nerst-Planck equation is found in a more familiar form:

$$\vec{J}^C_i = -D_i \left(\vec{\nabla} c_i + \frac{c_i}{k_B T} \vec{\nabla} \varphi^{s=1}_i (r,z) \right) \tag{2.4.13}$$

The flux, $\vec{J}^C$ is now the number flux, and not the probability flux as it was in the previous chapter. The

potential in this case is the single particle potential, which does not include any pair interactions. Throughout the remainder of this section, the number flux will be written simply as $\vec{J}$, and the single particle potential as $\varphi_i(r,z)$. The index i is retained to indicate that the fluxes still depend on the type of ion. Another interpretation of the solution to this Nernst-Planck equation is not the $s=1$ solution, but also the solution for non-interacting particles in the nanopore. The correspondence between the two is not likely a coincidence. The net current, which is the measured quantity in experiments, is given by net current across the nanopore $I_i = \int_0^{r_P - r_I} J_i^z(r)\, r dr$. Finally, the coordinate $\hat{z}$ will also be called the transmembrane coordinate.

Boundary conditions and continuity

The boundary conditions for this equation are known concentrations at the entrance $c(r, z=-L/2)$ and exit $c(r, z=L/2)$ of the nanopore, and a no flux condition at the perimeter of the nanopore, $\vec{J}(r=r_p-r_i, z)\cdot\hat{r}=0$, where r_p is the radius of the pore and r_i is the radius of the ion.

In the interior of the nanopore, there is a known potential $\varphi(r,z)$, and the continuity equation $\frac{\partial c}{\partial t} = \vec{\nabla}\cdot\vec{J}$ holds. In the case of steady state, this reduces to:

$$\vec{\nabla}\cdot\vec{J}=0 \tag{2.4.14}$$

$$\frac{\partial J_i^z(r,z)}{\partial z} + \frac{\partial J_i^r(r,z)}{\partial r} = 0 \tag{2.4.15}$$

In the last equation above, the superscript, r and z refer to the projections of the vector in the $\hat{r}$ and $\hat{z}$ directions respectively. To obtain an analytically solvable expression, a further simplication is made - that $\varphi(r, z=\pm L/2)$ and $c(r, z=\pm L/2)$ have weak radial dependence just outside the nanopore, at least compared to the radial dependence in the nanopore. In this approximation, at the boundary $(r, z=\pm L/2)$, both the derivatives $\frac{\partial\varphi}{\partial r}(r, z=\pm L/2)$ and $\frac{\partial c}{\partial r}(r, z=\pm L/2)$ are approximately zero, and the radial flux, $\vec{J}\cdot\hat{r}\approx 0$ and $\frac{\partial\vec{J}\cdot\hat{r}}{\partial r}\approx 0$ at the entrance and exit. In this approximation, continuity (equation 2.4.3) requires that the derivative be zero, and the function itself is zero. At the nanopore boundary, both the radial flux and its derivative are zero, and consequently, the radial flux at all radial coordinates must be:

$$J_i^r(z)=0 \tag{2.4.16}$$

For the continuity equation, this implies that:

$$\frac{\partial J_i^z(r,z)}{\partial z} = \frac{\partial J_i^r(r,z)}{\partial r} \tag{2.4.17}$$

$$\int \frac{\partial J_i^z(r,z)}{\partial z} dz = J_i^z(r) \tag{2.4.18}$$

Nernst-Planck equation in the radial coordinate

The vanishing radial ionic flux enables a relationship to be derived between the potential and the concentration directly from the Nernst-Planck equation:

$$0 = J_i^r(z) = -D\left(\vec{\nabla}c + \frac{c}{k_B T}\vec{\nabla}\varphi\right)\cdot\vec{r} \tag{2.4.19}$$

$$0 = J_i^r(z) = -D\left(\frac{\partial c}{\partial r} + \frac{c}{k_B T}\frac{\partial \varphi}{\partial r}\right) \tag{2.4.20}$$

$$\frac{\partial c(r,z)}{\partial r} = -\frac{c(r,z)}{k_B T}\frac{\partial \varphi(r,z)}{\partial r} \tag{2.4.21}$$

Let us now define a function, $\chi(r,z)$ such that:

$$c(r,z) = c_0 \exp\left(-\chi(r,z)/k_B T\right) \tag{2.4.22}$$

Using this definition:

$$\frac{c_0}{k_B T}\frac{\partial \chi(r,z)}{\partial r}\exp\left(-\chi(r,z)/k_B T\right) = \frac{c_0}{k_B T}\exp\left(-\chi(r,z)/k_B T\right)\frac{\partial \varphi(r,z)}{\partial r} \tag{2.4.23}$$

$$\frac{\partial \chi(r,z)}{\partial r} = \frac{\partial \varphi(r,z)}{\partial r} \tag{2.4.24}$$

$$\chi(r,z) = \varphi(r,z) + \beta(z) \tag{2.4.25}$$

Inserting this result back into equation 2.4.3:

$$c(r,z) = c_0 \exp\left(-\left(\varphi(r,z) + \beta(z)\right)/k_B T\right) \tag{2.4.26}$$

$$c(r,z) = c_0 \exp\left(-\beta(z)/k_BT\right) \exp\left(-\varphi(r,z)/k_BT\right) \tag{2.4.27}$$

Finally, we note that the function $\beta(z)$ is ultimately going to be determined by the concentration boundary conditions across the nanopore.

$$\exp\left(-\beta(z)/k_BT\right) = \frac{c(r,z)}{c_0} \exp\left(\varphi(r,z)/k_BT\right) \tag{2.4.28}$$

$$\frac{-c_0}{k_BT}\frac{\partial\beta}{\partial z} \exp\left(-\beta(z)/k_BT\right) = \frac{\partial c(r,z)}{\partial z} \exp\left(\varphi(r,z)/k_BT\right) + \frac{1}{k_BT}\frac{c(r,z)}{c_0}\frac{\partial\varphi(r,z)}{\partial z} \exp\left(\varphi(r,z)/k_BT\right) \tag{2.4.29}$$

Nernst-Planck equation in the transmembrane coordinate

$$J_i^z(r) = -D\left(\frac{\partial c(r,z)}{\partial z} + \frac{c}{k_BT}\frac{\partial\varphi(r,z)}{\partial z}\right) \tag{2.4.30}$$

Using the solution for the concentration from the radial coordinate:

$$J_i^z(r) = -\frac{D}{k_BT}\left(-\left(\frac{d\beta}{dz} + \frac{\partial\varphi(r,z)}{\partial z}\right)c(r,z) + c(r,z)\frac{\partial\varphi}{\partial z}\right) \tag{2.4.31}$$

Remarkably, this simplifies to:

$$J_i^z(r) = -\frac{D}{k_BT}\frac{d\beta}{dz}c(r,z) \tag{2.4.32}$$

$$J_i^z(r) = -\frac{Dc_0}{k_BT}\frac{d\beta}{dz} \exp\left(-\beta(z)/k_BT\right) \exp\left(-\varphi(r,z)/k_BT\right) \tag{2.4.33}$$

From this equation, we now solve for the total current across the nanopore:

$$I = \int_0^{r_P - r_I} J_i^z(r)\, rdr = -\frac{Dc_0}{k_BT}\frac{d\beta}{dz} \exp\left(-\beta(z)/k_BT\right) \int_0^{r_P - r_I} \exp\left(-\varphi(r,z)/k_BT\right) rdr \tag{2.4.34}$$

For convenience, we define the radial averaged nanopore potential, which can be computed directly from $\varphi(r,z)$:

$$\left(\pi\left(r_P - r_I\right)^2\right) \exp\left(-\frac{\bar{\varphi}(z)}{k_BT}\right) = \int_0^{r_P - r_I} \exp\left(-\varphi(r,z)/k_BT\right) rdr \tag{2.4.35}$$

Solving for this radial averaged nanopore potential:

$$\bar{\varphi}(z) = -k_B T \log\left[\frac{1}{\left(\pi\left(r_P - r_I\right)^2\right)}\int_0^{r_P - r_I} \exp\left(-\varphi(r,z)/k_B T\right) r dr\right] \tag{2.4.36}$$

$$I = \frac{Dc_0}{k_B T}\pi\left(r_P - r_I\right)^2 \frac{d\beta}{dz}\exp\left(-\left(\beta(z) + \bar{\varphi}(z)\right)/k_B T\right) \tag{2.4.37}$$

In steady state, the current is a constant and independent of z. We now have a fully specified set of equations to solve for the function $\beta(z)$. In particular, we have that:

$$\frac{d\beta}{dz}\exp\left(-\left(\beta(z) + \bar{\varphi}(z)\right)/k_B T\right) = \xi \tag{2.4.38}$$

The parameter ξ is directly related to the current by:

$$I = \xi \times \frac{Dc_0}{k_B T}\pi\left(r_P - r_I\right)^2 \tag{2.4.39}$$

Separation of variables yields:

$$d\beta \exp\left(-\beta/k_B T\right) = \xi \exp\left(\bar{\varphi}(z)/k_B T\right) dz \tag{2.4.40}$$

$$\exp\left(-\beta\left(\frac{L}{2}\right)/k_B T\right) - \exp\left(-\beta\left(-\frac{L}{2}\right)/k_B T\right) = -\frac{\xi}{k_B T}\int_{-L/2}^{L/2} \exp\left(\bar{\varphi}(z)/k_B T\right) dz \tag{2.4.41}$$

Using the definition of the function $\beta(z)$ in equation 2.4.3:

$$\frac{c\left(r,\frac{L}{2}\right)}{c_0}\exp\left(\varphi\left(r,\frac{L}{2}\right)/k_B T\right) - \frac{c\left(r,-\frac{L}{2}\right)}{c_0}\exp\left(\varphi\left(r,-\frac{L}{2}\right)/k_B T\right) = -\frac{\xi}{k_B T}\int_{-L/2}^{L/2} \exp\left(\bar{\varphi}(z)/k_B T\right) dz \tag{2.4.42}$$

Solving for the current, we obtain:

$$I = D\pi\left(r_P - r_I\right)^2 \frac{c\left(r,\frac{L}{2}\right)e^{\varphi\left(r,-\frac{L}{2}\right)/k_B T} - c\left(r,\frac{L}{2}\right)e^{\varphi\left(r,-\frac{L}{2}\right)/k_B T}}{\int_{-L/2}^{L/2}\exp\left(\bar{\varphi}(z)/k_B T\right) dz} \tag{2.4.43}$$

To obtain the concentration field, the equation 2.4.3 is integrated from one (known) end of the pore, to an arbitrary position, z:

$$\frac{c\left(r,\frac{L}{2}\right)}{c_0}\exp\left(\varphi\left(r,\frac{L}{2}\right)/k_BT\right)-\frac{c\left(r,z\right)}{c_0}\exp\left(\varphi\left(r,z\right)/k_BT\right)=-\frac{\xi}{k_BT}\int_{-L/2}^{z}\exp\left(\bar{\varphi}\left(z'\right)/k_BT\right)dz' \quad (2.4.44)$$

$$c\left(r,z\right)=c\left(r,\frac{L}{2}\right)\exp\left(\varphi\left(r,\frac{L}{2}\right)/k_BT\right)+\frac{I}{D\times\pi\left(r_P-r_I\right)^2}\int_{-L/2}^{z}\exp\left(\bar{\varphi}\left(z'\right)/k_BT\right)dz' \quad (2.4.45)$$

Comments

The solution provided above makes a number of approximations even after its derivation - in particular, the one on the radial dependence of the concentration and potential outside the nanopore. As we will see in Chapter 4, the nanopore potential has its largest values inside the pore, and therefore the approximation that the potential and concentration have weak radial dependence is a decent first order approximation. This approximation is not necessarily valid, however, for the case of $s > 1$, where there are interactions between particles.

The solution, however, is quite powerful in that it provides a method of analytically relating the potential in the nanopore to the net current and the concentration profiles. This allows for very efficient estimation of nanopore properties from the structure of a nanopore. From analysis of this solution in Chapter 4, we will see that it predicts a wide range of interesting transport characteristics that capture many of the essential features of experiments performed in Chapter 3.

Finally, the solution also provides an understanding of the *structurally endogenous* behavior of a graphene nanopore - where *structurally endogenous* refers to those behaviors arising spefically from the structure of the nanopore. The structure-function relationship that is so often discussed in ion channel literature fundamentally assumes that the structure of a nanopore - and not inter-ionic interactions - gives rise to the selectivity properties observed in the channels. The solution for $s = 1$ completely neglects interactions between ions and therefore captures only those behaviors expected to emerge from a structural description of the pore.

Chapter 3

Experimental measurement of ion transport in graphene pores

The emergence of two-dimensional materials has opened up new avenues for experimental research into transport of matter through highly confined geometries. Although biological ion channels have been studied experimentally for decades, their structure - and by design, their chemical affinity - is extremely heterogeneous along the length of the nanopore. As a result, it has been very difficult to predict the properties of biological ion channels from physical toy models. Instead, researchers have been forced to explain transport properties of biological ion channels from the specific atomic configurations found from diffraction studies.

In direct contrast, two-dimensional nanopores present a markedly simpler atomic description. The number of atoms defining the nanopore structure - as well as the nanopore volume - is smaller than any other conceivable nanopore. The lattice structure of the nanopores provides significant prior information about the nanopore structure, and, in the absence of chemical functionalization, a homogeneity in the atomic structure of the nanopore. It is therefore likely that the simple descriptions of ion transport developed in Chapter 2 can be used to understand the transport of ions through graphene nanopores. Nonetheless, that any analytic treatment involves a large number of approximations. There is absolutely no substitute for the ability to experimentally measure the transport properties of individual nanopores. Measurement of current through single graphene nanopores directly provides us with a solution to the complete set of physical equations, without approximation. This chapter, therefore, develops an experimental methodology for measuring single graphene nanopores, and summarizies a large number of measurements taken on single nanopores.

This chapter will also provide an introduction to the experimentally measured transport properties of single graphene nanopores, including the linearity of their current-voltage response, preliminary data on

ionic selectivity, and time dependence to their behavior.[1]

3.1 Statistical isolation of graphene nanopores

In 1976, Neher and Sakmann reported on a method to isolate individual ion channels in a cell membrane by developing a technique now known as the patch-clamp[37]. In doing so, uncovered one of the hallmark behaviors of individual ion channels, stochastic switching between different conductance states. For their efforts, the duo won the Nobel Prize in Physiology or Medicine in 1991, and created an entire industry of single ion channel electrophysiological measurements that has been responsible for major advances in the understanding of the behaviors and mechanisms of transport in biological in channels.

Underlying the ubiquitous patch-clamp method is the principle of statistical isolation. A cell, with a diameter on the order of $5\,\mu m$ has roughly 50 ion channels distributed across its surface. This corresponds to a density of ion channels on the order of $2\,\mu m^{-2}$. Using a glass nanopipette with a small enough diameter, there is a high probability that one will get one or fewer ion channels in the probed area. While it is possible to guarantee a single channel by using feedback-controlled exposure of protein channels to reconstituted lipid bilayers, statistical isolation remains till date the only method of probing single channels in cell membranes.

Generalizing this observation, *single channel resolution on any membrane with existing defects will likely rely on the principles of statistical isolation.* In the context of graphene membranes, one can introduce nanopores using electron or ion beam irradiation. The measurements, however, should only be considered valid if there are no other nanopores from intrinsic defects in the graphene materials. This condition again would need to be checked using the simple principles of statistical isolation. In fact, multiple experimental reports on intentionally created graphene nanopores report the existence of "leakage currents" from defects due to the large area under test. Inspired by the patch-clamp technique, and given that defects with sub-2 nm in diameter already exist in chemical vapor deposition grown graphene, we decided to adopt statistical isolation of intrinsic defects as our method of measuring single graphene nanopores.

3.1.1 Concept for statistical isolation of graphene nanopores

The experimental approach adopted in this thesis is based on statistical isolation of individual nanopores in graphene. Statistical isolation of individual nanopores occurs when the probability of finding a nanopore in the membrane area under test is less than one. The technique therefore requires some knowledge of the density of nanopores in a membrane and an ability to control the area of the membrane under test. This

[1] Scanning transmission electron microscope images presented in this thesis were taken by Dr. Sean O'Hern and Dr. Juan-Carlos Idrobo at Oak Ridge National Laboratories.

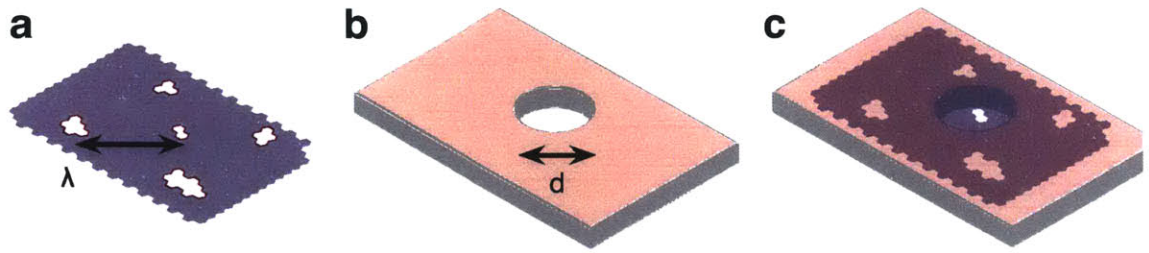

Figure 3.1.1: Statistical isolation of graphene nanopores (a) CVD graphene with a mean distance $\hat{\lambda}$ of sub-continuum nanopores. (b) Silicon nitride nanopore with a diameter d. (c) CVD graphene suspended over the silicon nitride nanopore. When $\hat{\lambda} > d$, statistical isolation of graphene nanopores occurs.

required relationship is mathematically expressed as:

$$\hat{\sigma}\left(\frac{\pi d^2}{4}\right) < 1 \tag{3.1.1}$$

Variable	Description
$\hat{\sigma}$	Density of defects, nanopores per unit area
d	Diameter of the support hole
$\hat{\lambda} = \left(\frac{4\hat{\sigma}}{\pi}\right)^{-1/2}$	Effective spacing between defects
$\hat{\lambda}_M$	Estimated defect density from measurements
$\Delta\hat{\lambda} = \hat{\lambda} - \hat{\lambda}_M$	Variation from measured
d_T	Diameter of support hole used for testing

By combining gas permeation measurements across multiple layers of graphene, scanning transmission electron microsope (STEM) imaging of the defect distribution, and a parametric model for gas transport, the density of nanopores in the graphene, $\hat{\lambda}_M \in (70, 100)\, nm$ was estimated for CVD graphene[24]. Although this estimate of $\hat{\sigma}_M$ will be used going forward, there are some limitations with the estimation. Specifically, batch to batch and area uniformity variations (collectively, $\Delta\hat{\lambda}$) of the defect density and the is not known. Furthermore, larger nanopores have much higher permeation rates than smaller nanopores, and particularly so in gas phase transport. Therefore, it is likely that the estimates of the defect density provide a more accurate estimate of defects at the tail of the distribution (larger nanopores) rather than the mode (typically around 0.8 - 1 nm diameter). To compensate for the likelihood that the density of sub-2 nm defects was larger than measured, it was therefore chosen to use a graphene area under test with $d_T = 40nm < \hat{\lambda}_M$, and with $\hat{\sigma}_M\left(\frac{\pi d^2}{4}\right) \approx \frac{1}{3}$.

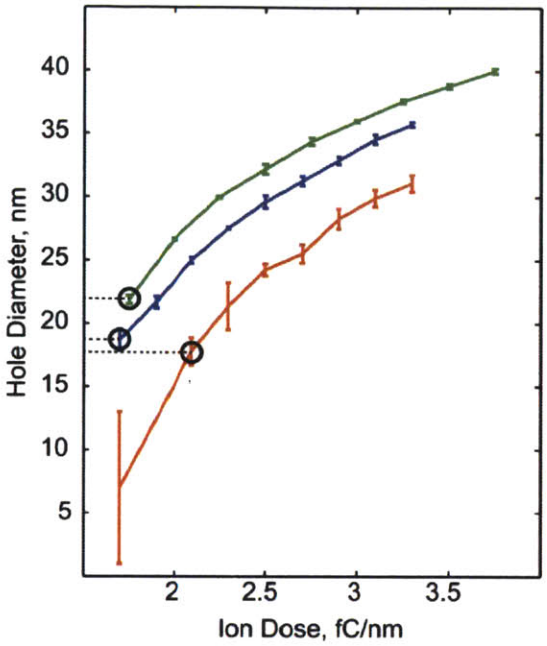

Figure 3.1.2: Relationship between Ga^+ dose and diameter of SiN_x membranes for an ion beam current of 1.5pA and accelerating voltage of 30kV. Green, blue, and red data represent 50, 20, and 10nm thick membranes respectively. The black circle represents the size of the smallest reproducibly created feature.

In principle, statistical isolation is not mutually exclusive with using electron imaging techniques to characterize any nanopores in the area under test. In practice, however, finding a single support hole with $d_T = 40nm$ in a larger $O\,(10\mu m)$ membrane is time-consuming, and finding all of the defects in the suspended graphene area equally challenging. Equally importantly, access to 80kV, aberration corrected STEM with $\AA$ resolution of light elements is extremely limited. From STEM images of graphene, it was also clear that hydrocarbon contamination is often present on the surface of graphene, and there was no guarantee that contamination would prevent measurement of the entire free-standing area when attempting to characterize all nanopores present in the area. As a result, no attempts were made to correlate STEM images of nanopores in CVD graphene with samples used to measure ion transport.

3.1.2 Fabrication of Silicon Nitride support structures

Silicon nitride membranes (SiNx) , 50 nm thick, with a 100 μm membrane area (TEMwindows, SN100-A50Q33) were chosen for the support material, and a single support hole was patterned in using a Ga+ Focused Ion Beam (Helios 600) in the center of the central membrane. The dose was calibrated to ensure that the diameter of the support hole was consistently between 30 and 40 nm[50] (Figure 3.1.2). For the highest patterning resolution, the maximum accelerating voltage of the instrument (30kV) was used to maximize

the probability of sputtering, while the smallest beam current (1.5pA) was used to reduce the width of the incident ion beam. Still, achieving consistent results with ion beam milling requires that the ion beam is properly focused and corrected for astigmation. The small beam current and high accelerating voltage means that image contrast on the relatively insulating silicon nitride layer makes finding the right focus difficult. In many cases, other research groups use samples with gold nanoparticles or other conducting features to focus the beam. Instead of this, small chips of conductive silicon debris near the edge of the TEM grid were used to fix the focus and stigmation of the ion beam. It is important that the eutectic height calibration (where the eutectic height is, by design of the manufacturer, the height of the sample at which optimal performance for both the ion beam and electron beam is obtained) is done as close as possible to the feature being used to focus the ion beam. If the eutectic height calibration is performed far away from the milling site - even a distance of 300 μm is considered far - then the tilt of the TEM grid from its mounting will cause the ion beam to be inadequately focused. Finally, to ensure repeatability of ion beam milling between sessions, a dose size calibration is milled into a spare membrane in each session. Nanopore milling doses and diameters are spot checked with the electron beam.

3.1.3 Unique ability to use vacancy defects as nanopores for mass transport in 2D materials

Two dimensional materials are a unique class of materials in which vacancy defects are inherently potential conduits for mass transport across the material. The equivalence of vacancy defects and nanopores in graphene provides access to a large variety, and parameter space, for making solid-state nanometers with diameters below sub-2 nm. Of the top-down methods used for fabrication of solid-state nanopores, ion and electron[51, 52, 53] bombardment is most common. The lateral resolution is known to depend strongly on the thickness of the material[50], pre-dominantly owing to atomic recoil, scattering, redeposition, and ion implantation[54, 55]. When the same techniques are applied on graphene, atom by atom control over the nanopore diameter has been demonstrated (citation), and theoretical predictions indicate that the statistical properties of vacancy defect distributions - and local amorphous carbon distributions - can be controlled through the ion energy, angle of incidence, and mass[56]. Chemical etching of graphene lattices pristine[20] and disrupted by ion bombardment[22] has also been used to create sub-nm pores in graphene.

Unique to two-dimensional materials, however, is that vacancy defects intentionally generated through the graphene synthesis process itself have the potential to create high density distributions of sub-2 nm nanopores. Nanopores formed during the chemical vapor deposition (CVD) synthesis graphene have been reported, and generated during some attempts at dopoing graphene[23]. The potential for engineered nanopore distributions

generated directly during the growth process has largely been overlooked, however, as most CVD studies are motivated by low cost, high quality graphene for electrical and optical properties.

A mathematical description of nanopores as an ensemble of vacancy defects clearly indicates why the ability to use vacancy defects as nanopores is unique to two dimensional materials. Consider the set of all possible vacancy defect configurations in the any membrane material, $\Omega_N(\vec{x}_k)$ where $\vec{x}_k$ denotes the positions of the number of atoms removed $1 \leq k \leq N$. A potential conduit for mass transport across the material of thickness L occurs if the following conditions are met:

$$\exists\, \nu_1 \in [1, N]\ s.t.\ \vec{x}_{\nu_1} \cdot \hat{z} = \frac{d_{C-C}}{2} \tag{3.1.2}$$

$$\exists\, \nu_M \in [1, N]\ s.t.\ \vec{x}_{\nu_M} \cdot \hat{z} = L - \frac{d_{C-C}}{2} \tag{3.1.3}$$

$$\exists\, \{\nu_m\}\ with\ m \in [1, M]\ s.t.\ \left(\vec{x}_{\nu(m)} \cdot \vec{x}_{\nu(m+1)} = d_{C-C}^2\right) \forall m \tag{3.1.4}$$

In other words, a set of neighboring atoms needs to be removed *across the entire thickness* of a material to form a nanopore and enable mass transport across the membrane. For *random* distributions of vacancy defects during material synthesis, co-location of nearest neighbor vacancy defects across the length of a material (a full pinhole defect) is to first order proportional to the probability of finding a single defect, p_d. Maintaining mechanical integrity of the material generall means that p_d should be relatively low. For a nanopore with M atoms removed, the probability of co-locating those vacancies roughly scales as:

$$p_{nanopore} \sim p_d^M \tag{3.1.5}$$

Clearly, any appreciable density of nanopores in a membrane can only be formed for very large vacancy densities. However, in graphene, random vacancy defects satisfy all of the criteria simultaneously for $M = 1$. This means that distributions of sub-2 nm nanopores can be created simply by relying on entropic drivers for vacancy defect generation during synthesis of graphene. For chemical vapor deposition (CVD) synthesis of graphene alone, there is a huge parameter space that can be tailored to optimize the distribution of nanopore structures (both geometric configurations and functional groups), and consequently optimize the distribution of nanopore functional characteristics.

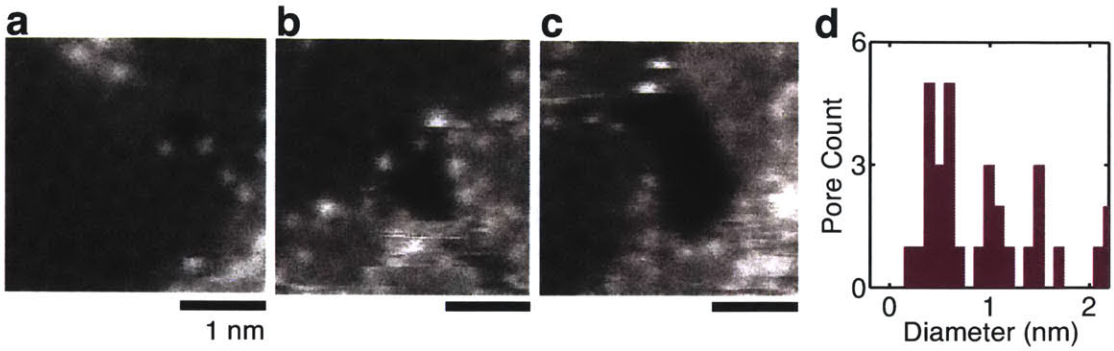

Figure 3.1.3: (a-c) STEM images of sub-2 nm nanopores in graphene. (d) Distribution of nanopores with diameter less than 2 nm.

3.1.4 Characterizing size and density of intrinsic nanopores in CVD graphene

Previous reports have shown that defect free exfoliated graphene provides an impenetrable barrier to molecules as small as helium in gas phase[13], and likely in fluid phase as well. Instead of pursuing the arduous, and labor intensive route of making suspended areas of free-standing monolayer graphene, and then introducing sub-2 nm nanopores into that material, we decided to use graphene grown on copper using CVD. Through comprehensive imaging of CVD graphene using a scanning transmission electron microscope, previous work in our lab had demonstrated that CVD graphene has a broad, exponentially decaying distribution of nanopores ranging from sub-1 nm to 20 nm diameters. These larger defects are now believed to originate from active etching processes during the cooldown phase of CVD. There are, however, a substantial number of defects in the sub-2 nm size regime of interest for functional characterization (Figure 3.1.3).

3.1.5 Transfer of graphene to silicon nitride support membranes

Chemical vapor deposition (CVD) grown single layer graphene was purchased from ACS Materials. Graphene was transferred to 50 nm thick silicon nitride membranes using a wet transfer with polycarbonate as a support layer[23].

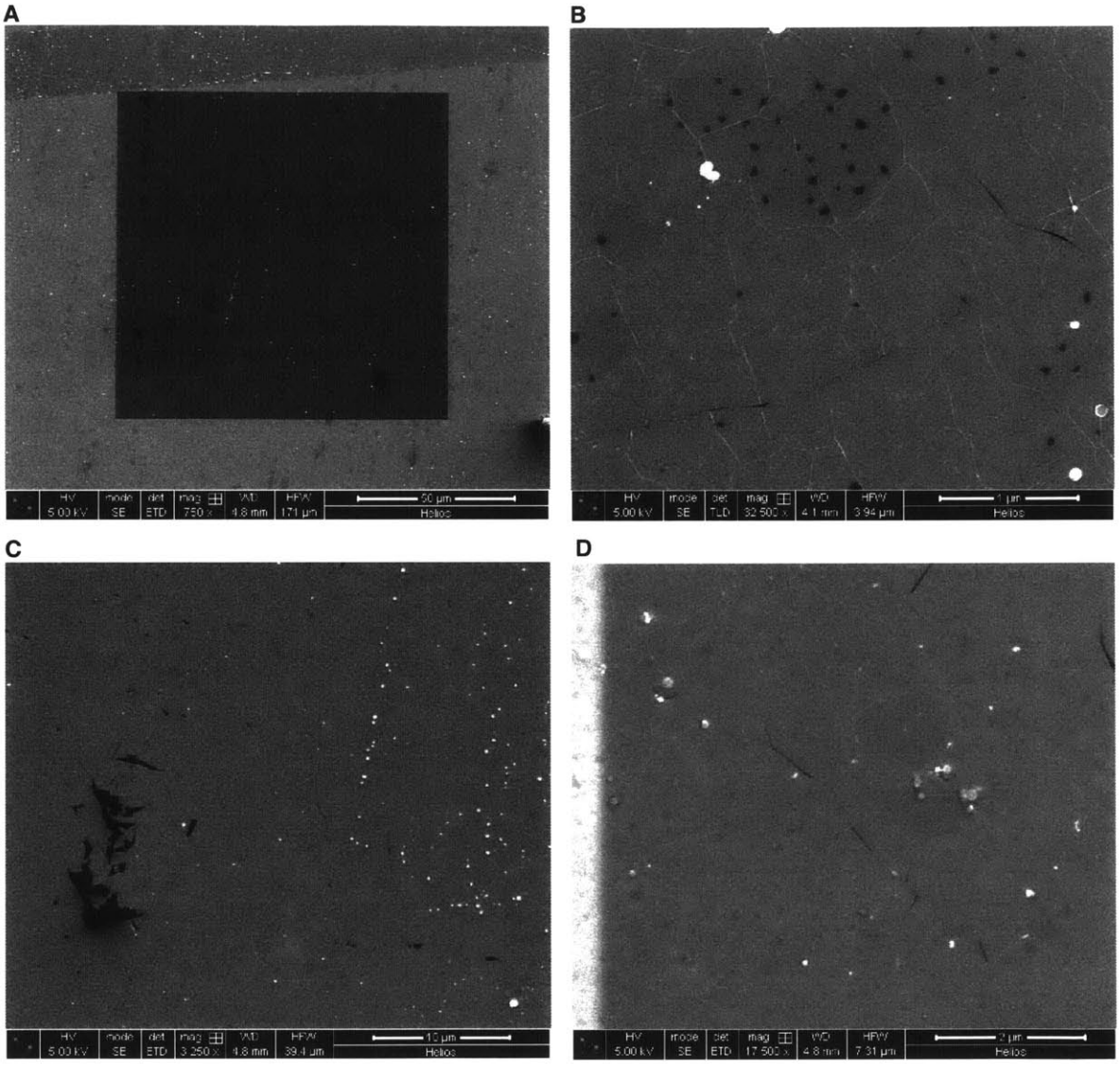

Figure 3.1.4: Scanning electron microscopy characterization of graphene coverage on silicon nitride membranes at 5kV and 86pA beam current. (A) Graphene transferred directly to a silicon nitride membrane with high coverage. Scale bar $50\mu m$. (B) Wrinkles in the graphene appear as bright, thin lines. These wrinkles possibly originate from copper grains, topography in the copper, or surface tension effects during water drainage. Scale bar $1\mu m$. (C) Thin dark lines indicate cracks in graphene coverage. Contrast between areas where graphene is present and absent arises from the difference in electron scattering at the graphene surface versus the silicon nitride surface. Scale bar $2\mu m$. (D) A void in graphene coverage can be seen as a dark spot on the silicon nitride membrane. Scale bar $10\mu m$.

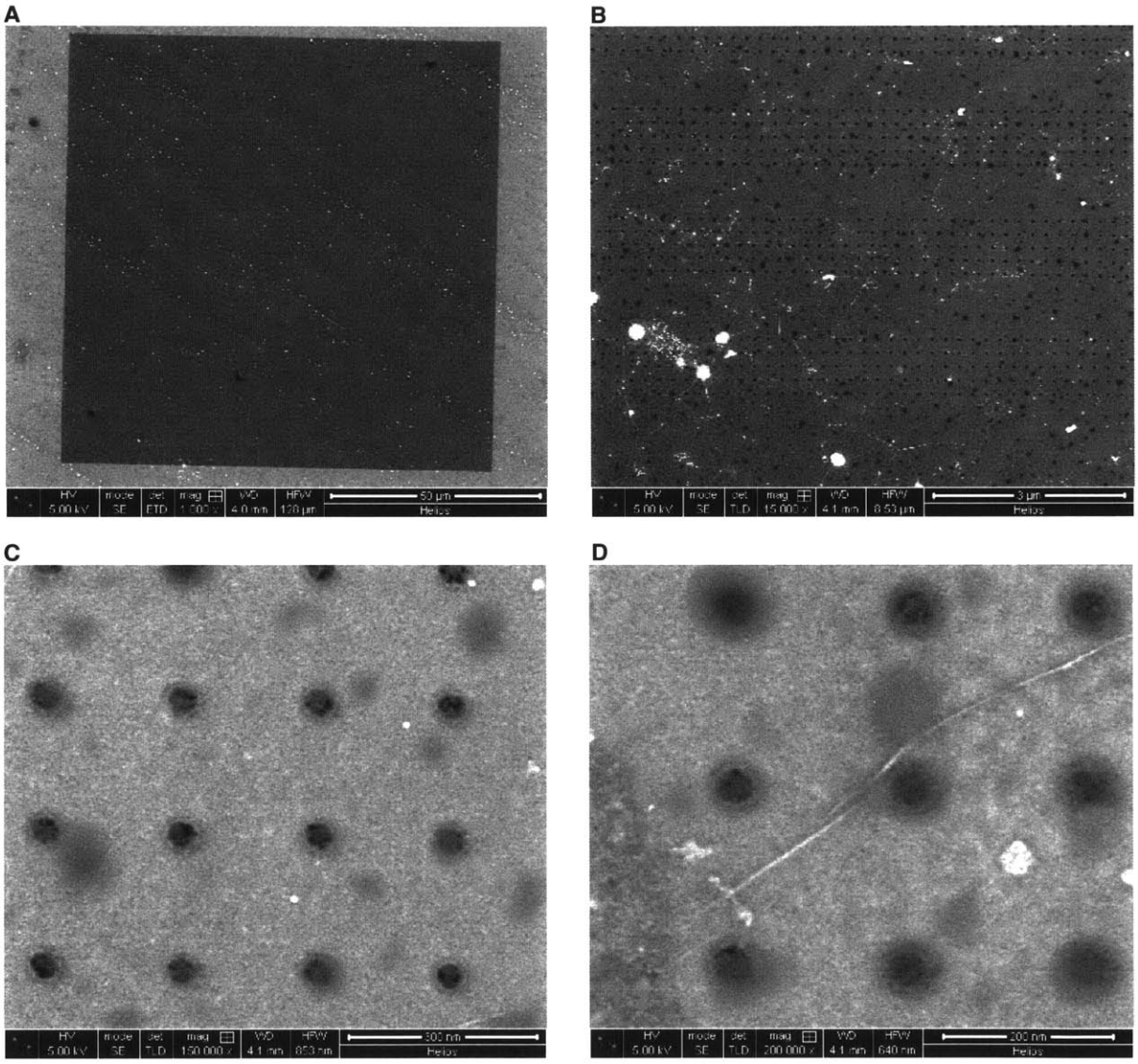

Figure 3.1.5: Scanning electron microscopy characterization of graphene over an array of nanopores in silicon nitride membranes, imaged at 5kV and 86pA beam current. (A) Graphene transferred directly to a silicon nitride membrane with high coverage. Scale bar $50\mu m$. (B) Image of the entire array of silicon nitride nanopores with suspended graphene. Scale bar $3\mu m$. (C) Closeup of 12 silicon nitride nanopores with suspended graphene. Scale bar $300nm$. (D) Closeup of silicon nitride nanopores with suspended graphene. Scale bar $200nm$.

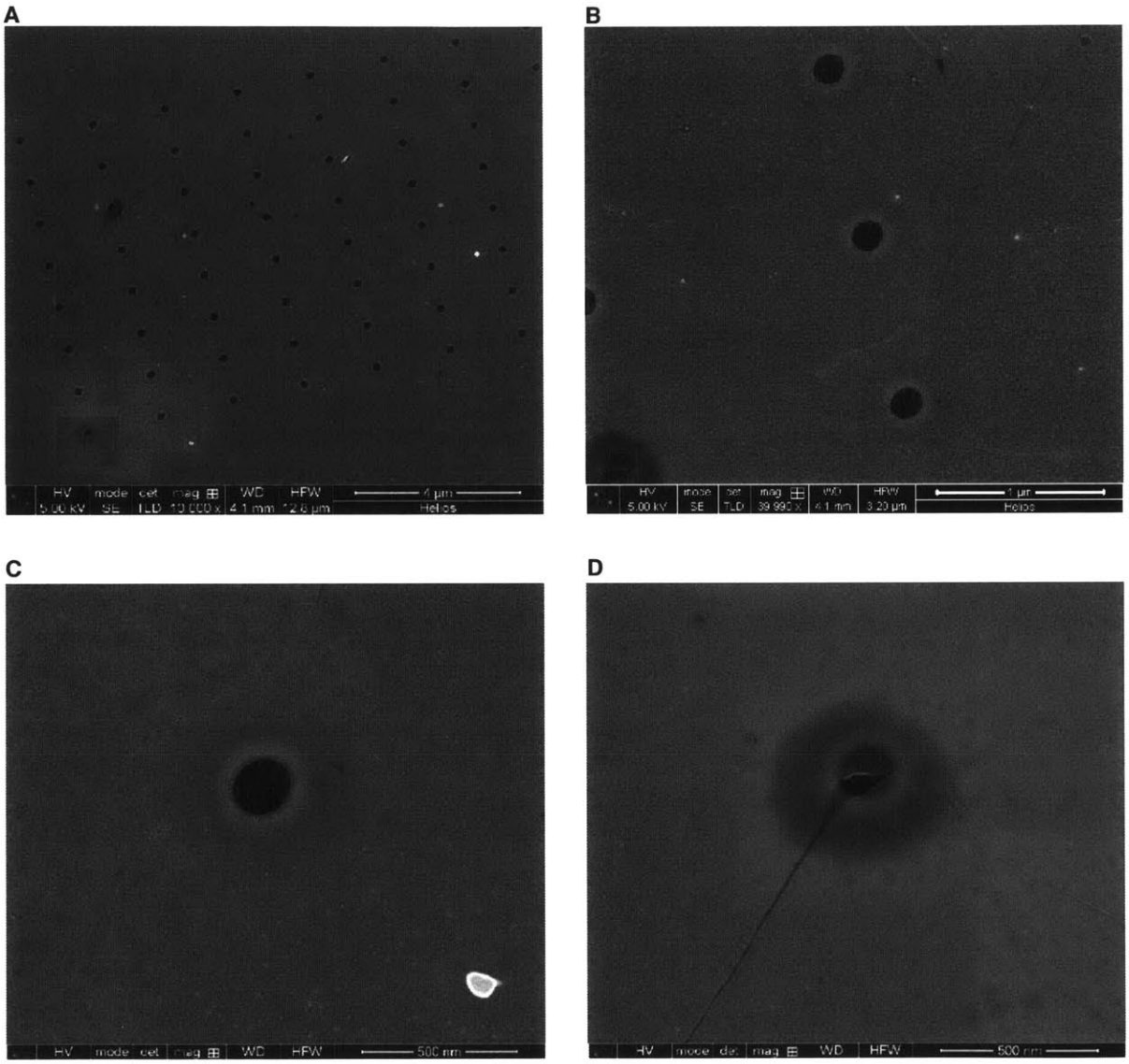

Figure 3.1.6: Scanning electron microscopy characterization of graphene over an array of nanopores in silicon nitride membranes, imaged at 5kV and 86pA beam current. (A) Array of silicon nitride nanopores with suspended graphene. Scale bar $4\mu m$. (B) Closeup of three silicon nitride nanopores with suspended graphene. Scale bar $1\mu m$. (C) Closeup of a single area with suspended graphene. Faint white lines on the area are suggestive of small amounts of residual polycarbonate on the surface. Scale bar $500nm$. (D) Closeup of a single silicon nitride nanopore with a broken graphene membrane. A crack in the graphene leading up to the big tear over the nanopore is clearly visible, and suggests that any overlap of cracks or wrinkles may cause complete short-circuiting of the ionic conductance. Scale bar $500nm$.

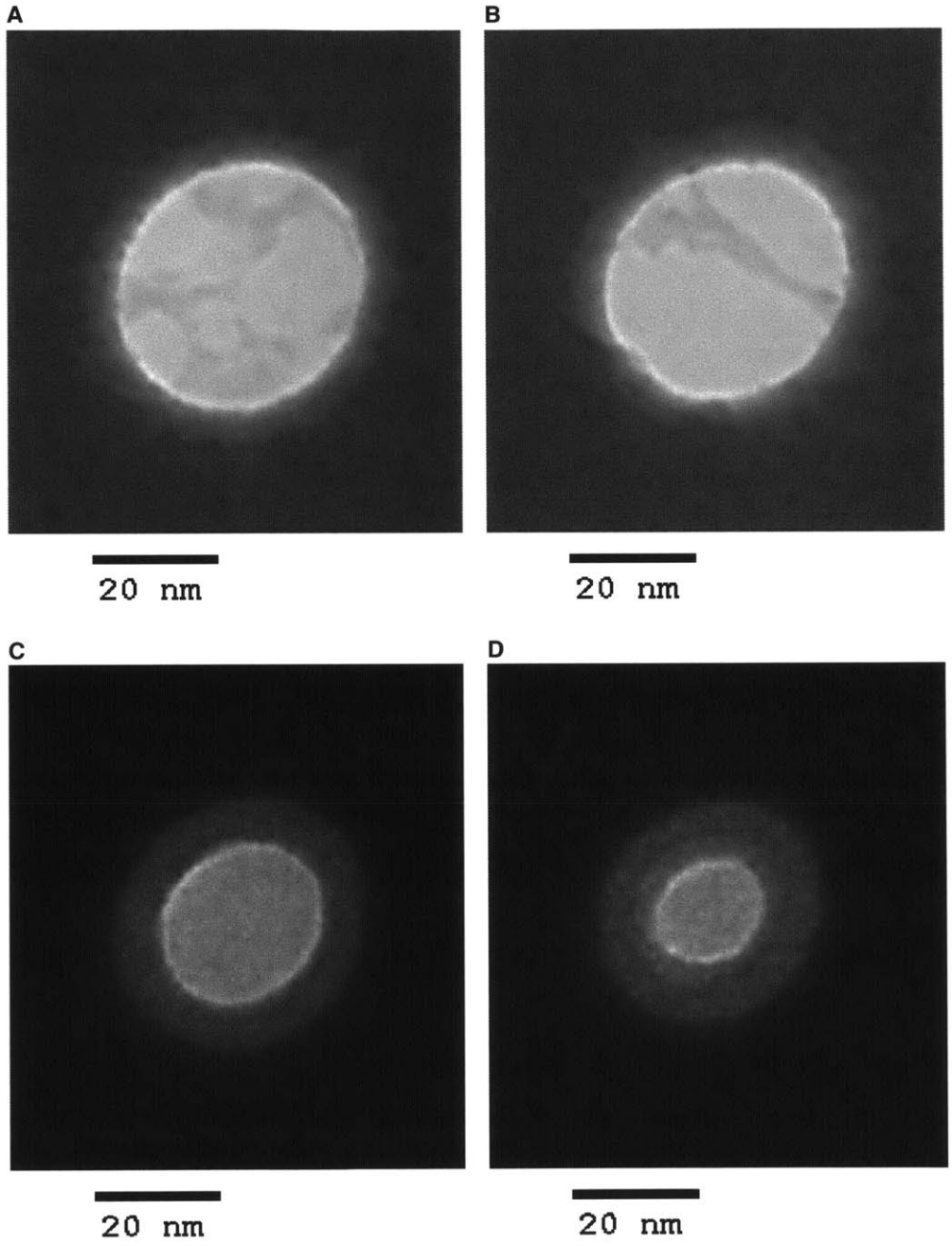

Figure 3.1.7: Transmission electron microscopy characterization of graphene over nanopores in silicon nitride membranes, imaged at 100kV for silicon nitride diameters ranging from 40nm down to 20nm diameter. Although TEM images suggest indications of residual polycarbonate, the majority of the graphene area is exposed for ionic conduction if a small nanopore in the graphene is present.

A piece of copper with graphene (Cu–Gr) was cut to a size of 8 mm × 8 mm with a razor blade and taped (Scotch® tape) along the edges of the copper onto the center of a 1 in × 3 in glass slide. A bead of polycarbonate (Sigma Aldrich, CAS#25037-45-0) was dissolved in chloroform (Sigma Aldrich, CAS#67-66-3), resulting in a 1.5% w/w solution. The (Cu–Gr) was loaded onto a spin coater and a 20 μL volume of the polycarbonate solution was spin coated at a spin speed of 2200 rpm for 30 seconds. Residual chloroform was allowed to evaporate for at least three hours, resulting polycarbonate – graphene – copper (Cu–Gr–PC) stack.

Next, a smaller piece of (Cu–Gr–PC), typically close to 6 mm × 6 mm was cut free of the glass slide. The (Cu–Gr–PC) was flipped over and exposed to oxygen plasma (Harrick Plasma PDC-32G, 7.16 W plasma at pressure of 700 mTorr with atmospheric composition) for 30 seconds to remove any graphene on the backside. The (Cu–Gr–PC) was then placed on the surface of a copper etchant bath (APS-100, http://www.transcene.com) with the exposed copper facing downwards. For the duration of the etch, the copper etchant bath was loaded into a metal pressure vessel and pressurized to two atmospheres in order to minimize bubble formation from the etching process. After one hour, the bath was unloaded, and full etching of the copper was visually verified. Next, the (Gr–PC) was scooped up and placed into a series of four to five deionized water baths to remove any copper etchant. The (Gr–PC) was allowed to sit for 20 minutes in each deionized water bath.

The patterned SiNx membrane was treated with oxygen plasma for 15 s at (7.16 W plasma at pressure of 700 mTorr with atmospheric composition). The washed graphene floating on a DI water bath was then scooped up onto the SiNx membrane. The resulting (SiNx–Gr–PC) complex was placed on a glass slide. Residual water between the nitride and the graphene was allowed to evaporate for 24 h prior to further processing. As the final step of the transfer process, the polycarbonate support on the graphene was dissolved with chloroform. The (SiNx–Gr–PC) was placed into a chloroform bath. Using an autopipette, chloroform in the bath was withdrawn and replaced with fresh chloroform. After all of the chloroform volume in the bath was replaced four times to fully remove residual polycarbonate, the chloroform was allowed to evaporate, leaving the silicon nitride with the transferred graphene membrane.

The as transferred graphene as characterized using both SEM and TEM (Figures 3.1.3 to 3.1.6).

3.1.6 Atomic layer deposition on graphene

To obtain a second estimate of the defect density, we investigated the use of atomic layer deposition to visualize defect sites. Briefly, 38 cycles of HfO_2 (at 250C) was deposited onto graphene suspended over silicon nitride support hole arrays for two different samples. Previous studies have indicated that ALD films

are unable to nucleate on graphene without pre-treatment (citation) and that defects in similar graphitic structures such as carbon nanotubes are able to nucleate defects.

In one experiment, graphene was irradiated with an gallium ion beam prior to ALD. Bombardment of graphene is expected to produce vacancy defects in the graphene, and therefore seed nucleation sites for ALD growth on graphene. The results ((Figure 3.1.8) indicate that bombardment does indeed nucleate sites for ALD growth

We found that ALD exhibited a preference to grow on graphene when a substrate is present underneath the graphene (Figure 3.1.9). The patterns of ALD growth exhibit some similarities to the morphologies of residual polycarbonate on the graphene as imaged in some free standing layers with a TEM (Figure 3.1.7). By bombarding free-standing areas of graphene with Ga^+ ions prior to ALD deposition, we found vacancy defects do provide nucleation sites for ALD growth with a density of the final ALD films that was equivalent to graphene supported by silicon nitride (3.1.10). These results therefore provide some supporting evidence that the free-standing graphene areas have defect densities low enough to perform statistical isolation of intrinsic vacancy defects in CVD graphene. However, we also found that the density of ALD films grown on graphene were not always repeatable. As it is not possible to differentiate ALD growth from surface contamination from ALD growth due to defects in the lattice even on free-standing graphene, this technique was not pursued further as a method to calculate the actual vacancy defect density.

3.2 Experimental setup for measuring current-voltage curves

The support structure containing the graphene was next mouned into a custom designed flow cell. The flow cell was configured to allow for liquid phase fluids to be rinsed across either side of the support structure, and for ionic currents to be measured across the graphene interface. The design for the flow cell is illustrated in Figure 3.2.1. The flow cell consisted of two cylindrical Teflon blocks clamped together by six polypropylene screws along the circumference of each block. In the center of the interior surface of each Teflon block, a 4 mm recess was milled for the TEM grid/gasket composite. The thickness of the TEM grid/gasket composite is larger than the sum of both recess depths in the Teflon surfaces to ensure that the gaskets compress to form a fluidic seal around the TEM grid. The exterior surfaces of the the teflon surface each had two drilled

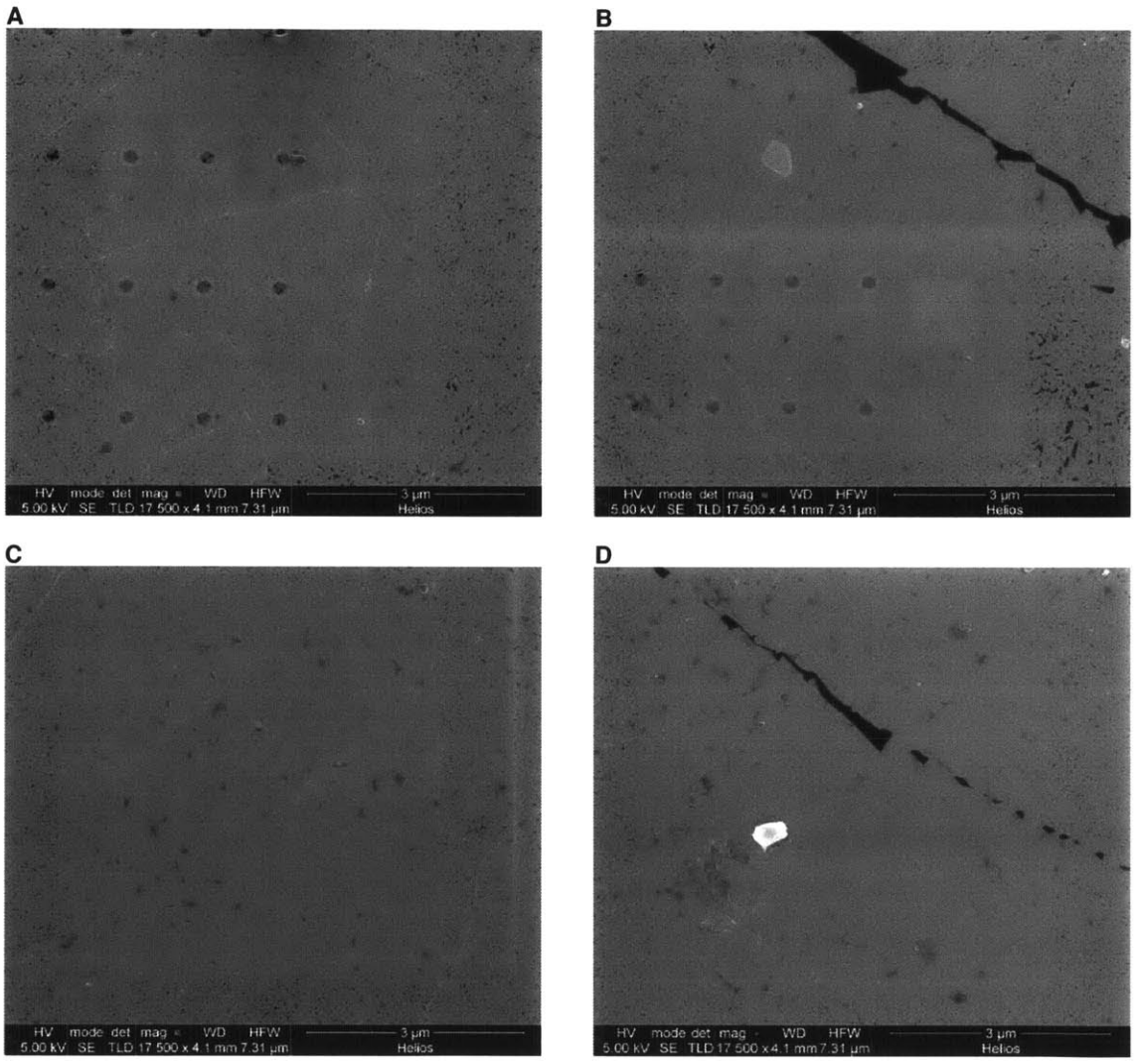

Figure 3.1.8: Atomic layer deposition of HfO_2 on graphene after imaging a graphene area with a Gallium ion beam. An ion beam scan with dwell time of (A) $50ns$ (B) $100ns$ (C) $300ns$ (D) $1\mu s$. As the scan dwell time increases, the density of ALD on the graphene increases, and saturates at full coverage of ALD on graphene. Tears in the graphene are still visible even at full ALD coverage, indicating that the graphene is still present, and that ALD growth on graphene is being visualized.

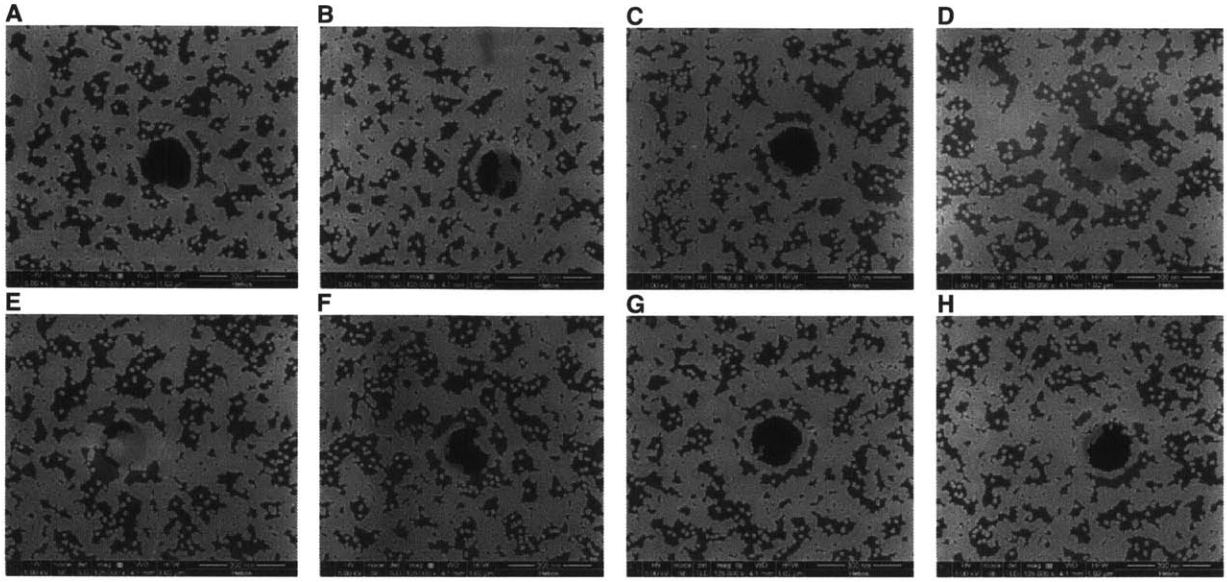

Figure 3.1.9: Atomic layer deposition of HfO_2 on free standing graphene supported by a silicon nitride membrane

from the exterior face of each Teflon block to the recess to provide a fluidic connection between the external reservoirs and the large fluidic channels in the gaskets. The fluidic channels in the silicone gaskets are cut out directly with a razor blade, and have a length of roughly 2.5 mm, and a width between 500 μm and 1 mm. To isolate only one of the nine silicon nitride membranes for measurement, and to reduce capacitive noise, a third gasket is used; this third gasket has a single hole, approximately $70 - 100\,\mu m$ in its center, and is aligned over the center SiN_x membrane of the TEM grid that contains the SiN_x nanopore and the free standing graphene. On its other side, the thicker gaskets with fluidic channels is placed.

3.2.1 Flow cell design considerations

The geometry of the flow cell described above was chosen after consideration of the following:

1. Perform a single rinsing operation (exchange one solution in contact with the nitride membrane with another) in a reasonable amount of time (3-5 minutes)
2. Ability to rinse flow cell with high efficiency ($>$ 99% replacement of old fluid after a maximum of three rinses)
3. Minimize dead volumes and its impacts on concentrations after rinsing
4. Resistance to acids and oxidizing agents

The chemical resistance criterion was automatically satisfied with the use of teflon as the flow cell material. To satisfy the remaining three criteria, however, the flow cell geometry needed to be used in conjunction with

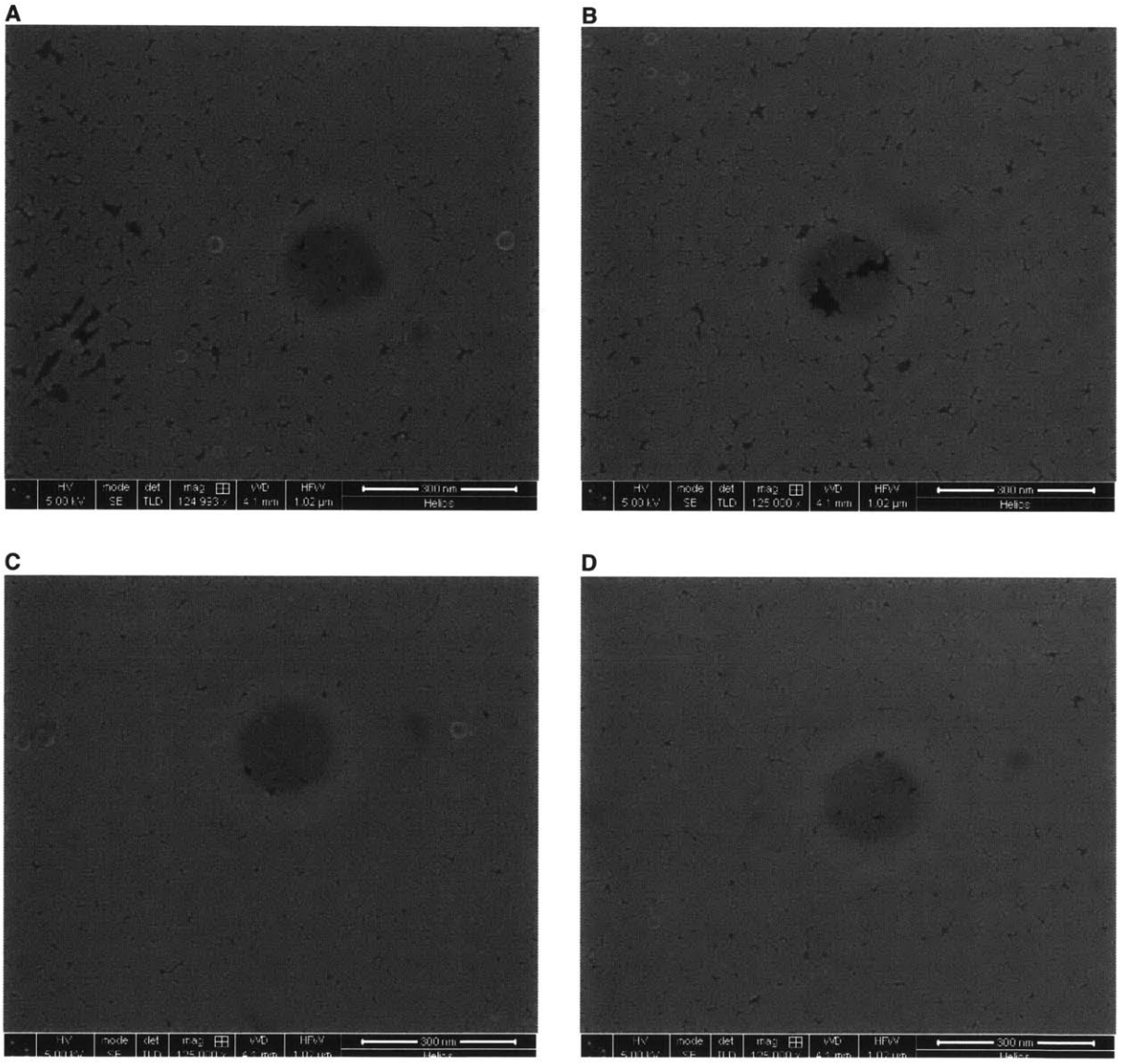

Figure 3.1.10: Atomic layer deposition of HfO_2 on free standing graphene irratediated with Ga^+ ions supported by a silicon nitride membrane

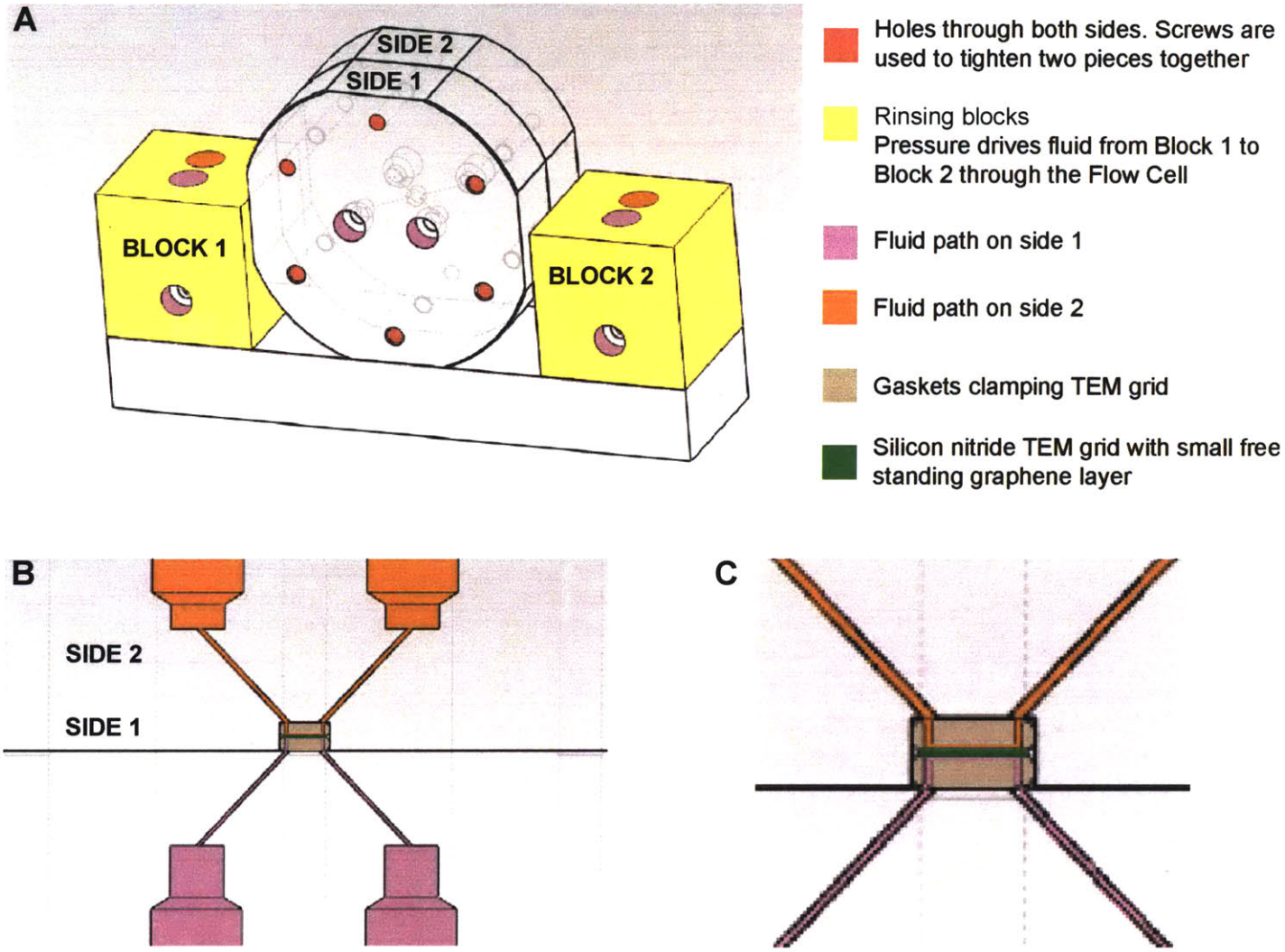

Figure 3.2.1: Schematic of custom designed flow cell. (A) Front view of the entire flow cell (excluding tubing, chromatography fittings, bolts, and nuts). (B) Cross-section of the hexagonal piece of the flow cell. All colored volumes in the image represent volumes removed by machine milling. (C) Closeup of the inner cylindrical cavity of the flow cell. The diameter of the inner cylindrical cavity is is 5mm, with the gaskets and TEM grids going inside it.

diffusion and flow rates expected in the flow cell.

The flow cell described above provides fluidic channels on either side of the silicon nitride membrane. In turn, the inlet and outlet of each of the fluidic channel is connected to two macroscale reservoirs. A pressure gradient between the two macroscale reservoirs drives the fluid in the first reservoir to the second reservoir. The reservoirs are connected to the flow cell using teflon tubing of diameter 800 μm with length of roughly $8cm$, and through interior channels of $250\mu m$ diameter with length of roughly $1.5cm$. With these dimensions, the interior channels of the flow cell provide the dominant flow resistance, and computing the flow rate Q and the passing time $\bar{t}_P$ are given by the equation for Hagen-Poiseuille flow using pressure gradient of $5\,cm\,H_2O$, or 500 Pa:

$$Q = \frac{\Delta P}{128\mu L}\pi d^4 \approx 3 \times 10^{-9} m^3/s \tag{3.2.1}$$

$$\bar{t} = \frac{V_{reservoir}}{Q} \times \frac{4L}{\pi d^2} \approx 5.2\,min \tag{3.2.2}$$

In practice, the largest dead volumes are at the bottom of the reservoirs (on the order of $50 - 100\,\mu L$, compared to the reservoir volume of $V_{reservoir} \approx 1\,mL$ and not in the flow cell. The reservoir is twice, and then the entire reservoir volume is rinsed through the flow cell in time $\bar{t}_{exp} \approx 4\,min$. This rinsing process is repeated three times to ensure good rinsing. Conductance measurements were used to verify the degree of rinsing.

3.2.2 Protocol for filling and rinsing graphene membranes in the flow cell

In order to measure ionic currents across the small graphene area, the as-prepared graphene samples were mounted into a custom flow cell that allows for solutions to be rinsed across both sides of the membrane, as described previously by Jain et al (32). To begin with, a set of five solutions ({1} Ethanol, {2} 80% Ethanol / 20% Water {3} 50% Ethanol / 50% Water {4} 20% Ethanol / 80% Water, and {5} Water) was degassed. Ethanol was used as the first solvent for ensuring that the graphene surface and the silicon nitride nanopore were all properly wetted. Each solution was rinsed across either side of the membrane, starting with the first solution, (ethanol), and ending with the last solution, (water). The sample was deemed ready for measurement once deionized water was rinsed across both sides of the membrane.

When introducing a new solution on either side of the membrane, it was critical to make sure that the old solution is completely rinsed out, and that the local concentration of the solution in contact with the membrane was indeed equal to the concentration of the new solution. After the old solution was removed

from both fluid reservoirs, the new solution was rinsed through the flow cell. The volume of the new solution that was rinsed through was three times the reservoir volume (~0.5 mL × 3 = 1.5 mL), and significantly larger than the interior fluid volume in the flow cell (at < 5 μL). Separate conductance measurements were performed after successive rinses to verify that the protocol reproducibly rinsed both sides of the membrane.

In a fair number of instances, the flow cell needs to be debugged before a sample can be measured. In some cases, a leak between the faces of the flow cell was detected, in which case the flow cell is rinsed with ethanol before taking the flow cell apart and putting it back together. This leak does not develop during testing, and is typically a result of improper bolting of the flow cell, for example if the bolts are not tightened enough, not tightened evenly, or if the threads on the teflon screws or bolts have become too worn. I

Filling the flow cell with ethanol typically occurs spontaneously, but in some rare instances, it either occurs very slowly or not at all. In these instances, the likelihood is that the fluid path has some obstruction in it - typically this obstruction is the improper alignment of the gasket channels with the 45 degree holes connecting the interior cylindrical cavity with the chromatography fittings. Usually, the solution is to take the flow cell apart and re-position the gaskets. Once, though only once, some particulate matter had lodged itself in the small 45 degree hole and had prevented any fluid flow across the flow cell.

If the flow cell does not have a leak and is filling normally, the next step is typically electrical characterization. During electrical characterization, it may be possible that a large bubble is observed on the membrane. Whether the membrane is wet or not can in fact be deduced from the power spectral density. Recall that the membranes being used are 100 μm squares, and the gasket contains in it a ~ 60 μm hole in it. The large exposed membrane area, results in a large capacitive noise at bandwidths higher than 5 kHz[57]. While this noise prevents measurement at higher bandwidths, it is also a very good indicator that the membrane has been wet with an electrolyte solution. The noise at a bandwidth of 100 kHz should be greater than 25 pA rms, and is typically larger than this.

3.2.3 Measuring current-voltage (I-V) characteristics

To measure current – voltage (I-V) characteristics, we used a patch-clamp amplifier (Axopatch 200B) with silver/silver chloride electrodes (E255, http://www.invivometric.com) to transduce the ionic current into an electronic current. The patch-clamp amplifier was operated in voltage-clamp mode, which allows for a fixed voltage to be applied across the graphene membrane while recording currents. Voltage control and digitization of analog signals (Digidata 1440A) are both programmed using free automation software, AutoIT. Current traces are typically 10 seconds long; the long duration of the current traces allows for resolving lower frequencies in the power spectral densities (PSD). All current measurements were filtered with a 5 kHz 8-pole

Bessel filter, and sampled at 25 kHz.

In the I-V curves, the current was first recorded in the absence of an applied bias. Then, the voltage is stepped down to the maximal value of the negative voltage (–200 mV). To ensure that all measurements taken are in steady state conditions, the program waits 120 s before recording the current at this voltage. The two-minute delay was longer than both the RC time constant of the amplifier, nanopore membrane, and any relaxation electrokinetic timescales. The voltage was then stepped up in pre-specified increments (10 mV) up to the maximum voltage (200 mV). Corresponding to the smaller step size for subsequent voltage steps, the delay time prior to measurement was smaller (60 s). Real time traces with no applied voltage were measured before and after the I-V curve in order to determine, and subtract, any drift in the baseline during the course of the measurements.

For samples 1 and 2, the voltage step was 20 mV, and the measurement duration was 5 seconds. For data in Figures 3B – 3D, the current traces were 60 seconds long, the voltage was swept from –800 mV to 800 mV, and the wait times were 240 s for the first and last voltage steps to/from 0 mV, and 120 s between the remaining voltage changes.

3.2.4 Data acquisition and visualization

Visualiziation of the current-voltage curves was performed on the same day as the data was acquired, and in many cases, current-voltage curves were plotted immediately after acquisition. The Auto-IT script acquires current-voltage data by sending button press inputs to the Axoscope software to change the voltage and record data files at appropriately timed intervals. The Auto-IT script immediately writes into a datalog file all of the particulars surrounding the acquisition of that datafile, including the Project, Sample number, Date, Time, Salts and their concentrations, the Voltage, the File number the data is contained in, the Duration of the recording, the Bandwidth and the Sampling rate. MATLAB programs were written to take in the starting file number and ending file number for a current-voltage curve, and automatically plot a current-voltage curve by accessing all intermediate files. The voltage steps were inferred from the number of data files in the current-voltage curve, as the maximum voltage was always 200mV and the steps uniformly spaced. Early on, a GUI was written in MATLAB that automatically detected all current-voltage curves in a datalog that the user read in. However this approach requires further work, but was impeded by MATLAB's inability to handle the large database that was generated. Such an interface also makes data analysis much more difficult, as the actual data vectors are less accessible than if they are read in by the operator. Visualization of the data on the same day is extremely important, however, as it can be used to confirm what the flow cell should be tested with on the following day.

3.2.5 Control experiments to determine conductance limits of the setup

We performed a number of negative and positive control experiments to verify that the measured current was passing through a nanopore in the graphene membrane. The results demonstrated that our flow cell can resolve any conductances higher than 10 pS. Transport between silicon nitride and graphene has not been reported in any of six papers on larger (> 2 nm) graphene nanopores. As it is not possible to reliably fabricate a graphene device with explicit knowledge that there are no nanopores available for direct transmembrane conductance, direct measurement of transport between the graphene and silicon nitride has remained a major challenge. In this section, we do not directly measure the interlayer transport conductance between graphene and SiNx. However, we devise control experiments that provide an upper bound for the interlayer conductance as described below. The different control experiments, detailed in text, are also summarized by Figure 3.2.2:

1. Current around and through nitride membrane without support hole.
   (a) Sample: No support hole, no graphene, no ALD
   (b) Measured a conductance of < 10 pS
   (c) This measurement means that samples with conductances lower than 10 pS cannot be resolved by the measurement setup.
2. Limiting conductance of support hole
   (a) Sample: Support hole, no graphene, no ALD
   (b) Measured conductances between 270 nS and 350 nS
   (c) Conductance measurements below 50 nS can safely neglect resistance modulations from the silicon nitride support hole.
3. Current through graphene with ALD
   (a) Sample: Support hole, graphene, ALD (38 cycles, ~5 nm thickness HfO2)
   (b) Measured conductances of 139 pS and 96 pS
   (c) ALD is expected to grow on defects in graphene, and along grain boundaries, thereby reducing their conductance. These experiments show that ALD is likely to significantly reduce the measured conductance.
4. Current between graphene and silicon nitride through support hole

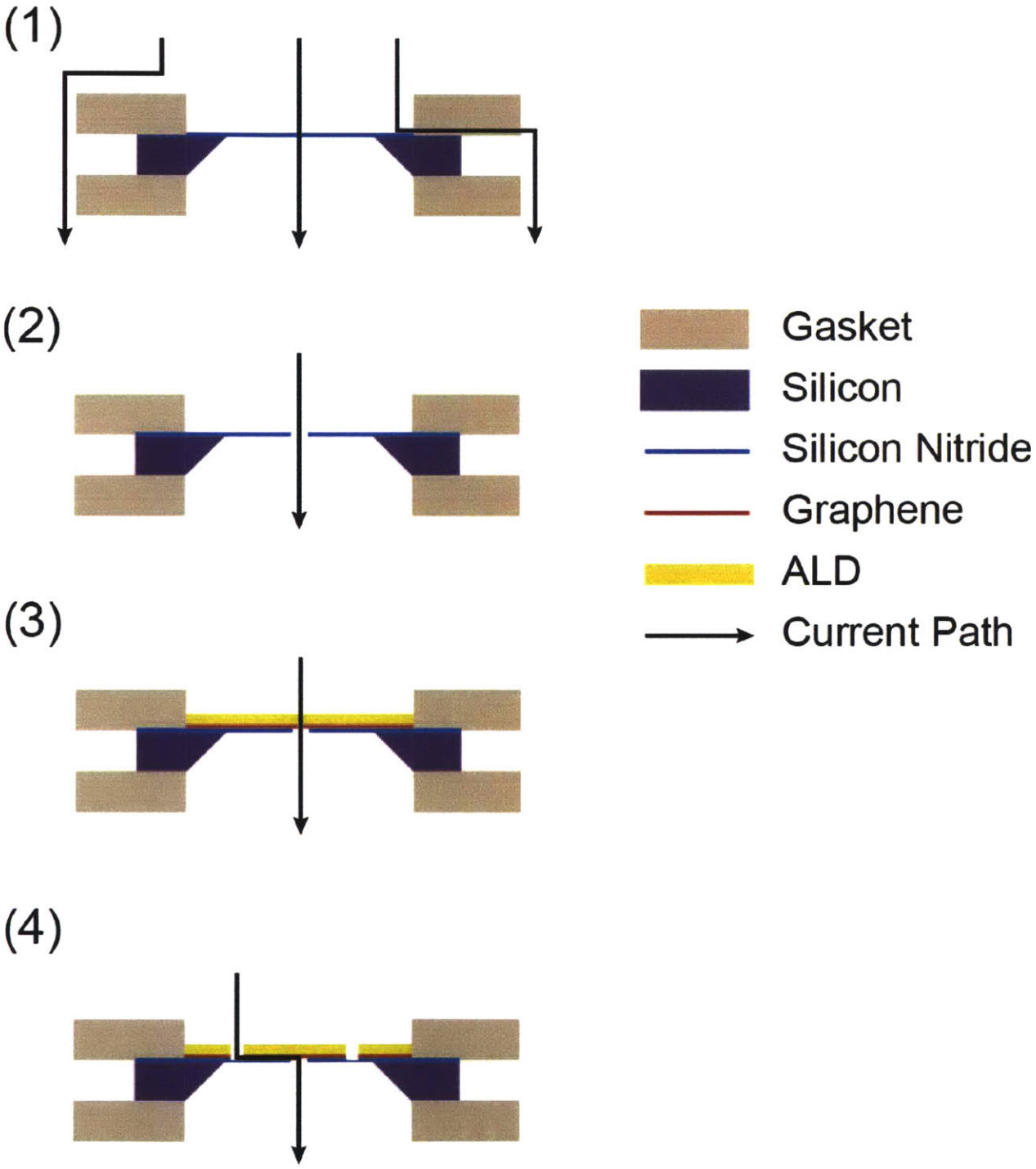

Figure 3.2.2: Illustration of four different control experiments. (a) (b) (c) (d)

(a) Sample: Support hole, graphene, ALD, and 15 μm diameter circular cut centered around the support hole.

(b) Measured conductances of 73 pS and 56 pS.

(c) The circular cut centered around the support hole creates a pre-defined circumference through which interlayer transport can occur. The conductances in this experiment are similar, but slightly lower than in

(d) This suggests that there is a very low probability that the ionic solution wets the interface between the graphene and the silicon nitride, and provides additional ion transport as a result.

(e) If the leakage current originates from transport between the graphene and the SiNx, the conductance of this pathway would be expected to scale as , where is the radius of the support hole, and is the radius of the circular cut. In a real experiment, where no ALD is performed, and assuming wrinkles along grain boundaries provide access to interlayer transport with , the factor is only a factor of 2 times larger than the control experiment. Furthermore, we expect this factor of 2 to be compensated for the fact that a tear is likely to allow for conduction on one or two of the sides of the graphene grain, whereas our control experiment exposes the graphene to ionic conduction along the entire circumference of the milled cut. Therefore, we reason that this experiment provides a decent upper bound for interlayer transport in devices without ALD.

3.2.6 Parametric descriptions of current-voltage curves

Characterizing the nonlinear relationship between the applied voltage and the ionic current can provide important insight into the physics of ionic transport across the graphene nanopore. In particular, comparing the conductance at higher voltages (where the curve is nonlinear) to the Ohmic conductance (where the curve is linear) can provide a meaningful description of the overall nonlinearity. The Ohmic conductance is defined for small voltages compared to thermal energy, $G_{Ohmic} = G\left(eV < k_BT\right)$. Experimentally, the Ohmic conductance is found by computing the slope of the IV curve for $eV < 1.6k_BT$. To describe nonlinearities, we defined a parameter:

$$NL\left(V\right) = \frac{G\left(V\right) - G_{Ohmic}}{G_{Ohmic}} \tag{3.2.3}$$

At low voltages, the current-voltage curve is linear, and therefore, the nonlinear parameter is zero, $NL\left(V < k_BT/e\right) \simeq 0$. Non-zero values of the nonlinearity, therefore must occur at higher voltages, and can produce either a positive or negative value. It is possible for I-V curves to exhibit asymmetry, $G\left(V\right) \neq G\left(-V\right)$, and an asymmetry parameter is defined as:

$$\chi(V) = 2\left|\frac{G(V) - G(-V)}{G(V) + G(-V)}\right| \tag{3.2.4}$$

To provide a single value for the nonlinearity despite potential asymmetry in the I-V curve, most nonlinear parameters reported for I-V curves will in fact be the average of the nonlinear parameter at the maximum and minimum voltages used (typically $\pm 200\, mV$). This averaged nonlinearity is defined as:

$$\bar{NL}(V) = \frac{1}{2}\left(NL(V) + NL(-V)\right) \tag{3.2.5}$$

Different combinations of this function, $NL(V)$, are used to classify nonlinear behaviors.

A rectification ratio, R_C is defined to characterize the degree of rectification. The rectification ratio is defined as:

$$R_C = \max\left(\left|\frac{G(+V)}{G(-V)}\right|, \left|\frac{G(-V)}{G(+V)}\right|\right) \; iff \; NL(+V) \times NL(-V) < 0 \tag{3.2.6}$$

According to this definition, a rectification ratio of one, $R_C = 1$ means that the curve is not rectified. Values larger than one indicate larger rectification, and values less than one are not possible. Another type of nonlinear behavior is activated current-voltage curves. In an activated I-V curve, the conductance $G(\pm V) > G_{Ohmic}$. Provided this criteria is met, the degree of activation will be numerically represented by $\bar{NL}(V)$.

3.3 Verifying sub-2 nm diameter by comparison with literature

The first experiment performed on each graphene device was to measure the conductance at 1 M KCl, with the intention of obtaining an upper bound on the diameter of the nanopore being tested. One limitation of the experimental approach taken in this thesis is that there is no direct visualization of the graphene nanopore structure being measured, either before or after measuring its functional current-voltage properties.

The method to determine the upper bound estimate of the diameter was constructed by a series of observations from literature. By plotting the relationship between diameter and conductance across a number of previous reports, both experimental ($>$ 2nm pores) and molecular dynamics (MD) on sub-2 nm pores, we found that graphene nanopore charge on a graphene nanopore consistently increases the conductance. In particular, the conductance-diameter relationship for uncharged nanopores derived from MD was summarized by an analytical model. The analytical model developed by Suk et al. is described in Equations 3.3 to 3.3.

$$G_{analytical}^{MD-approx}\left(d_P, z_P = 0\right) = \frac{\sigma_P}{\left(\frac{1}{\pi d_P} + {}^{4L}/_{\pi d_P^2}\right)} \tag{3.3.1}$$

$$\sigma_P = \sum_i \mu_i^P z_i c_i \tag{3.3.2}$$

$$c_i = c_0\left(1 - \lambda_i^2\right)\exp\left(-\Phi_{hyd}^i / k_B T\right) \tag{3.3.3}$$

$$\Phi_{hyd}^i = \frac{2}{d_P}\Phi_{hyd}^{i,0} \tag{3.3.4}$$

$$\lambda_i = \frac{d_i^*}{d_P} \tag{3.3.5}$$

The Suk et al. derives a solution for the conductivity inside the nanopore, that changes as a result of the reduced concentration and diffusivity of the ion. The paper provides some additional plots for the diffusivity and mobility of the ion under confinement, and it is those values that need to be used in the equations above. However, one incorrectly assumption is that the access resistance (resistance of ions transporting to the nanopore) is determined by the same conductivity as the nanopore itself. A closer approximation to the real physical system would be to use the bulk conductivity for ions transporting in bulk to the nanopore. Therefore, in future plots, the Suk et al. conductance model has been modified as:

$$G_{analytical}^{MD-approx} = \left(\left[\left(\pi\sigma_B d_P\right)^{-1} + \left(\frac{\pi\sigma_P d_P^2}{4L}\right)^{-1}\right]\right)^{-1} \tag{3.3.6}$$

The conductance-diameter relationship for uncharged nanopores matches experimentally observed conductances for largr ($>$ 2nm pores). At a given conductance, G^*, this formula can be used to extract an estimated nanopore diameter, $d_P^{z=0}$ by solving for the only positive root of the nonlinear equation:

$$\left(d_P^{z=0}\right)^2 - \frac{G^*}{\pi\sigma_B} d_P^{z=0} - \frac{4LG^*}{\pi\sigma_P\left(d_P^{z=0}\right)} = 0 \tag{3.3.7}$$

As the function $\sigma_P\left(d_P^{z=0}\right)$ is a monotonically decreasing function, the value of $d_P^{z=0}$ is a monotonically increasing function of the conductance, G^*. For smaller nanopores, MD simulations on charged graphene nanopores (purple and pink symbols) all report a higher conductance compared to the analytic model for

uncharged pores for the same diameter. Mathematically, this relationship is represented by:

$$G = G\left(d_P, z_P, \Lambda\right) \tag{3.3.8}$$

$$G\left(d_P, 0, \Lambda\right) < G\left(d_P, z_P, \Lambda\right) \tag{3.3.9}$$

When keeping all other external variables, Γ, constant, we have:

$$G\left(d_P, 0\right) \approx G_{analytical}^{MD-approx}\left(d_P, 0\right) < G\left(d_P, z_P\right) = G^* \tag{3.3.10}$$

Using the monotonic nature of the analytic approximation to MD simulations, there exists a diameter d_P^{UB} such that $d_P^{UB} > d_P$ satisfying the relationship:

$$G_{analytical}^{MD-approx}\left(d_P, 0\right) < G_{analytical}^{MD-approx}\left(d_P^{UB}\right) = G^* \tag{3.3.11}$$

In conclusion, compiling the literature enables derivation of an upper bound diameter for any nanopore being measured experimentally using the approximate analytical scaling of MD simulations. It is evident that this is an approximation, as there is no formal proof that molecular dynamics simulations provide an accurate computation of the ionic conductance. However, the goal of obtaining an upper bound is to verify that the nanopores being tested have diameters less than 2 nm. Usings the upper bound estimate, we find that eight of ten measured graphene devices had upper bound diamters below 2 nm. Devices were measured at 1M KCl to ensure accurate comparison to the model and literature.

Variable	Description
G	Conductance of the graphene nanopore
G^*	Experimentally measured conductance
$G_{analytical}^{MD-approx}$	Conductance from Suk et al. approximating MD simulations on uncharged pores
d_P	Diameter of the graphene nanopore
d_i^*	Diameter of a solvated ion. Likely diameter of first hydration shell
z_P	Charge of the graphene nanopore
Λ	Set of all other variables determining the conductance
σ_B	Conductivity of the bulk electrolyte
σ_P	Conductivity of the electrolyte in the nanopore
z_i	Valence of species i
c_i	Concentration of species i in the nanopore
μ_i	Mobility of species i in the nanopore
Φ_{hyd}^i	Free energy barrier for species i in the nanopore
$\Phi_{hyd}^{i,0}$	Fitted coefficient describing relationship between diameter and energy barrier
D_i	Diffusivity of species i in the nanopore

3.4 Phenomenological behaviors of sub-2 nm graphene nanopores

By measuring current-voltage curves across multiple salt solutions, we found that graphene nanopores exhibit distinct behaviors resembling those of biological ion channels. As larger graphene nanopores have not been shown to display these nonlinear behaviors, they likely originate from the spatial confinement of ions in that occurs as the diameter decreases below 2 nm. This section is organized on the basis of behavior, and covers the majority of the data taken on the sub-2 nm graphene pores.

3.4.1 Nonlinear current-voltage curves and cation selectivity

Three types of current-voltage behaviors were observed: linear (Figure 3.4.1a), rectified (Figure 3.4.1b), voltage activated (Figure 3.4.1c). Interestingly, virtually all current-voltage curves could be characterized with one of these three behaviors across all salts and concentrations in all ten devices tested. Current-voltage curves in 1M KCl (Figure 3.4.2a) and in 100mM KCl (Figure 3.4.2b) are presented for each of the ten devices.

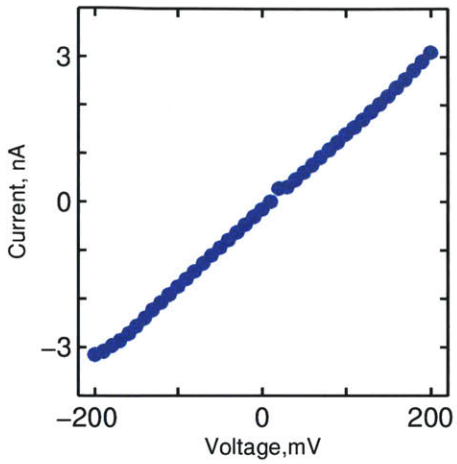

(a) Linear I-V profile, measured at 1M KCl for Device 8

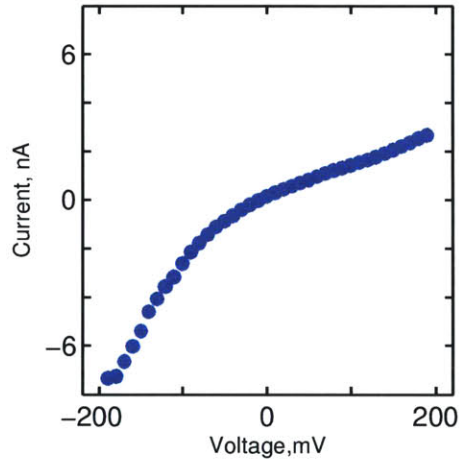

(b) Rectified I-V profile, measured at 1M KCl for Device 9

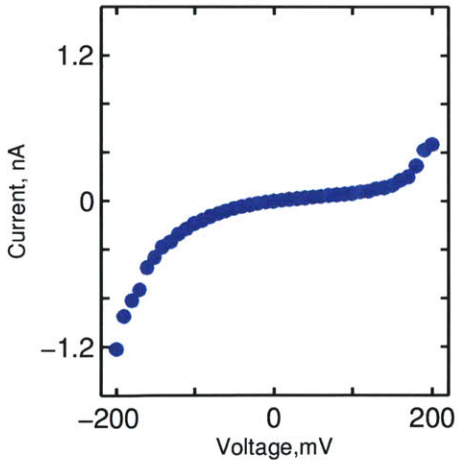

(c) Voltage activated I-V profile, measured at 1M KCl for Device 5

Figure 3.4.1: Types of current-voltage profiles.

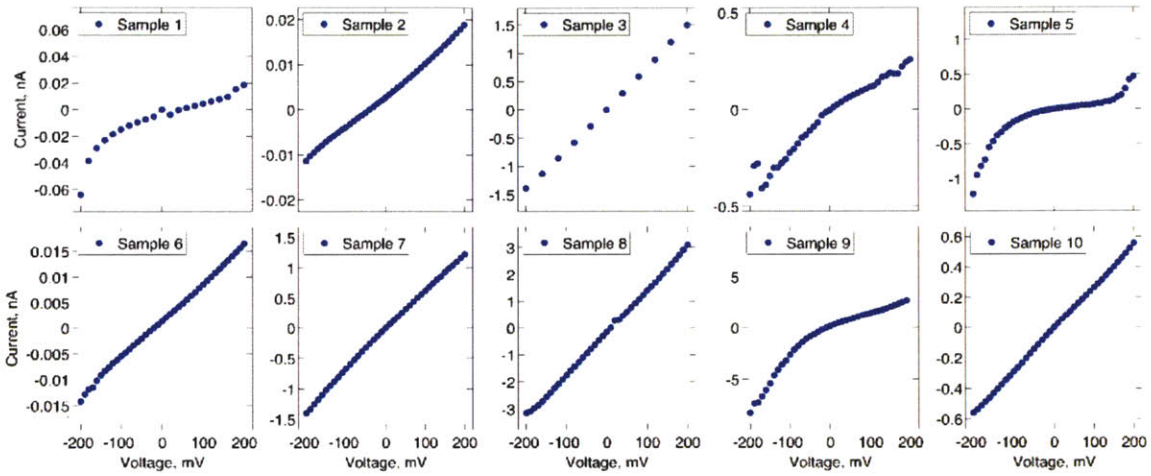

(a) Measured in 1M KCl

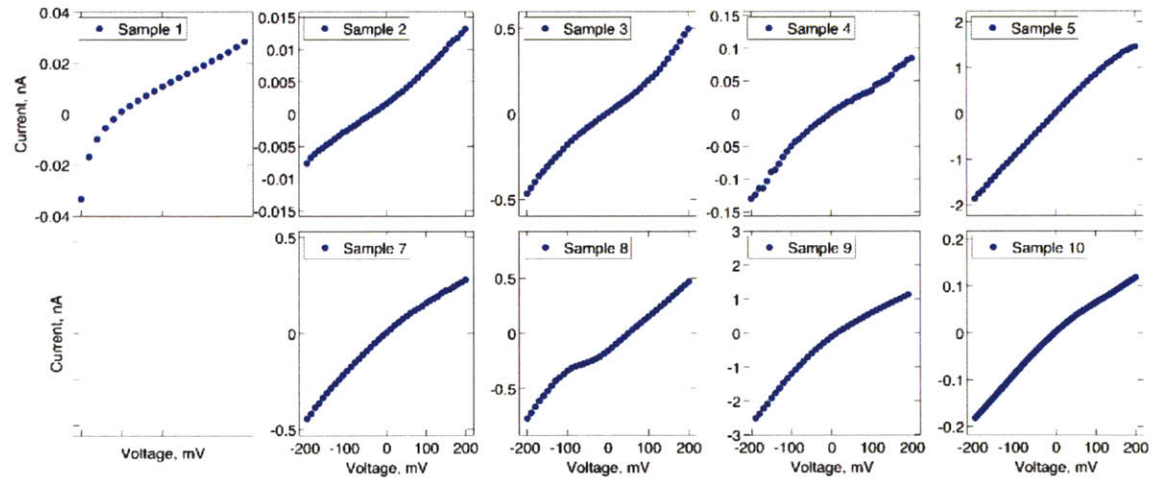

(b) Measured in 100mM KCl

Figure 3.4.2: Current-voltage (I-V) profiles for all ten devices:

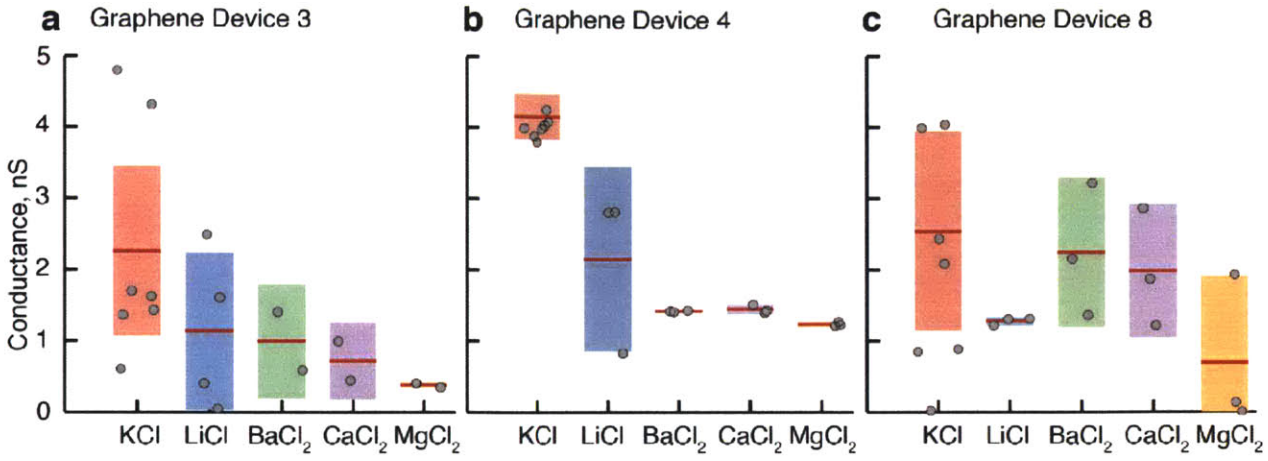

Figure 3.4.3: Conductance measurements

During measurements on six of the ten devices, the conductance increased significantly within a few hours, indicating that the graphene had delaminated from the silicon nitride substrate. The remaining four devices (devices 1, 3, 4, and 8) were tested extensively in several salts, (1) KCl, (2) $LiCl$, (3) $BaCl_2$, (4) $CaCl_2$, and (5) $MgCl_2$. We used 100 mM concentration for monovalent salts, and 50 mM concentration for divalent salts in order to ensure that (a) the chloride ion concentration was consistent across all experiments, and (b) the product, $\sum_i c_i z_i$, was the same for all cations, ensuring that to first order, differences in the conductance were arising from differences in the mobility of the ions, and not from differences in bulk conductivity.

The measured current-voltage curves are plotted in Figures 3.4.4, 3.4.5, and 3.4.6. The data clearly nonlinear behaviors that depend on the salt under test - these nonlinear behaviors will be critical in developing a theory and matching it against experiments. However, the first synthesis of the data should start with the simplest characterization of the system: the conductance. Conductance measurements from devices 3, 4, and 8 have been summarized in Figure 3.4.7. The salts on the x-axis are arranged by increasing hydration energy. We found that each of the three devices display distinct trends in ionic selectivity. The trends in ionic selectivity do not change when the conductance is normalized by the conductivity of the bulk electrolyte, indicating that physical interactions inside the nanopore are responsible for the differences in conductance.

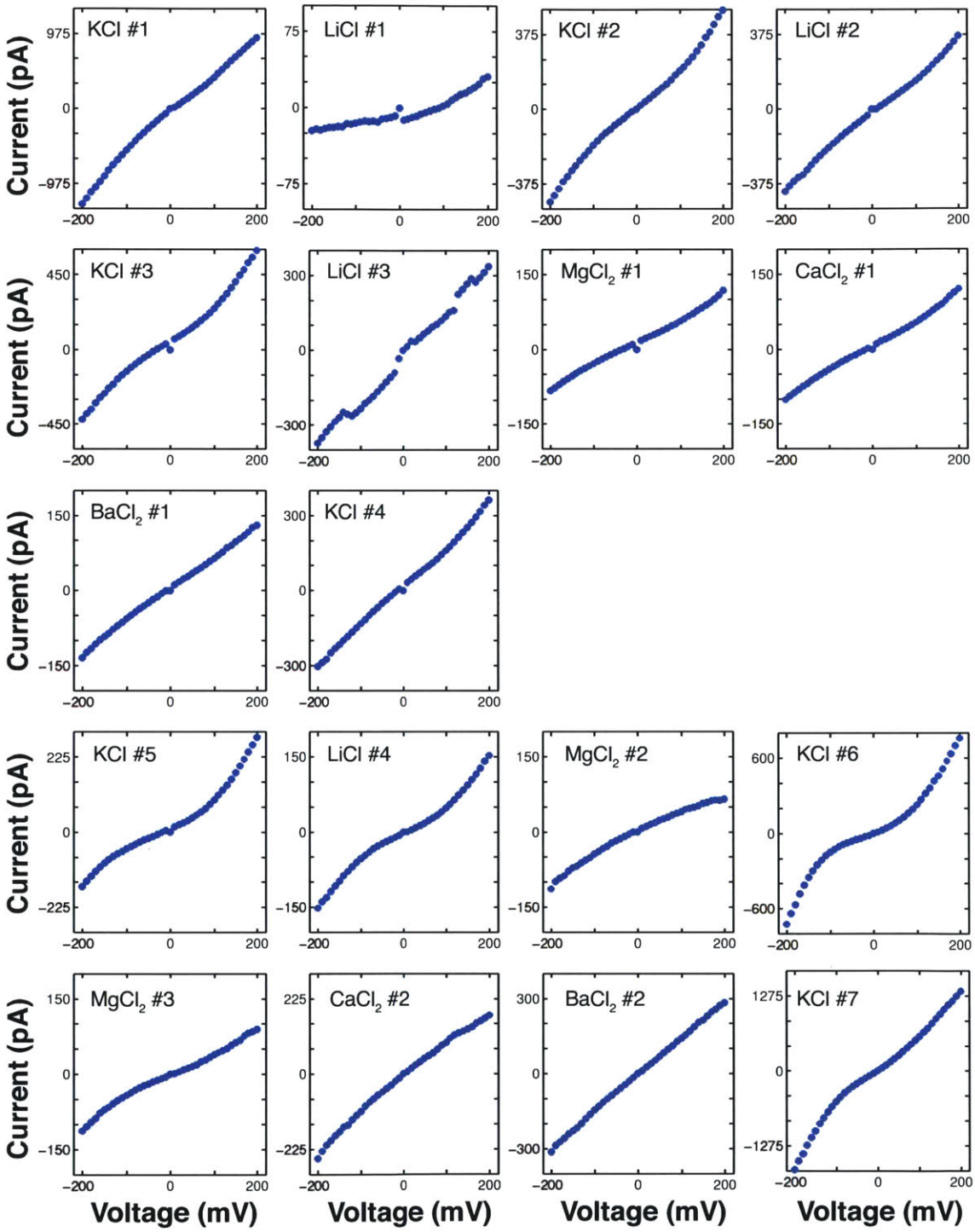

Figure 3.4.4: Current-Voltage curves for Device 3, arranged chronologically reading left to right

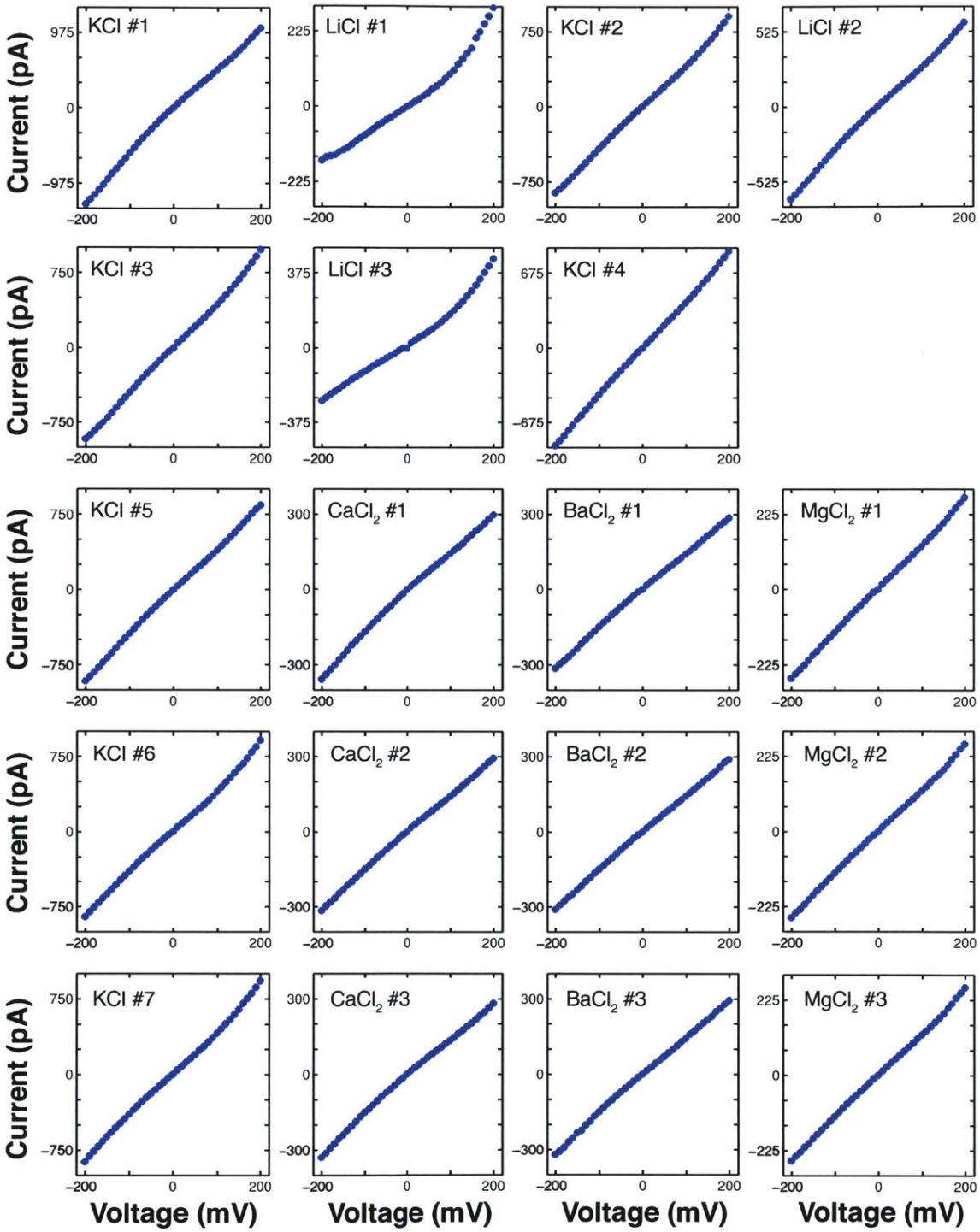

Figure 3.4.5: Current-Voltage curves for Device 4, arranged chronologically reading left to right

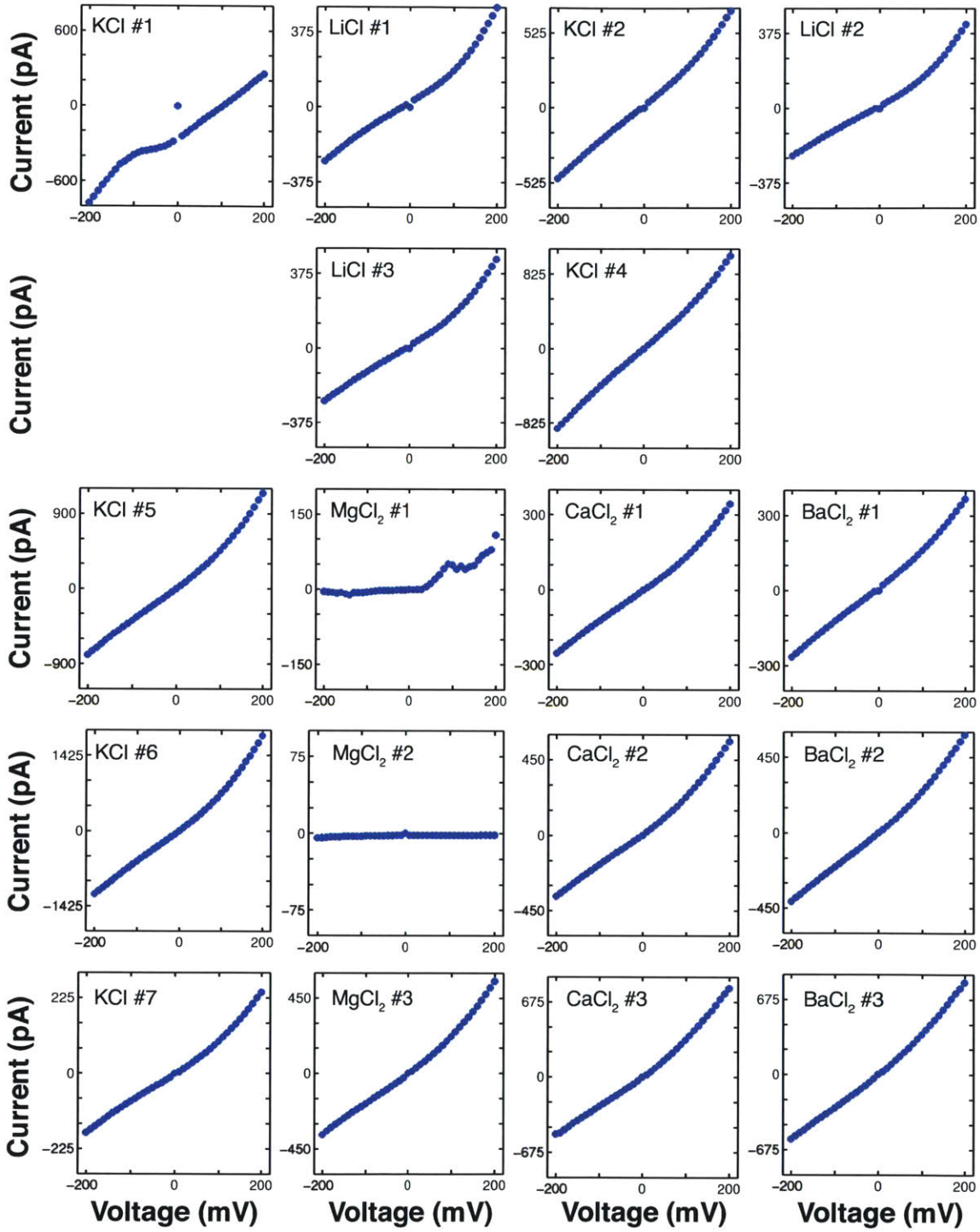

Figure 3.4.6: Current-Voltage curves for Device 8, arranged chronologically reading left to right

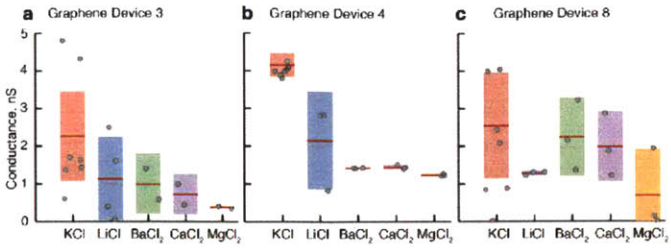

Figure 3.4.7: Conductances of five different salt solutions (KCl, LiCl, $BaCl_2$, $CaCl_2$, and $MgCl_2$ taken across three different devices. (a) Graphene Device 3. (b) Graphene Device 4. (c) Graphene Device 8. The data provides an indication for the relative transport rates between different ionic solutions, and differences in the ordering of the conductances for the ionic solutions indicates the emergence of selectivity.

The flow cell was rinsed thoroughly (using the procedure above) with each new salt solution prior to recording an I-V curve. We first measured I-V curves for KCl (1) and LiCl (2) three times, alternating between each salt, i.e. measuring (1) – (2) – (1) – (2) – (1) – (2). Then, I-V curves were measured for KCl and the divalent salts three times: [(1) – (3) – (4) – (5)] × 3 This procedure was adopted so that we could average out the conductance over three measurements for each salt, and in order to use the benchmark the conductance over time with potassium.

In the dilute concentration limit, the differences in conductance between each salt can be directly attributed to the difference in conductance betewen the cations. Neglecting the effects of correlations between ions:

$$G\left(XCl\right) \simeq G\left(Cl^{-}\right) + G\left(X^{+}\right) \tag{3.4.1}$$

$$G\left(YCl\right) \simeq G\left(Cl^{-}\right) + G\left(Y^{+}\right) \tag{3.4.2}$$

$$\implies G\left(X^{+}\right) - G\left(Y^{+}\right) = G\left(XCl\right) - G\left(YCl\right) \tag{3.4.3}$$

Therefore, the trends in ionic selectivity across each salt can be attributed specifically to differences in the transport rates of cations in solution. This cation selectivity suggests that the effects in which the finite size of the ion plays a role, such as the dehydration energy, may be playing a role in creating selectivity between cations.

	KCl	$LiCl$	$BaCl_2$	$CaCl_2$	$MgCl_2$
Device 5	1.5739	1.2967	0.5764	0.3931	0.0345
Device 6	0.4671	1.1459	0.0081	0.0593	0.0343
Device 10	2.0109	0.0615	0.9251	0.8205	1.0797

Table 3.1: Standard deviation in conductance values, nS

	KCl	$LiCl$	$BaCl_2$	$CaCl_2$	$MgCl_2$
Device 5	71.5%	106.4%	58.1%	54.0%	9.0%
Device 6	11.3%	53.7%	0.6%	4.1%	2.8%
Device 10	79.3%	4.9%	41.6%	41.7%	163%

Table 3.2: Standard deviation in conductance values as % of mean conductance

Intra-salt conductance fluctuations and temporal stability

One of the most immediate features of the data is the statistically significant change in conductance measured over multiple time points for the same salt. The statistical significance here is determined by the fact that the changes in conductance are *much* larger than the uncertainty in the conductance measurement itself. The differences are so large, in fact, that in some cases, the fluctuations resemble transitions between ON and OFF states. For example, the conductance of lithium chloride in Device 5 virtually exhibits has a lowest conductance measurement of 12.5pS, with a second lowest conductance measurement of 387pS, or a 30× increase (the largest conductance measurement of 2.88nS is 230× larger. Magnesium chloride in Device 10 exhibits similar behavior, with three conductance values that are distributed across four orders of magnitude (5.4pS, 72.8pS and 1.91nS).

These fluctuations are not well correlated with the type of salt being tested. Each salt, in at least one device, exhibited large fluctuations (Table 3.1). When tabulated as percentages of the mean, it becomes clear that the degree of fluctuations in the conductance are linked to the cation type with some non-trivial dependence.

Furthermore, intra-salt conductance fluctuations could not be correlated with time under measurement. Table 3.3 provides the conductance for 100mM KCl for multiple runs over a total of three days. Conductance data of other salts cannot be used to estimate trends in the conductance over time, as other salts only had two to three measurements aken, all of which were on the same day. The data show that there was no consistent increase or decrease over the course of measurement, and that changes in conductance are likely ocurring due to changes in the nanopore state. Finally, the large range over which the conductance varies, and the sensitivity to the salt under test, indicate that the transmembrane potentials are extremely sensitive to perturbation and are specific to ion type. Both these conclusions will be discussed with a more mathematical basis as we move onto modeling of the data in Chapter 4.

	Run 1	Run 2	Run 3	Run 4	Run 5	Run 6	Run 7	Run 8
Device 5	4.12	1.68	1.55	1.34	0.59	1.36	4.68	
Device 6	5.25	3.95	4.23	4.02	4.07	3.78	3.87	3.96
Device 10	2.14	2.41	0.02	4.03	3.95	5.99	0.84	0.88

Table 3.3: Conductance values for KCl at 100mM in each of the three devices

	Run 1	Run 2	Run 3	Run 4	Run 5	Run 6	Run 7
KCl	WA	A	A	WA	SA	SA	A
$LiCl$	?	WA	L		A		
$MgCl_2$			A		R	A	
$CaCl_2$			A			R	
$BaCl_2$			L			L	

Table 3.4: Device 5: Progression of nonlinearity over all salts during testing

Trends in nonlinear behavior across salts

The recorded current-voltage curves measured for each salt were examined to determine whether there were any consistent trends indicating that the nonlinearity depended on the type of salt, and whether there was any temporal correlations between nonlinear behaviors over different salts. In addition to Figures 3.4.4, 3.4.5, and 3.4.6, Tables 3.4, 3.5, and 3.6 provide a compact, chronological summary of the nonlinear classifications across all salts. Interestingly, it seems that each device not only presents its own trends in cation selectivity, but its own nonlinearity profiles. Device 4, for example, seems to exhibit pre-dominantly linear I-V curves across all of the salts tested. Device 8, however, presents a large number of activated current-voltage curves. On the other extreme, I-V curves of all types can be found in Device 3 in roughly similar measure with the degree of nonlinearity changing dramatically over the course of the device's lifetime.

Stochastic Switching

In contrast to unpredictable long-timescale changes in the nanopore state (Figure 3.4.7), we also observed rare instances of rapid stochastic switching. This is a hallmark of biological ion channels resulting from dynamic changes in the conformational state of the channel which can be voltage gated, ligand gated, or mechanosensitive. In rare cases, switching events in graphene nanopores were noticed from a clear, voltage-

	Run 1	Run 2	Run 3	Run 4	Run 5	Run 6	Run 7
KCl	L	L	L	L	L	L	WA
$LiCl$	R	WA	R				
$CaCl_2$					WR	L	WR
$BaCl_2$					L	L	L
$MgCl_2$					L	L	L

Table 3.5: Device 6: Progression of nonlinearity over all salts during testing

	Run 1	Run 2	Run 3	Run 4	Run 5	Run 6	Run 7	Run 8
KCl	A	WA	(-)	WA	A	A	A	WA
$LiCl$	A	A	A					
$MgCl_2$					(-)	R (-)	A	
$CaCl_2$					A	A	A	
$BaCl_2$					WA	WA	A	

Table 3.6: Device 10: Progression of nonlinearity over all salts during testing

dependent increase in baseline fluctuations during measurement of current-voltage properties in devices 10 and 5 in 1 M KCl (Figure 3.4.8a,e). Real-time current traces indicate the presence of a baseline current (Figure 3.4.8b,f) with large current spikes occurring at sporadic intervals. Closer inspection shows that the waveforms for the switching events have complex inter-event fluctuations (Figure 3.4.8c,d,g). Similar waveforms have been frequently observed for many different synthetic ion channels in lipid bilayers. Based on the large range of fitted nanopore charge values, we explored protonation or ion association of functional groups on the nanopore interior as a potential mechanism for the origin of the multiple conductance states observed. Power spectral analysis of the current traces (Figure 3.4.8h) indicates that switching events have a single characteristic lifetime, indicating that the phenomena has a well-defined timescale consistent with protonation and deprotonation[58, 59]. This is further supported by the conductance model that is able to mimic the large amplitude of the switching events for reasonable changes in the nanopore charge; addition of 2e– changes current from 0.13 to 1.9 nA in Fig. 4a–d for a 0.8 nm pore, whereas addition of 1e– changes current from 1.1 to 2.2 nA in Figure 3.4.8e–g for a 1.05 nm pore. Remarkably, in both cases the current fluctuations occur only for negative voltage bias, which is expected for an asymmetrically located binding site where the proton or ion concentration increases as the local electric potential is modulated by either positive or negative (but not both) voltage biases.

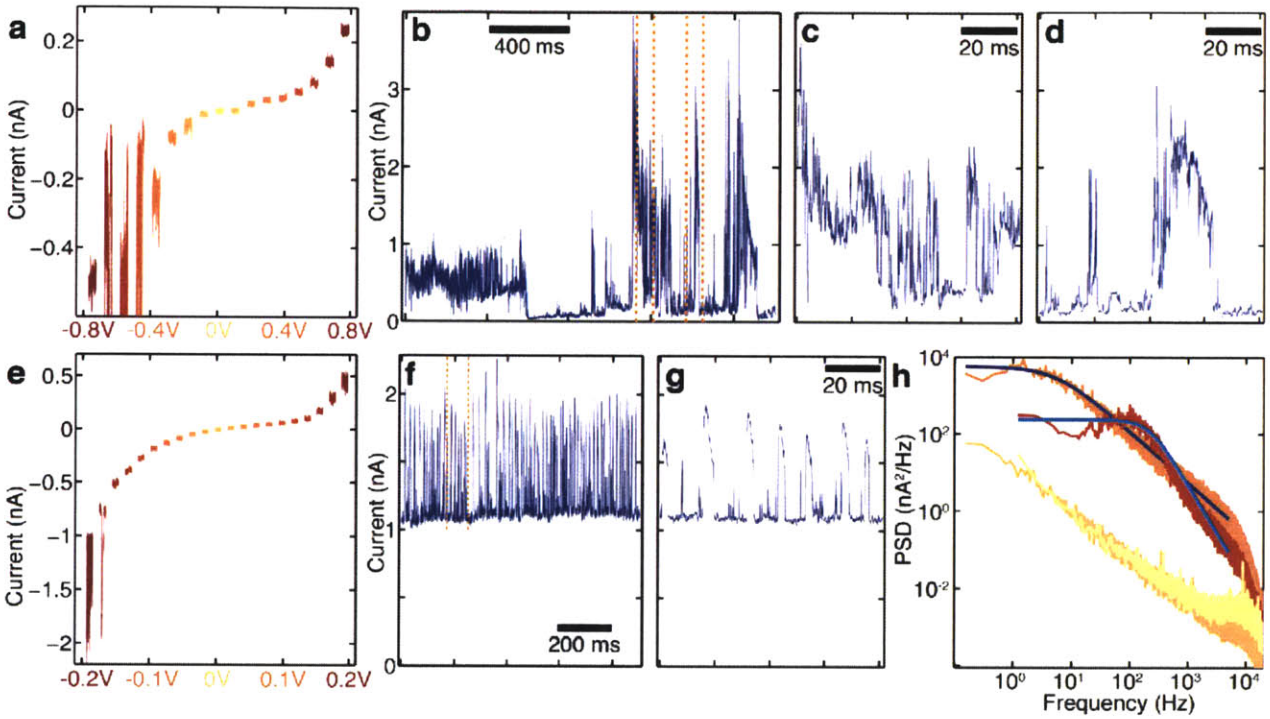

Figure 3.4.8: Voltage-activated switching of nanopore state. (a) Current-voltage curve with actual traces (400 ms long) showing voltage-dependent nanopore behavior (device 10 at 1 M KCl). (b – d) Close-up of real-time current trace at –600 mV. (e) Current-voltage curve with actual traces (400 ms long) (device 5 at 1 M KCl). (f, g) Close-up of real-time current trace at –200 mV. (h) Power spectral density for real time current traces exhibits a shoulder indicative of a single relaxation timescale only in in the presence of voltage-activated switching. Ochre: Device 10 at –600 mV, (orange: experiment, blue: Lorentzian with 25 ms timescale), Device 10 at –200 mV, Device 5 at –200 mV (red: experiment, blue: Lorentzian with 1 ms timescale), yellow: Device 5 at –80 mV.

Chapter 4

Structure-function relationship for graphene nanopores

This chapter will develop a method of calculating the relationship between a nanopore's structure and its ion transport properties. The theory for ion transport developed in Chapter 2 indicates that the transport rates of ions can in principle be directly calculated if the potential energy of the ion is known as a function of its position in the nanopore. The potential energy of the ion is a sum of the single ion potential, $\mathcal{U}^s(\vec{x})$, and the inter-particle potential, $\mathcal{V}^s(\vec{x}-\vec{x}')$. As a first approximation, states of the nanopore with more than one ion - where $s > 1$ and where the inter-particle potential $\mathcal{V}^s(\vec{x}-\vec{x}')$ is relevant - will not be considered. The validity of assuming the nanopore has only one ion in it will be discussed further, though it is important to remember that the probability of all nanopore states are weighted by the single ion potential $\mathcal{U}^s(\vec{x}) \approx \mathcal{U}(\vec{x})$. As of such, the single ion potential, $\mathcal{U}(\vec{x}) = \mathcal{U}_{pore}(\vec{x}) + \mathcal{U}_{external}(\vec{x})$, contributes in a priviledged way to the nanopore's transport properties. In this framework, inter-particle interactions are considered as a perturbation or modulation of the baseline properties defined by the potential in the nanopore. Therefore, this chapter will focus on calculating the potential energy from the nanopore structure - including both the nanopore geometry and charge distribution. The calculation of ionic transport rates will prove to be computationally efficient enough to perform across many nanopore structures and ionic species. From the resulting computationally constructed database of structure-function relationships, it becomes possible to estimate a real nanopore's structure from experimental transport measurements using a least squares minimization. The implications of this computational method for estimating a nanopore's structure will be illustrated with a specific example from the experimental data collected in Chapter 3, and represents a powerful example of how theory and experiments can be used in conjunction with each other.

4.1 Nanopore structure defines a potential

Throughout this thesis, the contribution of the nanopore to ion transport is bundled into both a potential energy term, $\mathcal{U}_{pore}(\vec{x})$ and the boundary conditions for solving the transport equations. Fundamentally, however, both the single ion potential $\mathcal{U}_{pore}(\vec{x})$ and the boundary conditions originate from interactions between atoms in the nanopore containing membrane and ions in solution. However, atoms in the membrane do not participate in transport, and their degrees of freedom are severely restricted by chemical bonds between atoms in the membrane. Therefore, it is well justified to assume that the nanopore structure can be accounted for with a potential field that depends only on the position of the ion and the global description of the nanopore structure - provided that a method for computing $\mathcal{U}_{pore}(\vec{x})$ is provided.

There are several interactions between ions and atoms in the membrane, including hard-sphere repulsion, proximity induced dehydration, electrostatic interactions, and van der Waals (polarization effects)[60]. Hard-sphere repulsion is taken into account by excluding the volume of the membrane from the accessible phase space for the ions in solution; in other words, by properly defining the boundary conditions for ion transport, hard-sphere repulsion does not need to be included into the nanopore potential. The same model for the nanopore geometry as Chapter 2 will be considered: a cylindrical nanopore with radius r_p. The accessible radial coordinates for an ion in the nanopore is then $r \in [0, r_p - r_i]$, where r_i is the radius of the ion. Therefore, each ion has a different accessible radial coordinate depending on the ion size after properly accounting for hard-sphere repulsion.

The remaining terms are then:

$$\mathcal{U}_{pore}(\vec{x}) = \mathcal{U}_{hyd}(\vec{x}) + \mathcal{U}_{el}(\vec{x}) + \mathcal{U}_{vdW}(\vec{x}) \tag{4.1.1}$$

It is generally accepted that the dehydration potentials and electrostatic potentials play the most significant roles in determining ionic selectivity. Therefore, the first model considered will directly compute the contributions of these two potentials, and exclude contributions from polarizability of the membrane and electronic correlations via van der Waals. To differentiate the potential, $\mathcal{U}_{pore}$ in the abstract sense from the computationally derived potential, from here on out, the potential in the nanopore, as used for the purposes of computing transport properties, is henceforth called $\varphi(r, z)$ and is calculated in a cylindrical coordinate system.

Diameter	Nanopore Volume	K^+Occupancy	K^+Occupancy	K^+Occupancy
nm	nm^3	at 400mM	at 1M	at 2.5M
0.4	0.071	0.0188	0.0470	0.118
0.8	0.284	0.0753	0.188	0.470
1.2	0.639	0.169	0.423	1.06
1.6	1.136	0.301	0.753	1.81
2.0	1.775	0.470	1.18	2.94

Table 4.1: Number of potassium ions in a graphene nanopore for different diameters and mean potassium concentrations.

Diameter	Nanopore Volume	Max Occupancy	Max Occupancy
nm	nm^3	No Water, only K^+	Full Hydration of K^+
0.4	0.071	0.35	0.8
0.8	0.284	29	1.2
1.2	0.639	65	3.1
1.6	1.136	115	5.6
2.0	1.775	180	8.7

Table 4.2: Maximum number of ions in a graphene nanopore under different conditions

4.1.1 Solving for single ion occupancy

In Chapter 2, we saw that the probability density of ions in the nanopore, and consequently, the current through the nanopore, depends on the ion occupancy of the nanopore. In turn, the probability of finding a specific number of ions in the nanopore, s, is determined by the master equation (equation 2.2.2). Interactions between ions include electrostatic interactions, hard-core repulsion, and a soft-shell repulsion from dehydration of the ions in proximity. Although rigorous analysis of the pair potential has not been performed here, it is likely that the repulsive terms in the nanopore make finding more than one ion in the nanopore at any given point in time relatively, and likely exponentially, unlikely. Furthermore, finding one positive ion and one negative is far more probable (due to their electrostatic attraction) than finding two like charged ions. As a result, this Chapter will focus on computing transport properties in the limit of one ion occupancy in the nanopore.

To better understand the relevance of electrostatic interactions between ions inside a graphene nanopore, simple back of the envelope calculations were done on the average number of ions inside the nanopore under different conditions (Tables 4.1 and 4.2). The calculations reveal that in the absence of enhancements in concentration inside the nanopore, there is on average less than one cation (and one anion) in a sub-2 nm graphene nanopore (Table 4.1). If the concentraton in the nanopore is significantly higher than bulk, however, the number of cations in the nanopore can be two or greater. The concentrations used in Table 4.1 cover a reasonable range of values; higher concentrations than 3M KCl in the nanopore require that ions begin to dehydrate their hydration shell to fit inside the nanopore (Table 4.2). Even at the concentration where the

highest number of fully hydrated ions are in the nanopore, a diameter greater than 1.4 nm is required before two cations and two anions can fit inside the pore. As a result, the assumption of single ion occupancy is a decent first approximation.

4.1.2 Model parameters

Clearly, computing $\varphi(r,z)$ will require a model for $\varphi_{hyd}(r,z)$, the dehydration energy and φ_{el}, the electrostatic energy. Emphasis is placed on models with no fitting parameters, i.e. the model can use previously measured or derived material properties, such as the radius (hydrated and ionic), charge, mass, and total hydration energy of an ion, but cannot rely on any assumed behavior - whether experimentally or theoretically - to estimate any parameter of the model. The model does require that the properties of the nanopore are known, and therefore this computational approach is a forwards problem; for *a given nanopore structure*, it can estimate the transport properties of that nanopore.

The three structural parameters that define the nanopore are the nanopore diameter, the amount of charge on the nanopore, and the position of the charge on the nanopore. To simplify the geometry, the nanopore is assumed to be a cylinder, and the charge density is approximated as a ring charge that can be located anywhere along the thickness of the graphene nanopore (Figure 4.1.1). The three parameters are used to compute the dehydration energy, $\varphi_{hyd}(r,z)$, and the electrostatic interaction between the ion and the ring charge, $\varphi_{el}(r,z)$. The sum of the two contributions gives the net free energy profile inside the graphene nanopore:

$$\varphi(r,z) = \varphi_{hyd}(r,z) + \varphi_{el}(r,z) \tag{4.1.2}$$

4.1.3 Approximate solution to the dehydration energy of an ion

To compute the current-voltage characteristics of graphene nanopores, a method is needed to estimate the dehydration penalty as a function of the position of the ion in the graphene nanopore. In bulk, the exact equilibrium hydration structure of an ion, including the total hydration energy E_{hyd}^{eq}, the number of nearest neighbor water molecules N_W^{eq}, geometric configuration of nearest neighbor water molecules, and the distance between the ion and water molecules r_{M-O}, are essentially determined by quantum mechanical force balance. Heuristically speaking, electrostatic ion-dipole interactions are balanced by electronic repulsion between different water molecules, and between water molecules and the ion in question. The role of electronic correlations, i.e. many body interactions, in determining the hydration structure of an ion implies that calculation of the dehydration penalty $\varphi_{hyd}(r,z) = E_{hyd}^{eq} - E_{hyd}(r,z)$, requires some quantum mechanical

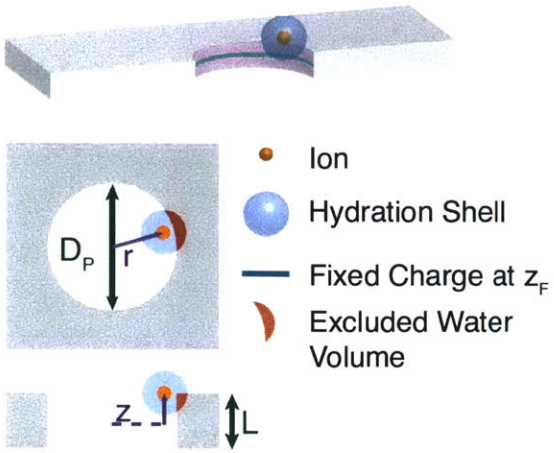

Figure 4.1.1: Model geometry for computing potentials

calculation. However, a number of simulations using density functional theory indicate that the energy of an ion hydrated by $E_{hyd}\left(N_W^i\right)$ water molecules is roughly proportional to the number of coordinating water molecules[61, 62]. As a first order approximation, we have that:

$$E_{hyd}\left(N_W^i\right) \approx E_{hyd}^{eq} \times \frac{N_W^i}{N_W^{eq}} \tag{4.1.3}$$

We can therefore write the mean energy of an ion at position r, z as an intermediate function of the mean number of water molecules coordinating at that position $\bar{N}_W^i\left(r,z\right)$. This results in the expression:

$$E_{hyd}\left(r,z\right) = E_{hyd}\left(\bar{N}_W^i\left(r,z\right)\right) \tag{4.1.4}$$

$$E_{hyd}\left(r,z\right) = \frac{E_{hyd}^{eq}}{N_W^{eq}} \times \bar{N}_W^i\left(r,z\right) \tag{4.1.5}$$

The mean number of water molecules coordinating an ion, $\bar{N}_W^i\left(r,z\right)$ is further estimated by considering the volume of the hydration shell excluded by the graphene lattice:

$$V_{hyd}^{eq} = \frac{4}{3}\pi\left(r_{M-O}^3 - r_I^3\right) \tag{4.1.6}$$

$$\frac{N_W^{eq}}{V_{hyd}^{eq}} \approx \frac{\bar{N}_W^i}{V_{hyd}\left(r,z\right)} = \frac{\bar{N}_W^i}{V_{hyd}^{eq} - V_{excluded}\left(r,z\right)} \tag{4.1.7}$$

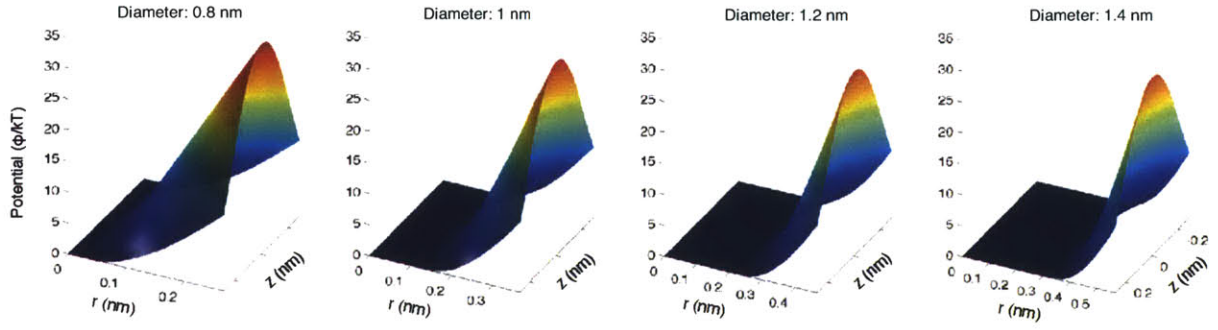

Figure 4.1.2: Dehydration energy profiles for graphene nanopores of different diameters computed for a Potassium ion.

$$E_{hyd}(r,z) = \frac{E_{hyd}^{eq}}{N_W^{eq}} \times \frac{N_W^{eq}}{V_{hyd}^{eq}} \times \left(V_{hyd}^{eq} - V_{excluded}(r,z)\right) \tag{4.1.8}$$

$$E_{hyd}(r,z) = E_{hyd}^{eq} \times \left(1 - \frac{V_{excluded}(r,z)}{V_{hyd}^{eq}}\right) \tag{4.1.9}$$

$$\varphi_{hyd}(r,z) = \frac{3}{4\pi} E_{hyd}^{eq} \times \frac{V_{excluded}(r,z)}{\left(r_{M-O}^3 - r_I^3\right)} \tag{4.1.10}$$

The excluded volume, $V_{exlcuded}(r,z)$ is computed by numerical Monte Carlo integration for each nanopore geometry and ion type. Sufficient accuracy for the Monte Carlo integration could be obtained for a single geometry and ion type on a laptop in MATLAB within several minutes. For this thesis, approximately 40 nanopore diameters, ranging from 0.3 nm to 2 nm were chosen and simulated for each of nine different ions. These simulations were run in C++ on a multi-core computer, and completed in about one day. Once these simulations have been performed, however, they do not need to be repeated, and other properties of the nanopore, and any other potentials in the nanopore, can be added without modification of this potential.

Examples of the potential surfaces for different diameter nanopores are shown in Figure 4.1.2. The surfaces indicate that near the radial edges of the nanopore, the dehydration barrier is the highest. As expected, we see a decrease in the dehydration barrier away from the center of the nanopore as ions are able to be partially hydrated by water molecules in bulk.

Recall that the current-voltage profiles are integral properties of the exponential of the potential $\varphi(r,z)$, in particular, of the radial averaged potential, (Eqn. 2.4.3). Looking at the definition of the radial averaged potential equation (Eqn. 2.4.3), it becomes clear that the smallest values of $\bar{\varphi}(z)$ dominate the integral. Furthermore, the shape of the radial averaged potential profiles can be roughly approximated with a quadratic

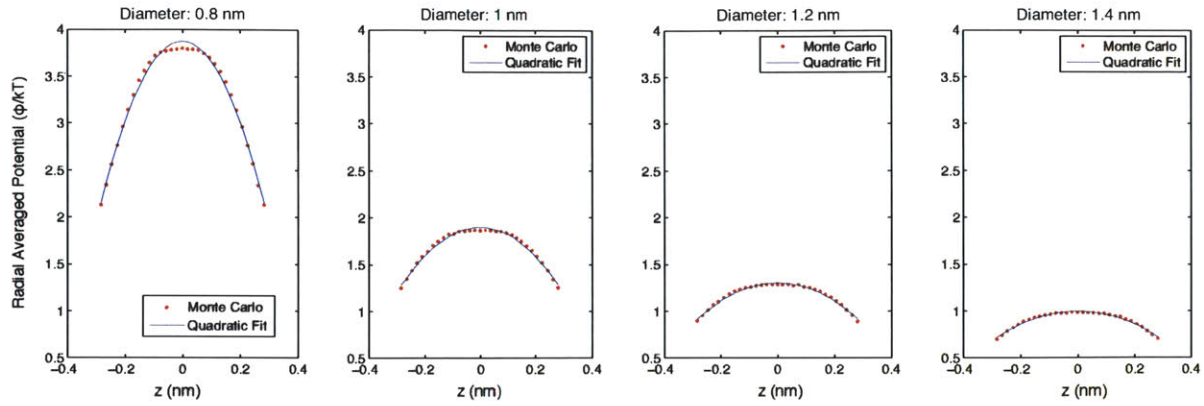

Figure 4.1.3: Dehydration energy profiles for graphene nanopores of different diameters computed for a Potassium ion.

polynomial (Figure 4.1.3):

$$\bar{\varphi}^i_{hyd} = a^i_1(r_P) - a^i_2(r_P)\, z^2 \tag{4.1.11}$$

4.1.4 Electrostatic interactions with the nanopore charge

Electrostatic interaction between an ion in the nanopore and a ring charge of z_P at a location $x_P \in \left[-\frac{L}{2}, \frac{L}{2}\right]$ along the transmembrane coordinate of the nanopore can be computed directly by applying Maxwell's equations and integrating numerically. The ion is assumed to be at a location of $(r, z, \phi = 0)$, and the distance, d_λ, to the differential line segment of charge located at (r_P, x_P, ϕ) is given by:

$$d_\lambda(r, z, \phi) = \sqrt{\left(r_P^2 + r^2 - 2 r_P r \cos\phi\right) + \left(z - x_P\right)^2} \tag{4.1.12}$$

$$\varphi_{el}(r, z) = \frac{z_{ion}}{4\pi} \int_0^{2\pi} \frac{z_P}{2\pi} \frac{1}{d_\lambda(\phi)} \frac{1}{\varepsilon\left(d_\lambda(\phi)\right)} d\phi \tag{4.1.13}$$

For the majority of nanopores considered, the distance, d_λ, is sufficiently small that the bulk dielectric permittivity of water cannot be used in computing the electorstatic interaction between the two charged species. However, the dielectric constant can be approximated as:

$$\varepsilon(d_\lambda) \approx \frac{\varepsilon_W - n^*}{\pi} \arctan\left[\alpha\left(d_\lambda - d_W\right)\right] + \frac{\varepsilon_W - n^*}{2} + n^* \tag{4.1.14}$$

From this function, it can be seen that the dielectric function reduces to the index of refraction, n^* as the

distance goes below the water molecule diameter, whereas for larger distances, there is a sharp transition to the dielectric permittivity of bulk water. Similar to the previous section, scaling analysis will be performed to understand the effects of $\varphi_{el}(r,z)$ on $\bar{\varphi}(z)$ and on the current.

4.1.5 External voltage contribution to the applied potential

The quadratic approximation to the dehydration energy means that, for uncharged graphene nanopores, we can derive an approximate analytic solution to the transport properties for any ionic species in the limit of single ion occupancy. To estimate transport properties, we need to compute the dependence of the current, I, on the applied voltage, V. The applied voltage, V, adds a potential to the nanopore, leading to a total nanopore potential of the form:

$$\varphi(r,z) = \varphi_{hyd}(r,z) + \varphi_{ext} \tag{4.1.15}$$

Where φ_{ext} represents the electric potential from an applied voltage across the nanopore. The boundary conditions for φ_{ext} are $\varphi(r, z = L/2) = V$, and $\varphi(r, z = -L/2) = 0$. From Poisson's equation, the potential drop across the nanopore can be given as:

$$\varphi_{ext} = \frac{ez_i(z + L/2)V}{k_B T L} \tag{4.1.16}$$

The radially averaged potential, as a function of the applied voltage

$$\bar{\varphi}_i(z;V) = \bar{\varphi}_i(z;V=0) + ez_i(z + L/2)V/k_B TL \tag{4.1.17}$$

And the integral of the potential appearing in the current equation (equation 2.4.3) can be directly integrated, with $\kappa = ez_i V/L$, and by shifting the coordinate system by $L/2$:

$$\int_0^L \exp\left[a_2\left(\frac{a_1}{a_2} + \frac{\kappa}{a_2}z' + z'^2\right)\right]dz' \tag{4.1.18}$$

$$\int_0^L \exp\left[a_2\left(z' + \frac{\kappa}{4a_2}\right)^2 - \frac{\kappa^2}{2a_2} + a_1\right]dz' \tag{4.1.19}$$

$$\exp\left[-\frac{\kappa^2}{4a_2} + a_1\right]\int_0^L \exp\left[a_2\left(z' + \frac{\kappa}{2a_2}\right)^2\right]dz' \tag{4.1.20}$$

Now defining a new variable $\lambda = \sqrt{a_2}\left(z' + \frac{\kappa}{2a_2}\right)$, the integration can be simplified. The limit of the

integral in λ are on the lower bound $\lambda^- = \frac{\kappa}{2\sqrt{a_2}}$ and on the upper bound $\lambda^+ = \lambda = \sqrt{a_2}\left(L + \frac{\kappa}{2a_2}\right)$

$$\frac{1}{\sqrt{a_2}} \exp\left[a_1 - \frac{\kappa^2}{4a_2}\right] \int \exp\left[\lambda^2\right] d\lambda \tag{4.1.21}$$

$$\sqrt{\frac{\pi}{4a_2}} \exp\left[a_1 - \frac{\kappa^2}{4a_2}\right] \left(\text{erfi}\left[\sqrt{a_2}\left(L + \frac{\kappa}{2a_2}\right)\right] - \text{erfi}\left[\frac{\kappa}{2\sqrt{a_2}}\right]\right) \tag{4.1.22}$$

Substituting the integral into the denominator for the current, we obtain:

$$I = D\pi \left(r_p - r_i\right)^2 \frac{c\left(r, \frac{L}{2}\right) e^{\varphi\left(r, -\frac{L}{2}\right)/k_B T} - c\left(r, \frac{L}{2}\right) e^{\varphi\left(r, -\frac{L}{2}\right)/k_B T}}{\sqrt{\frac{\pi}{4a_2}} \exp\left[a_1 - \frac{\kappa^2}{4a_2}\right] \left(\text{erfi}\left[\sqrt{a_2}\left(L + \frac{\kappa}{2a_2}\right)\right] - \text{erfi}\left[\frac{\kappa}{2\sqrt{a_2}}\right]\right)} \tag{4.1.23}$$

Here, the concentrations and the potential at the boundaries are both known, and $\kappa = ez_i V/L$ is just a non-dimensional voltage. Therefore, analytic estimates for the current of arbitrary ions can be obtained for uncharged graphene nanopores as a function of voltage - provided that the Monte Carlo simulations are performed to compute, and fit to the quadratic model, the dehydration potential beforehand.

4.2 Characterizing model dependence on nanopore properties

From the nanopore potential profiles, the I-V characteristics can be directly computed given *a priori* knowledge of three nanopore properties, the nanopore diameter, the charge on the nanopore, and the position of that charge. Collectively, these three parameters will be refered to as θ. In this section, the potential profiles $\varphi\left(r, z \middle| \theta\right)$

The model has three parameters: the nanopore diameter, the nanopore charge, and the position of that charge. We wanted to understand how changes in these parameters affect the I-V curves predicted by the Nernst-Planck equation. Figure 4.2.1a, shows that the conductance transitions from access resistance dominated at large pore sizes to limited by dehydration effects in the nanopore as the size decreases. Adding charge to the nanopore increases the conductance compared to uncharged nanopores. At a nanopore charge of about $3e^-$, the nanopore resistance is effective shorted by the nanopore charge until the nanopore diameter goes below the hydrated diameter of the ions. In Figure4.2.1b,we find that dehydration results in activated current-voltage profiles, while adding nanopore charge results in saturated current-voltage profiles. Both these behaviors can be linked to their corresponding impact on the concentration profile inside the nanopore. Dehydration depletes the concentration in the nanopore, and as the voltage increases, the concentration in the nanopore increases as well due to the lower energy penalty for being in the pore. In Figure4.2.1c we see that if the charge on the nanpore is not in the center, the resultant I-V curves exhibit rectified behavior, with

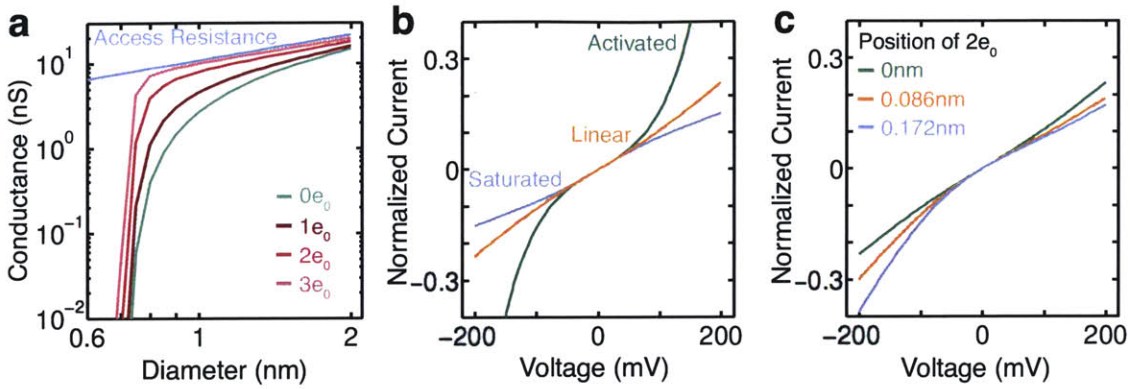

Figure 4.2.1: Characterizing the effects of the estimated nanopore potential. (a) Conductance as a function of diameter for different nanopore charge. (b) Pore diameter and charge determine whether I-V curves are linear (1.0 nm, 0e-), activation-type nonlinear (0.7 nm, 0e-), or saturation type nonlinear (0.85 nm, 6e-). (c) Current rectification as the charge moves off-center for a 0.85 nm diameter pore with 2e-.

the degree of rectification increasing as the charge moves further and further off center.

These model characterizations show that the conductances of sub-2 nm diamter graphene nanopores is in the same range as the experimentally measured conductances. Importantly, however, the model establishes a relationship between the conductance and nonlinearity. For example, as the nanopore diameter decreases, the conductance drops off significantly while simultaneously changing the nonlinear profile. It is therefore expected that there is a narrow range of nanopore properties that can model the behavior of a given current-voltage profile.

The predicted functional properties are similar to those observed in experimental measurements. For example, the dehydration of ions causes the conductance to span three orders of magnitude as the diameter of the nanopore decreases, and all of the nonlinearities predicted by the model are observed experimentally. The order of magntidue for the conductance and the degree of nonlinearity are also similar to experimental observations.

4.3 Application of theory to experimental data sets

4.3.1 Discussion of least-square nanopore structure estimation

The functional properties of a graphene nanopore are computed for *a priori* known nanopore geometries. This section seeks to determine the extent to which the theory can be used to predict the *actual* structural properties of experimentally measured graphene nanopores. Estimation of nanopore properties from functional measurements has been explored before, and defines a class of problems known as inverse problems[63]. In an inverse problem, some parameters of a differential equation are estimated from known values of the so-

lution. In this particular instance, the unknown parameters in the model are the nanopore diameter, charge, and position of the charge. These parameters will determine potential in the nanopore and the resultant current-voltage curve. Relying on the analogy with semiconductor physics, Burger and Eisenberg discuss in their paper the extent to which inverse problems are ill-posed mathematically[63]. Their conclusion is that the ability to measure over multiple different concentrations should improve the ability to estimate the nanopore properties.

The model developed in this section suggests that the problem is slightly less ill-posed than might be expected from that discussion. The conductance of graphene nanopores varies over three orders of magnitude for nanopore diameters between 0.4 nm and 2 nm. Therefore, the absolute value of the conductance in the linear regime can be used to estimate the diameter of a graphene nanopore to within a few Angstroms. The atomic thickness furthermore limits the number of charges that can be present on the perimeter of the graphene nanopore. Furthermore, if the model developed in this section accurately represents the behavior of graphene nanopores, then the nonlinear behavior should further help specify the problem. Of particular note here is that there are three unknown parameters in this model, (1) the nanopore diameter, (2) the nanopore charge, and (3) the position of the charge, and there are three types of nonlinear behaviors (1) activated current-voltage curves, (2) saturated current-voltage curves, and (3) rectified current-voltage curves. Therefore, the particular instance of structural estimation for graphene nanopores using the model above should be much better conditioned than the general class of problems.

One of the other challenges with the inverse problem framework is that it typically requires solving the differential equation multiple times until the correct parameters are estimated. This approach was not taken in this thesis. Instead, an entire database of current-voltage curves was generated. The database spanned 41 nanopore diameters, 33 values of the nanopore charge, and 31 values for the position of the charge in the nanopore, corresponding to a total of almost 20,000 nanopore structures. Current-voltage curves (at 100 voltage points in each curve) were generated for each of the 20,000 nanopore structures and for each of the eight different ions simulated. The inverse problem could therefore be reduced to a least-squares problem. For each experimentally measured current-voltage curve, a nanopore structure was assigned from the simulated current-voltage curve that minimized the least-squares residual.

Even with the least-squares method, it is important that the correspondence between the current-voltage curve and the predicted structure be one-to-one and not one-to-many. The main advantage of the method used in this thesis is that the approximations for nanopore transport make solving the forward problem - i.e. solving for the current-voltage curves - computationally easy. There are nonetheless several errors in the inverse problem, such as model errors (not all nanopores have cylindrical symmetry), discretization errors (the true best fit structure was not simulated), and uniqueness errors (the algorithm returns a close fit from

an incorrect structure). As discussed by Burger et al.[63], one method to improve the accuracy of a fit is to use measurements over several different concentrations. One of the challenges with using concentrations, however, is that the concentration scaling of transport properties are not known *a priori*. In fact, developing an experimentally verified theory for how the conductance changes with concentrations is a very significant outstanding problem in this nascent field of graphene nanopores. Specifically, the concentration dependence of the conductance will inevitably require solving the coupled transport problems between the reservoir and the graphene nanopore - a problem that was in this thesis framed, but not solved.

4.3.2 Case study: nanopore structure estimation and theory validation

Instead, our experiments focused on measuring different ion types at the same concentration. Measuring different cations is in principle a better way of investigating the extent to which the finite size impacts the overall nanopore potential and, through it, the transport rates. The *fundamental* assumption, however, is that the nanopore is the same even if the cation changes. If the transport model is correct (i.e. up to model, discretization, and uniqueness errors), then the same nanopore structure should be obtained from least-squares fitting of each of the different current-voltage curves. This hypothesis was investigated by comparing the nanopore diameter obtained by least-squares fitting of the data sets presented in Chapter 3. From the data (Figure 3.4.7), it would seem that the major source of uncertainty is the variability in the conductance over time for the same salt. Therefore, nanopore fits were averaged over the salt type. For example, a reported best fit nanopore diameter for potassium chloride would average the best fits of all seven current-voltage curves of KCl, and the best fit for lithium chloride would average over all three current-voltage curves for LiCl. The variance in the best fits for a single salts determines the precision with which the structure of a nanopore can be estimated from the model given intrasalt variability. In our experiments, this uncertainty was typically on the order of $0.1 - 0.2\,nm$, depending on the salt. With this degree of variance, there were no statistically significant differences in reported nanopore diameters for different salts.

As a more carefully constructed hypothesis, we compared the predicted nanopore structures for monovalent salts and divalent salts separately. In other words, the nanopore structure obtained from best fits over all monovalent salts were averaged and reported as a single diameter and charge, and all the structural fits from divalent salts were averaged into a single diameter and charge. These averaged values are reported for the three different graphene devices, Device 3, 4, and 8 in Figure 4.3.1. If the theory is accurate, then one would expect that the fitted nanopore diameter would be the same, irrespective of whether a monovalent or divalent salt is being measured. Figure 4.3.1a indicates that the difference in the averaged diameter is not statistically different. We found, however, that the fitted nanopore charge, however, *was* statistically different between

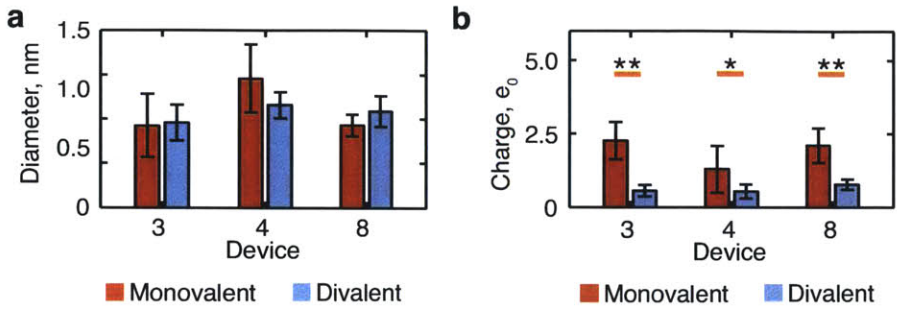

Figure 4.3.1: Least-squares nanopore structure estimation from experimental data. (a) Estimated nanopore diameter for Devices 3, 4, and 8. (b) Estimated nanopore charge for Devices 3, 4, and 8. Fitted structure for all monovalent salts are averaged into a single estimated diameter, as are all fitted structures for divalent salts.

monovalent and divalent salts (Figure 4.3.1b). Divalent salts consistently see a lower nanopore charge than monovalent salts - with a very high degree of confidence. The conclusion from this observation is that there is some dependence of ionic transport on the ionic charge that is not included in the transport model being used.

Although the transport model can reliably provide estimates of a graphene nanopore's properties, it is truly remarkable that the transport model can also be concretely tested using this "self-consistency" method. Self-consistently verifying the validity of a transport theory, however, requires a large amount of experimental testing, as nanopore transport properties have to be measured over many different salt concentrations or different ion types (preferably both). Chapter 5 focuses on developing a device architecture that would significantly increase measurement throughput. One major goal enabled by this general approach would be to develop a fully verified transport theory and use it to design nanopores with specic selectivity and transport characteristics.

Chapter 5

High throughput measurement of individual graphene nanopores

The ability to characterize an entire distribution of graphene nanopores in a membrane serves two distinct and complementary functions: screening of graphene synthesis conditions for optimal transport properties, and developing databases with which theoretical models can be accurately tested using self-consistency. This chapter focuses on developing a device architecture for high-throughput measurement of single graphene nanopores.

5.1 Motivation: screening synthesis parameters to optimize transport distributions

One method for controlling the distribution of sub-nm distributions of graphene pores is to introduce dopants during CVD synthesis[23]. At the moment, however, there are no methods available for functional characterization the distribution of nanopores in the material. There are a number of structural characterization techniques: raman spectroscopy provides some information about the bond structure, x-ray photoelectron spectroscopy can help inform elemental composition, and electron microscopy can directly visualize nanopores in the material. While aberration corrected TEM and STEM can uniquely characterize the structural distribution of nanopores in the material, these two methods are also time consuming and not easily accessible. Current methods for functional characterization are no better; it would take a perfectly programmed, machine-like operator one year of continuous, non-stop device fabrication and testing to characterize 100 graphene nanopores with the methods used in Chapter 3.

In comparison, it is possible to synthesize graphene under different CVD conditions within less than a week - orders of magnitude faster than current functional characterization techniques. Our aim, therefore, was to create a device that can independently measure 100 graphene nanopores within a couple of days - at which point the rate of functional testing would be commensurate with the rate at which new graphene samples could be synthesized using CVD. Combined synthesis and functional characterization would furthermore enable a feedback loop between the two, wherien functional measurement is used to screen and optimize synthesis methods.

Measurements with single pore resoution can significantly enhance feedback between CVD synthesis and functional characteristics. Larger area measurements have the property that they average over the behavior of large numbers of graphene nanopores. However, the contribution of each nanopore is weighted by their conductance, which scales quadratically with the diameter. Using large area measurements to perform feedback on CVD synthesis provides a measure of aggregate selectivity only. In contrast, we anticipate that measuring the distribution could help isolate how many off target pore sizes and functionalizations are made, and test strategies for mitigating them.

5.2 Extending statistical isolation to arrays

In Chapter 3, it was demonstrated that statistical isolation of individual graphene nanopores occurs when the diameter of the silicon nitride support nanopore for the graphene membrane is less than the average spacing between defects. When graphene is transferred to an array of silicon nitride nanopores, each suspended area independently satisfies the criterion for statistical isolation. From a device architecture perspective, the main challenge therefore is the ability to electrically measure ionic current through each of the suspended graphene areas independently. Each suspended graphene area has to have at least one of its reservoirs fluidically and electrically isolated from each other.

The standard method of providing electircal and fluidic isolation for biological nanopores is to fabricate the microwells on a silicon or glass wafer with electrodes on their bottom surfaces[64, 65]. The membrane over the well provides an electrical and fluidic seal between the electrode at the bottom, and a common ground electrode on the other side of the membrane. This conventional format has the advantage that many in principle hundreds of thousands of microwells can be patterned on the same substrate[66] - though throughput is predominantly limited by the number of channels on the transimpedance amplifiers[67, 68, 69]. While each well can be electrically addressed vis-a-vis the electrodes at the bottom of the well, the volume of fluid encapsulated by the well is typically fluidically completely inaccessible. Rinsing that the interior volumes of the microwells is extraordinarily difficult in the microwell format. Given that testing the graphene

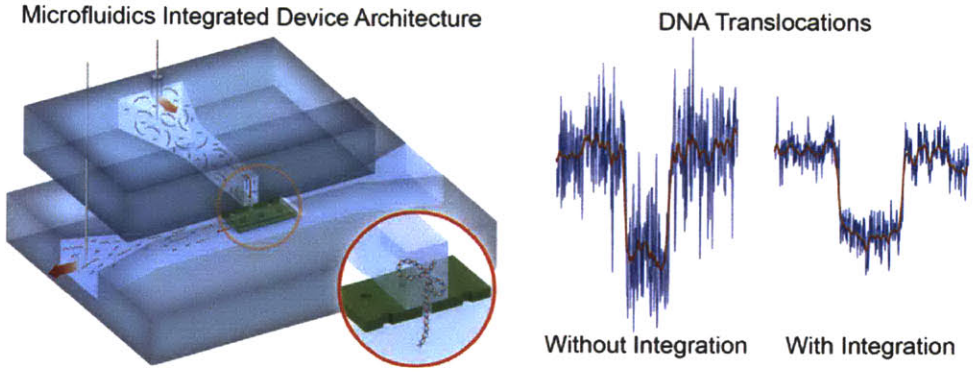

Figure 5.2.1: Original concept for noise reduction in solid-state nanopores through microfluidic integration

nanopores requires testing over large numbers of different salts and concentrations, the inability to rinse the interior volume of the microwell virtually precludes its use.

For the purposes of solid-state nanopores, a more serious issue with the microwell format, is the inability to *fill* the interior volume of the microwell with fluid. Unlike for lipid bilayer membranes, the solid-state membrane is deposited over the well before fluid fills the microwells. Solid-state nanopore systems are, in general, incompatible with micro-well based approaches, and it is expected that fluidic integration provides the dominant limitations to high-throughput integration[70]. In designing a new device architecture, one of the design criteria was creating a device architecture where both sides of the membrane could be addressed both fluidically and electrically. To achieve both electrical addressability and fluidic addressability, we employed a microfluidic integration scheme for solid-state nanopores that integrated active valves[71].

5.2.1 Microfluidic integration of solid-state nanopores

A few years back, we developed an device architecture that embedding solid-state membranes, and nanopores, between microfluidic channels[57]. The devices were first conceived of to reduce capacitive noise at high bandwidths for electronic measurements of DNA translocating through solid-state nanopores (Figure 5.2.1). In the context of ion transport through graphene nanopores, it was clear that the device architecture also met the needs of fluidic addressabilty of both the reservoirs on either side of the solid-state membrane. Specifically, in the microfluidic device, the microchannels on either side of the membrane had both an inlet and an outlet, thus making the devices perfectly amenable to rinsing of the fluidic volumes on either side of the membrane.

In the device format, a thin (usually $50\,nm$ or thinner) silicon nitride membrane is "stamped" on top of a microchannel in a first substrate. A second microchannel bearing substrate is then aligned and bonded on top

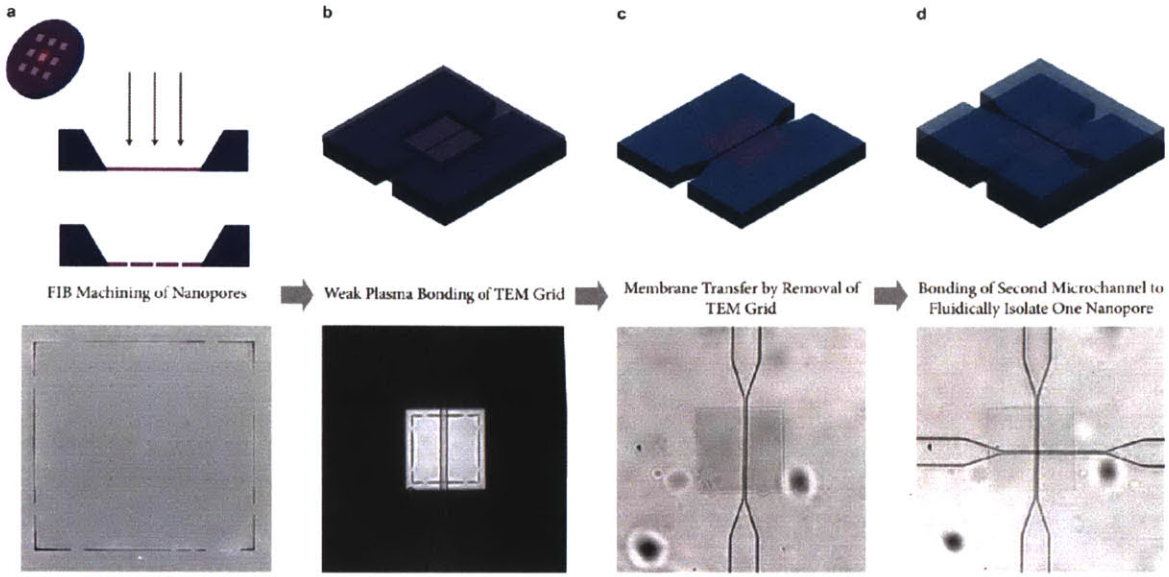

Figure 5.2.2: Device fabrication procedure for integrating a solid-state membrane into a microfluidic device.

of the first substrate. With proper alignment, this configuration results in two perpendicular microchannels with a silicon nitride membrane providing electrical and fluidic barrier for transport between the two channels. Similarly, when a nanopore is made in the membrane, it provides a conduit for ionic transport between the two channels that can be measured with a pair of electrodes placed in each channel. Large nanopore arrays were made with a Ga^+ FIB in the silicon nitride membrane with the same pitch as the width of the two microchannels on either side of the membrane. The fabrication process, summarized in Figure 5.2.2, can also be found in Jain et al.[57].

Upon integration of the nanopore bearing membrane, a single silicon nitride nanopore was statistically isolated between the two microchannels. Unlike statistical isolation of the graphene nanopores, however, there is a very high probability of obtaining a single silicon nitride nanopore between the two channels, and both the nanopore density and the microchannel widths were known very well - in the case of graphene nanopores, we can only provide crude estimates of the density of nanopores.

We reasoned that the device would enable measurement of statistically isolated graphene nanopores if graphene was transferred onto the nanopore-bearing silicon nitride membrane before it was deposited into the microfluidic device. Therefore, the main challenge we focused on was design of the devices for automated and multiplexed measurement of multiple nanopores in the same device.

5.2.2 Methodology for multiplexed measurement of solid-state nanopores

By increasing the number of microchannels in the top substrate, we hypothesized that it was possible to embed multiple nanopores into the same device. New devices were designed to have microchannels with a $3\mu m$ width, a $6\,\mu m$ spacing, and with a $3\,\mu m$ pitch for the square array of nanopores in the SiN_x membrane. In doing so, each microchannel in the top substrate connects to the single microchannel in the bottom substrate through a single nanopore in the silicon nitride membrane (Figure 5.2.3). In figure 5.2.3 each microchannel in the top substrate is fluidically and electrically isolated by the insulating walls of the microchannel. Furthermore, the schematic illustrates how all eight nanopores are be electrically and fluidically isolated within a small area of $100\,\mu m \times 100\,\mu m$.

Electrical connections of the fluidic channels

The single channel in the bottom substrate was connected to an external Ag/AgCl electrode via a larger downstream microchannel, and acted as a common ground for all nanopore measurements. The on-chip reservoir that interfaced with the Ag/AgCl electrode had a minimum diameter of $1\ mm$. Device designs in which each of the eight microchannels in the top substrate were given their own external electrode were quickly deemed sub-optimal.

1. A spacing of $2\ mm$ between external electrodes would require a device format of $(1.6\,cm)^2$, most of which is taken just to increase the spacing between the microchannels in the top substrate from $3\,\mu m$ to $2\ mm$

2. At $2\,mm/channel$, a 96 pore device would be unrealistically large, i.e. at best $(8 - 10\,cm)^2$

3. Using external electrodes for each channel increases the length of each microchannel; this in turn increases the rinsing time. The criteria of $<$ 10sec rinsing of the channels could not be satisfied with this format

4. Each of the eight channels would have to be individually rinsed with new solutions. This becomes even more problematic as the number of pores increases

5. Insertion of eight electrodes into the device adds a lot of mechanical complexity - each reservoir and electrode has to be individually debugged to check for any bubbles

There were in fact, multiple bottlenecks in designing devices with external electrodes for each channel. One alternative was integrating electrodes with smaller profiles ($\tilde{}200\,\mu m$) directly into the device. Integration of

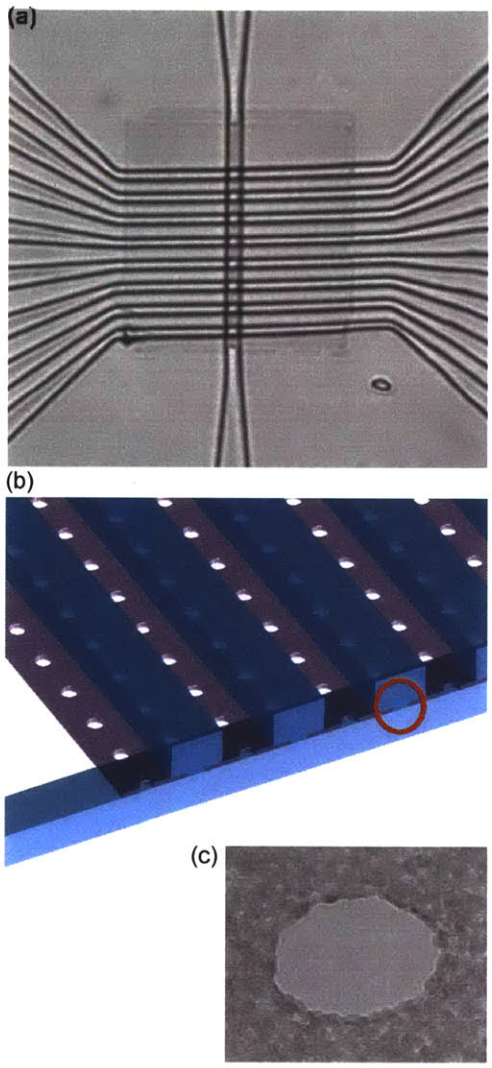

Figure 5.2.3: Embedding multiple solid-state nanopores into a microfluidic device. (a) Optical microscope image of a device with eight pores embedded in it. Above the membrane, in the top substrate there are eight parallel microchannels, whereas previous versions of the device had only one channel. (b) Schematic illustrating that a single silicon nitride nanopore provides fluidic connection between one channel in the top substrate and the single channel in the bottom substrate. The blue color represents the fluid in the microchannel. (c) TEM image of a silicon nitride nanopore with a 35nm diameter.

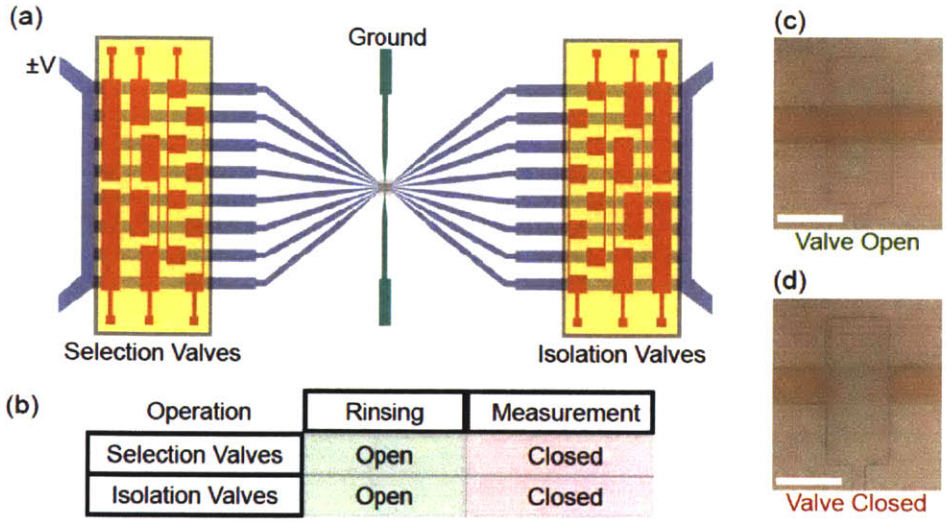

(b)

Operation	Rinsing	Measurement
Selection Valves	Open	Closed
Isolation Valves	Open	Closed

Figure 5.2.4: Device architecture for mulitplexed solid-state nanopores in microfluidic devices. (a) Drawing of different layers in the microfluidic device. Green indicates microchannels in the bottom substrate, purple indicates microfluidic channels in the top substrate, and red indicates microfluidic channels in the control layer substrate located above the "top substrate". Pressurization of the red channels causes channels in the top substrate to collapse, creating both a fluidic and electric seal. (b) Table indicating that microfluidic valves can all be opened to allow all fluid rinsing of all simultaneously. Closing the valves after rinsing restores electrical isolation between the different channels. (c - d) Optical microscope images of a microfluidic channel in its open and closed state respectively. The microchannel in the top substrate is filled with food dye for visualization.

Ag/AgCl electrodes would solve many of these problems, but with the trade-off that it would add significant additional complexity to device fabrication. A review of the microfluidics literature indicated that most electrode integration schemes were not immediately compatible with our microfluidic architecture without time consuming optimization and experimentation. Most importantly, however, integrated electrodes alone did not solve the problem that each of the eight channels would have to be rinsed independently.

In light of this discussion, a device architecture using microfluidic valves was devised (Figure 5.2.4). In this architecture, the eight microchannels depicted in Figure 5.2.3 connect upstream and downstream to a single microfluidic channel. Microfluidic valves are placed before the channels connect to the single upstream and downstream microchannels. For fluidic rinsing of the device, the valves are all kept open, and new solutions can be rinsed from the single upstream microchannel of the single downstream microchannel, simultaneously rinsing all eight microchannels where the nanopores are present. Following rinsing, valves are operated to disconnect the downstream channel from the eight microchannels (these valves are called isolation valves). Another set of valves is used to selectively disconnect seven of the eight microchannels from the upstream microchannel. During electrical measurement, an Ag/AgCl electrode is placed in a reservoir connected to

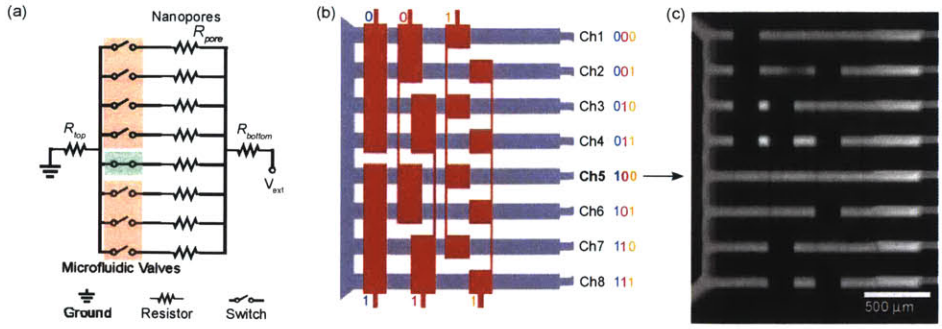

Figure 5.2.5: Using microfluidic valves to address individual nanopores. (a) An equivalent circuit diagram indicating the use of microfluidic valves as electronic switches (b) A multiplexing valve array for efficiently addresing one of eight channels in binary (c) Epifluorescence image showing valve actuation during one of the microfluidic states.

the upstream microchannel.

This device concept requires microchannels closed by microfluidic valve actuation result in a high electrical resistance[72] in addition to a high fluidic resistance. The electrical resistance of a microfluidic valve was found to be in excess of 10 $G\Omega$, significantly higher than any nanopore that would be placed in the circuit. Therefore, microfluidic valves can be thought of as electrical switches in fluidic circuits (Figure 5.2.5).

5.3 Device fabrication protocol

The microfluidics multiplexed solid-state nanopore devices consisted of a bonded three-layer polydimethylsiloxane (PDMS) stack (each layer designated from top to bottom as the control layer, top flow layer, and bottom flow layer), with a thin (50 nm) solid-state membrane between the top flow layer and the bottom flow layer. Multilayer soft-lithography was used to create microchannels in the control layer and the ~ 30 µm thick top flow layer alongside valves between the layers[71]. Nanopores were then integrated into the device using a method described elsewhere[57], with the control layer – top flow layer composite acting as one substrate, and the bottom flow layer acting as the other, and with the solid-state membrane being embedded between microchannels in the top flow layer and bottom flow layer. To fabricate the control layer, PDMS (Sylgard 184, with a polymer to curing agent ratio of 5:1), was degassed under vacuum for 30 minutes, poured over a photolithographically defined mold, and cured for 23- 25 minutes at 75°C. After curing, the control layer was punched with access ports for the control channels. For the top flow layer, PDMS (20:1 ratio) was degassed, spin coated onto the top flow layer mold (2300 rpm for 2 minutes), and cured for 30 minutes at 75°C. The control layer and top flow layer were then treated with oxygen plasma (60s, 1700W at 500mTorr of air at atmospheric composition, Harrick Plasma PGC-001), aligned, brought into contact, and cured in the oven

at 75°C for 4 hours. The spin coating of PDMS resulted in an approximately 30μm thick film, with a 20 μm thick membrane separating channels in the control layer and top flow layer that overlap. The thickness of this membrane determines the required operating pressure for the membrane to deform and close the channel beneath it with a high electrical and fluidic resistance. After peeling off the flow layer and control layer from the silicon mold, a nanopore containing membrane was aligned and deposited onto the eight parallel channels of the flow layer. The bottom flow layer piece was prepared identically to the control layer. Both of the flow layers were then plasma treated for 60 seconds, aligned, and brought into contact. Devices were further cured for 24 hours at 75°C prior to subsequent use. In graphene-based devices, the membrane was deposited onto the bottom flow layer instead of the top flow layer, and steps involving plasma treatment of the graphene surface were omitted. All other steps for the graphene membrane based devices remaining identical. Features in the mold for the control layer were patterned using SU-8 photolithography (SU-8 2010, 3000 rpm). Similarly, SU-8 photolithography (SU-8 2005, 3000 rpm) was used to pattern the highest resolution features (4.5 μm square microchannels in the active region under and over the membrane) and all other sub-80 μm features in the top and bottom flow layer molds. The remaining features in the flow layer molds were patterned with AZ photoresist (AZ-5214, 2000 rpm), and rounded through a heat exposure (150C for 15 min). To maintain symmetry in resistances, larger features in the bottom flow layer were patterned using the same protocol, despite the lack of actuation of these channels. The patterned molds were silanized with perfluoro-1H-1H-2H-2H-trichlorooctylsilane for 45 minutes prior to performing any soft-lithgraphy.

Devices with graphene-SiNx membranes

To integrate graphene into the devices, graphene was transferred onto the silicon nitride membrane after making a square array of nanopores using the Ga^+ focused ion beam. The same transfer process as in Chapter 3 was used. Following transfer, cuts were made around the membrane to facilitate membrane deposition. The membrane was then deposited on the bottom substrate (not the top substrate as described in the previous section), resulting in the graphene in contact with the substrate with only one microchannel. Although the oxygen plasma of the nitride membrane was omitted, the bottom substrate was plasma treated prior to membrane deposition. The top substrate was then plasma treated and aligned with the bottom substrate. In this way, plasma treatment of the graphene was avoided, while also provided for plasma assisted bonding of the two PDMS pieces.

System operation

Activation of the microfluidic valves required selectively pressurizing microchannels in the control layer using solenoid valves. The solenoid valves (Pneumadyne) were operated with a USB controller through Matlab.

All electrical measurements are performed using a low noise, high gain transimpedance amplifier (Axopatch 200B), with a 14-bit digitizer (Digidata 1440). Synchronization of valve operations and electrical recording was performed using the automation software, AutoIT, allowing for the scripting of complex protocols for channel switching and fluid handling.

5.4 Demonstrations

Multiplexed measurements in solid-state nanopore devices can enable nanopore devices to perform (i) efficient optimization of nanopore properties, (ii) screening and analysis of the physicochemical properties of molecules over several parameters, and (iii) measurement of variability in a nanopore system. We demonstrate that the microfluidics architecture presented herein is compatible with each of the different uses through testing of a model system for each of these operational configurations. To illustrate the potential for optimization of nanopore properties, a membrane was patterned with nanopore sizes that decreased across the membrane. Multiplexed devices were then fabricated with the pore size array membranes positioned with the gradient perpendicular to the eight parallel microchannels in the top flow layer, and conductance measurements were then taken across multiple nanopores of varying size. The size of a nanopore is one of the most important parameters, as it acts to determine the performance of the device by defining the electrical resistance of the nanopore, thus, it affects the open pore current, and the contributions of both thermal noise and flicker noise. In addition to this, the relative size of the nanopore to molecular analytes determines the available conformations of the molecule, the sampling of the fluidic velocity field profiles, and the electronic signatures measured during molecular translocation. Nanopores fabricated using a Ga+ ion beam are expected to be conical, with the nanopores becoming increasingly cylindrical with increasing ion beam dose and milling. Upon measuring the conductances of the nanopores in the device, we find that the conductance decreases monotonically across each measured channel (Figure 5.4.1a). For one of the nanopores, the measured resistance was equal to the seal resistance of a junction without a nanopore. While it is possible that the nanopore was clogged or fouled at the onset of measurement, we note that rotational misalignment of the device causes the probability of having a pore in the junction to be less than unity (i.e. statistically, not every junction should necessarily contain a nanopore). The approximately linear variation of the conductance with respect to the ion beam dose is likely attributable to the shape evolution of a nanopore with increasing dose.

To illustrate the ability to measure the nanopores over multiple different parameters, the conductance of each of the nanopores in the nanopore size array was measured at different ionic concentrations. At low concentrations, the surface charge of the silicon nitride enriches the concentration of counter-ions in the nanopore, leading to a leveling of the conductance with decreasing concentration (5.4.1b). The data reveals,

however, that there is a slight variation between the nanopores, suggesting the presence of variation in the surface charge in addition to the evolving shape profile of the nanopores. Possible origin for a variation in surface charge is a difference in implanted Gallium during milling of the nanopore or hydrocarbon/contaminant adsorption. The ability to measure the same analyte in nanopores of different sizes could be useful for understanding the dynamics of molecules, such as proteins, where there is significant heterogeneity in cross-section and surface charge. This demonstration also suggests the possibility of measuring the same analyte across nanopores that are treated with different functionalizations, allowing for screening of the optimal functionalization of a nanopore. The data evidence the fact that the effects of different solutions or analytes can be tested on nanopores of different sizes or functionalizations, making the devices a flexible platform for the development of new nanopore based biological assays. As a demonstration of the devices ability to measure variability across nanopores, we next integrate a graphene membrane over a silicon nitride nanopore array, and measure the conductance through small areas of CVD graphene. Following integration of graphene into the device, in comparison to the large ($>$ 100 nS) conductances measured for ~ (30 nm) SiNx nanopores, the measured conductance with graphene transferred over the SiNx nanopores was typically less than 10 nS. The conductances measured indicate graphene nanopores smaller than 2 nm in most cases. The large variability of the current across the graphene membrane is likely a consequence of the heterogeneous distribution of defects in the graphene growth process. These measurements across graphene thus provide a specific example of the ability of multiplexed nanopores to measure heterogeneity in an analyte, and open the avenue for high-throughput functional characterization of manufacturing techniques for two-dimensional materials.

The last functional test in the multiplexed devices was to transfer graphene onto the silicon nitride membrane with an array of 40 nm nanopores. At this silicon nitride nanopore diameter, the criteria for statistical isolation of graphene nanopores is satisfied. Therefore, by transfering of graphene to the silicon nitride membrane, our aim was to demonstrate that multiple graphene nanopores could be statistically isolated and measured in the microfluidic devices. The original device fabrication procedure involved oxygen plasma treatment of the PDMS surfaces. To successfully integrate graphene into the microfluidic devices, the fabricaiton process had to be modified. These modifications are described in the device fabrication section. Conductance measurements at 100mM KCl are shown in Figure 5.4.2. The measured conductances were found to be lower than the conductance of the silicon nitride nanopores at the same concentration - suggesting that graphene is indeed covering the silicon nitride pores. The conductances are furthermore in the same range as those measured in Chapter 3 for graphene nanopore. An interesting feature of the data, however, is that five of the nanopores have very similar conductance. The size of these nanopores cannot

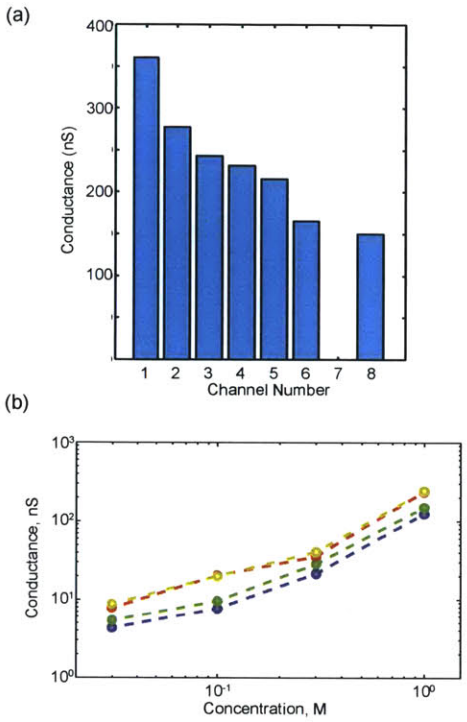

Figure 5.4.1: Multiplexed measurements of silicon nitride nanopores in a microfluidic device. (a) Measurements of silicon nitride nanopores each patterned with a nanopore diameter across the membrane. (b) Measurements of four different nanopores in a single device across four different salt concentrations.

be directly inferred from these measurements however, as they were performed at 100mM KCl, and these nanopores were not characterized in 1M KCl. While further measurements of graphene in these devices is needed to get a better understanding of the system, this experiment demonstrates that graphene can be reliably integrated into the device without any exposure to oxygen plasma. The only difference in treatment compared to the devices in Chapter 3 is that these graphene membranes were heated at 75 degrees Celsius during the PDMS curing steps.

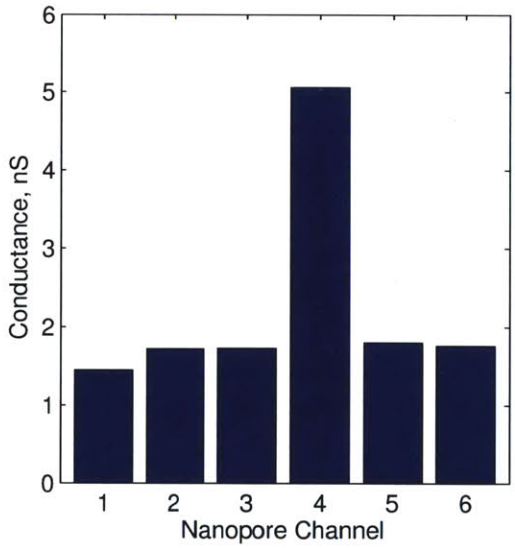

Figure 5.4.2: Multiplexed measurements of graphene suspended over silicon nitride nanopores.

Chapter 6

Outlook

6.1 Conclusions

In this thesis, the phenomenology and theory of ion transport through single graphene nanopores was studied. Inspired by the patch-clamp technique, a methodology for statistical isolation of graphene nanopores with single pore resolution was developed. From STEM imaging, a large fraction of the graphene nanopores in the sample were known to have sub-2 nm diameters. By comparing the conductance of the graphene nanopores measured in our experimental setup with experiments on larger nanopores and simulations on sub-2 nm nanopores, we confirmed that the majority of nanopores under test were less than 2 nm in diameter. In addition to having lower conductances compared to previous experimental results, the graphene nanopores measured also exhibited interesting nonlinear behaviors, including rectification, voltage-activation, and stochastic switching. Distinct trends in cation selectivity suggested that finite size effects are enabling rudimentary ionic discrimination.

The experimental observations clearly demonstrate that graphene nanopores can exhibit remarkable transport behaviors despite their atomic thickness. From a theoretical standpoint, a existing theory in stochastic differential equations has been applied to the description of solid-state nanopores - in particular to graphene nanopores - in a way that makes the open nature of the nanopore and the particle interactions explicitly accounted for. The solutions for the single particle case were used to develop a model for ion transport through graphene nanopores. The model suggests that ionic dehydration and electrostatic interactions with the nanopore are sufficient to produce a large range of nonlinear current-voltage behaviors. Extending the model to smaller pore sizes predicts that significant cation selectivity can be achieved in graphene nanopores. Furthermore, a method of directly estimating the validity of transport models was explored by combining nanopores structure estimation with self-consistency over large databases. To accelerate development of ex-

perimental and theoretical work in the area, a new device architecture for automated and high-throughput measurement of graphene nanopores was also developed.

6.2 Impact on the field

The field of two-dimensional industrial separations membranes is still in its infancy. However, two-dimensional membranes are likely to be *the* future of industrial separations, as they represent the highest possible performance that can be achieved from a separations process. Simulations, and measurements over large area membranes, have shown sufficiently promising results that it is very likely that this research will continue to make strides in the future. If research on polymer based membranes is any indication, however, one of the dangers in the future development of the field is a lack of mechanistic understanding for the origins of selectivity through nanopores in two-dimensional materials.

This thesis has explored, through many different perspectives, the fundamental question of the transport properties of individual graphene nanopores. These perspectives have included experimental measurement of graphene nanopores, providing a theoretical basis for ion transport through graphene nanopores, developing analytic models for current through a nanopore and structure-function relationship, methods for testing the validity of a transport theory, and device architectures for experimentally accelerating scientific analysis.

Accurate models for transport on the sub-nanometer lengthscale will naturally enable accurate estimation of the selectivity of a nanopore. Therefore, the work presented in this thesis has provided foundational work for analysis of the selectivity of two-dimensional nanopores. The theory presented in this thesis does predict that as the nanopore size decreases, it should become possible to engineer selectivity, and we anticipate that this work will motivate further attempts to create selective graphene nanopores for applications. This study provides also method for understanding the relationship between structure and function in a more precise way. Knowledge of this relationship is expected to advance both fundamental understanding of ionic transport, as well as improve our ability to engineer functional transport behaviors into synthetic materials.

There are nonetheless many unanswered questions, with many opportunities for researchers entering into a nascent field. This thesis should prove to be a useful tool for any future work on aqueous phase separations with two-dimensional nanopore based membranes.

Bibliography

[1] Celebi, K, Buchheim, J, Wyss, R. M, Droudian, A, Gasser, P, Shorubalko, I, Kye, J. I, Lee, C, & Park, H. G. (2014) Ultimate Permeation Across Atomically Thin Porous Graphene. *Science* **344**, 289–292.

[2] Cohen-Tanugi, D & Grossman, J. C. (2012) Water Desalination across Nanoporous Graphene. *Nano Letters* **12**, 3602–3608.

[3] Mistry, K & Lienhard, J. (2013) Generalized Least Energy of Separation for Desalination and Other Chemical Separation Processes. *Entropy* **15**, 2046–2080.

[4] Geise, G. M, Park, H. B, Sagle, A. C, Freeman, B. D, & McGrath, J. E. (2011) Journal of Membrane Science. *Journal of Membrane Science* **369**, 130–138.

[5] Humplik, T, Lee, J, O'Hern, S. C, Fellman, B. A, Baig, M. A, Hassan, S. F, Atieh, M. A, Rahman, F, Laoui, T, Karnik, R, & Wang, E. N. (2011) Nanostructured materials for water desalination. *Nanotechnology* **22**, 292001.

[6] Cohen-Tanugi, D, McGovern, R. K, Dave, S. H, Lienhard, J. H, & Grossman, J. C. (2014) Quantifying the potential of ultra-permeable membranes for water desalination. *Energy & Environmental Science* **7**, 1134.

[7] Schrödinger, E. (1944) *What is life? The physical aspect of the living cell.* (Cambridge University Press).

[8] Arendt, H. (1958) *The human condition.* (University of Chicago Press).

[9] Kumar, M, Grzelakowski, M, Zilles, J, Clark, M, & Meier, W. (2007) Highly permeable polymeric membranes based on the incorporation of the functional water channel protein Aquaporin Z. *Proceedings of the National Academy of Sciences of the United States of America* **104**, 20719–20724.

[10] Lee, C, Wei, X, Kysar, J. W, & Hone, J. (2008) Measurement of the Elastic Properties and Intrinsic Strength of Monolayer Graphene. *Science* **321**, 385–388.

[11] Lee, G. H, Cooper, R. C, An, S. J, Lee, S, van der Zande, A, Petrone, N, Hammerberg, A. G, Lee, C, Crawford, B, Oliver, W, Kysar, J. W, & Hone, J. (2013) High-Strength Chemical-Vapor-Deposited Graphene and Grain Boundaries. *Science* **340**, 1073–1076.

[12] Kobayashi, T, Bando, M, Kimura, N, Shimizu, K, Kadono, K, Umezu, N, Miyahara, K, Hayazaki, S, Nagai, S, Mizuguchi, Y, Murakami, Y, & Hobara, D. (2013) Production of a 100-m-long high-quality graphene transparent conductive film by roll-to-roll chemical vapor deposition and transfer process. *Applied Physics Letters* **102**, 023112.

[13] Bunch, J. S, Verbridge, S. S, Alden, J. S, van der Zande, A. M, Parpia, J. M, Craighead, H. G, & McEuen, P. L. (2008) Impermeable Atomic Membranes from Graphene Sheets. *Nano Letters* **8**, 2458–2462.

[14] Hu, S, Lozada-Hidalgo, M, Wang, F. C, Mishchenko, A, Schedin, F, Nair, R. R, Hill, E. W, Boukhvalov, D. W, Katsnelson, M. I, Dryfe, R. A. W, Grigorieva, I. V, Wu, H. A, & Geim, A. K. (2014) Proton transport through one-atom-thick crystals. *Nature* **516**, 227–230.

[15] Suk, M. E & Aluru, N. R. (2013) Molecular and continuum hydrodynamics in graphene nanopores. *RSC Advances* **3**, 9365.

[16] Suk, M. E & Aluru, N. R. (2014) Ion transport in sub-5-nm graphene nanopores. *The Journal of Chemical Physics* **140**, 084707.

[17] Ohtaki, H & Radnai, T. (1993) Structure and dynamics of hydrated ions. *Chemical Reviews* **93**, 1157–1204.

[18] Sint, K, Wang, B, & Král, P. (2008) Selective Ion Passage through Functionalized Graphene Nanopores. *Journal of the American Chemical Society* **130**, 16448–16449.

[19] Zhao, S, Xue, J, & Kang, W. (2013) Ion selection of charge-modified large nanopores in a graphene sheet. *The Journal of Chemical Physics* **139**, 114702.

[20] Yamada, Y, Murota, K, Fujita, R, Kim, J, Watanabe, A, Nakamura, M, Sato, S, Hata, K, Ercius, P, Ciston, J, Song, C. Y, Kim, K, Regan, W, Gannett, W, & Zettl, A. (2014) Subnanometer Vacancy Defects Introduced on Graphene by Oxygen Gas. *Journal of the American Chemical Society* **136**, 2232–2235.

[21] Russo, C. J & Golovchenko, J. A. (2012) Atom-by-atom nucleation and growth of graphene nanopores. *Proceedings of the National Academy of Sciences of the United States of America* **109**, 5953–5957.

[22] O'Hern, S. C, Boutilier, M. S. H, Idrobo, J.-C, Song, Y, Kong, J, Laoui, T, Atieh, M, & Karnik, R. (2014) Selective Ionic Transport through Tunable Subnanometer Pores in Single-Layer Graphene Membranes. *Nano Letters* **14**, 1234–1241.

[23] Lv, R, Li, Q, Botello-Méndez, A. R, Hayashi, T, Wang, B, Berkdemir, A, Hao, Q, Elías, A. L, Cruz-Silva, R, Gutiérrez, H. R, Kim, Y. A, Muramatsu, H, Zhu, J, Endo, M, Terrones, H, Charlier, J.-C, Pan, M, & Terrones, M. (2012) Nitrogen-doped graphene: beyond single substitution and enhanced molecular sensing. *Scientific Reports* **2**.

[24] Boutilier, M. S. H, Sun, C, O'Hern, S. C, Au, H, Hadjiconstantinou, N. G, & Karnik, R. (2014) Implications of Permeation through Intrinsic Defects in Graphene on the Design of Defect-Tolerant Membranes for Gas Separation. *ACS Nano* **8**, 841–849.

[25] Dirac, P. A. M. (1929) Quantum mechanics of many-electron systems. *Proceedings of the Royal Society of London. Series A, Containing Papers of a Mathematical and Physical Character* pp. 714–733.

[26] Percus, J. K. (2014) Molecular transport under tight confinement. *AIP Conference Proceedings* **1579**.

[27] Born, M & Green, H. S. (1946) A General Kinetic Theory of Liquids. I. The Molecular Distribution Functions. *Proc.Roy.Soc.* **A188**, 10–18.

[28] Kirkwood, J. G. (1947) The Statistical Mechanical Theory of Transport Processes II. Transport in Gases. *The Journal of Chemical Physics* **15**, 72.

[29] Kerins, J, Scriven, L, & Davis, H. (1986) Correlation functions in subcritical fluid. *Adv. Chem. Phys* **65**, 215–279.

[30] Percus, J. K. (1976) Equilibrium state of a classical fluid of hard rods in an external field. *Journal of Statistical Physics* **15**, 505–511.

[31] Doyle, D. A, Cabral, J. M, Pfuetzner, R. A, Kuo, A, Gulbis, J. M, Cohen, S. L, Chait, B. T, & MacKinnon, R. (1998) The structure of the potassium channel: molecular basis of K+ conduction and selectivity. *Science* **280**, 69–77.

[32] Walz, T, Hirai, T, Murata, K, Heymann, J. B, Mitsuoka, K, Fujiyoshi, Y, Smith, B. L, Agre, P, & Engel, A. (1997) The three-dimensional structure of aquaporin-1. *Nature* **387**, 624–627.

[33] Song, L, Hobaugh, M. R, Shustak, C, Cheley, S, Bayley, H, & Gouaux, J. E. (1996) Structure of staphylococcal α-hemolysin, a heptameric transmembrane pore. *Science* **274**, 1859–1865.

[34] Schoch, R, Han, J, & Renaud, P. (2008) Transport phenomena in nanofluidics. *Rev.Mod.Phys.* **80**, 839–883.

[35] Hodgkin, A. L & Katz, B. (1949) The effect of sodium ions on the electrical activity of giant axon of the squid. *The Journal of physiology* **108**, 37–77.

[36] Eisenman, G. (1962) CATION SELECTIVE GLASS ELECTRODES. *Biophysical Journal* **2**, 259–323.

[37] Neher, E & Sakmann, B. (1976) Single-Channel Currents Recorded From Membrane of Denervated Frog Muscle-Fibers. *Nature* **260**, 799–802.

[38] Shrivastava, I. H & Sansom, M. S. P. (2000) Simulations of Ion Permeation Through a Potassium Channel: Molecular Dynamics of KcsA in a Phospholipid Bilayer. *Biophysical Journal* **78**, 557–570.

[39] Chiu, S. W, Subramaniam, S, & Jakobsson, E. (1999) Simulation study of a gramicidin/lipid bilayer system in excess water and lipid. I. Structure of the molecular complex. *Biophysical Journal* **76**, 1929–1938.

[40] Schuss, Z, Nadler, B, & Eisenberg, R. (2001) Derivation of Poisson and Nernst-Planck equations in a bath and channel from a molecular model. *Physical Review E* **64**, 036116.

[41] Peskoff, A & Bers, D. M. (1988) Electrodiffusion of ions approaching the mouth of a conducting membrane channel. *Biophysical Journal* **53**, 863–875.

[42] Luchinsky, D, Tindjong, R, Kaufman, I, McClintock, P, & Eisenberg, R. (2009) Self-consistent analytic solution for the current and the access resistance in open ion channels. *Physical Review E* **80**, 021925.

[43] Barcilon, V. (1992) Ion flow through narrow membrane channels: Part I. *SIAM Journal on Applied Mathematics* **52**, 1391–1404.

[44] Davis, H. T. (1995) *Statistical Mechanics of Phases, Interfaces, and Thin Films.* (VCH Publishers, Inc.).

[45] Risken, H. (1984) *The Fokker-Planck Equation*, Springer Series in Synergetics. (Springer-Verlag).

[46] Attard, P. (2012) *Non-Equilibrium Thermodynamics and Statistical Mechanics.* (Oxford University Press).

[47] Kardar, T. (2007) *Statistical Physics of Particles.* (Cambridge University Press).

[48] Garcia-Palacios, J. L. (2007) Introduction to the theory of stochastic processes and Brownian motion problems. *arXiv.org.*

[49] Cichocki, B. (1987) The generalized Smoluchowski equation for interacting Brownian particles with hard cores. *Zeitschrift für Physik B Condensed Matter* **66**, 537–540.

[50] Jain, T, Aernecke, M, Liberman, V, & Karnik, R. (2014) High resolution fabrication of nanostructures using controlled proximity nanostencil lithography. *Applied Physics Letters* **104**, 083117.

[51] Garaj, S, Hubbard, W, Reina, A, Kong, J, Branton, D, & Golovchenko, J. A. (2010) Graphene as a subnanometre trans-electrode membrane. *Nature* **467**, 190–193.

[52] Merchant, C. A, Healy, K, Wanunu, M, Ray, V, Peterman, N, Bartel, J, Fischbein, M. D, Venta, K, Luo, Z, Johnson, A. T. C, & Drndić, M. (2010) DNA Translocation through Graphene Nanopores. *Nano Letters* **10**, 2915–2921.

[53] Schneider, G. F, Kowalczyk, S. W, Calado, V. E, Pandraud, G, Zandbergen, H. W, Vandersypen, L. M. K, & Dekker, C. (2010) DNA Translocation through Graphene Nanopores. *Nano Letters* **10**, 3163–3167.

[54] Lindsey, S & Hobler, G. (2012) The significance of redeposition and backscattering in nanostructure formation by focused ion beams. *Nuclear Instruments and Methods in Physics Research Section B: Beam Interactions with Materials and Atoms* **282**, 12–16.

[55] Tseng, A. A. (2004) Recent developments in micromilling using focused ion beam technology. *Journal of Micromechanics and Microengineering* **14**, R15.

[56] Lehtinen, O, Kotakoski, J, Krasheninnikov, A. V, Tolvanen, A, Nordlund, K, & Keinonen, J. (2010) Effects of ion bombardment on a two-dimensional target: Atomistic simulations of graphene irradiation. *Physical Review B* **81**, 153401.

[57] Jain, T, Guerrero, R. J. S, Aguilar, C. A, & Karnik, R. (2013) Integration of Solid-State Nanopores in Microfluidic Networks via Transfer Printing of Suspended Membranes. *Analytical Chemistry* **85**, 3871–3878.

[58] Bezrukov, S. M & Kasianowicz, J. J. (1993) Current Noise Reveals Protonation Kinetics and Number of Ionizable Sites in an Open Protein Ion Channel. *Physical Review Letters* **70**, 2352–2355.

[59] Kasianowicz, J. J & Bezrukov, S. M. (1995) Protonation dynamics of the alpha-toxin ion channel from spectral analysis of pH-dependent current fluctuations. *Biophysical Journal* **69**, 94–105.

[60] Laio, A & Torre, V. (1999) Physical Origin of Selectivity in Ionic Channels of Biological Membranes. *Biophysical Journal* **76**, 129–148.

[61] Mähler, J & Persson, I. (2012) A Study of the Hydration of the Alkali Metal Ions in Aqueous Solution. *Inorganic Chemistry* **51**, 425–438.

[62] Tongraar, A, Liedl, K. R, & Rode, B. M. (1998) Born Oppenheimer ab Initio QM/MM Dynamics Simulations of Na +and K +in Water: From Structure Making to Structure Breaking Effects. *The Journal of Physical Chemistry A* **102**, 10340–10347.

[63] Burger, M, Eisenberg, R. S, & Engl, H. W. (2007) Inverse Problems Related to Ion Channel Selectivity. *SIAM Journal on Applied Mathematics* **67**, 960–989.

[64] Baaken, G, Sondermann, M, Schlemmer, C, Rühe, J, & Behrends, J. C. (2008) Planar microelectrode-cavity array for high-resolution and parallel electrical recording of membrane ionic currents. *Lab on a Chip* **8**, 938.

[65] Osaki, T, Suzuki, H, Le Pioufle, B, & Takeuchi, S. (2009) Multichannel Simultaneous Measurements of Single-Molecule Translocation in α-Hemolysin Nanopore Array. *Analytical Chemistry* **81**, 9866–9870.

[66] Kleefen, A, Pedone, D, Grunwald, C, Wei, R, Firnkes, M, Abstreiter, G, Rant, U, & Tampé, R. (2010) Multiplexed Parallel Single Transport Recordings on Nanopore Arrays. *Nano Letters* **10**, 5080–5087.

[67] Rosenstein, J. K, Wanunu, M, Merchant, C. A, Drndić, M, & Shepard, K. L. (2012) Integrated nanopore sensing platform with sub-microsecond temporal resolution. *Nature Methods* **9**, 487–492.

[68] Uddin, A, Yemenicioglu, S, Chen, C.-H, Corigliano, E, Milaninia, K, & Theogarajan, L. (2013) Integration of solid-state nanopores in a 0.5 μm CMOS foundry process. *Nanotechnology* **24**, 155501.

[69] Kim, J, Maitra, R, Pedrotti, K. D, & Dunbar, W. B. (2013) A patch-clamp ASIC for nanopore-based DNA analysis. *Biomedical Circuits and Systems, IEEE Transactions on* **7**, 285–295.

[70] Maitra, R. D, Kim, J, & Dunbar, W. B. (2012) Recent advances in nanopore sequencing. *ELECTROPHORESIS* **33**, 3418–3428.

[71] Unger, M. A, Chou, H.-P, Thorsen, T, Scherer, A, & Quake, S. R. (2000) Monolithic microfabricated valves and pumps by multilayer soft lithography. *Science* **288**, 113–116.

[72] Chen, H, Gu, W, Cellar, N, Kennedy, R, Takayama, S, & Meiners, J.-C. (2008) Electromechanical Properties of Pressure-Actuated Poly(dimethylsiloxane) Microfluidic Push-Down Valves. *Analytical Chemistry* **80**, 6110–6113.